Exceptional Phytoplankton Bloom Recognition from Visible Spectral Satellite Radiometry Data

DISSERTATION

zur Erlangung des akademischen Grades eines
Doktors der Naturwissenschaften
am Fachbereich für Geowissenschaften
der Freien Universität Berlin

vorgelegt von

KERSTIN EBERT

Berlin, 29.09.2009

1. Gutachter: Univ.–Prof. Dr. Jürgen Fischer

2. Gutachter: Univ.–Prof. Dr. Maik Thomas

Tag der Disputation: 29.09.2009

Selbstständigkeitserklärung

Hiermit erkläre ich, Kerstin Ebert, die vorliegende Arbeit ohne fremde Hilfe verfasst und nur die angegebene Literatur und die angegebenen Hilfsmittel verwendet zu haben.

Abstract

The subject of this work is the parameterization, the development, and the application of a method for the detection of exceptional algal blooms in the oceans from data of a multi-spectral satellite radiometer. The feasibilty and the restrictions for the detection of two specific blooms from satellite radiometry data are studied. Key of the approach is the utilization of macroscopic optical properties of in-water constituents within the semi-analytic retrieval algorithms.

The thesis describes the development of a processing system for deriving bloom extent and intensity from Envisat MERIS data. The processing system consists of a radiative transfer forward model, MOMO, and an Artificial Neural Network applied for the inversion. The algorithms are developed to be applied to MERIS Level-1b data, i.e., top-of-atmosphere radiances, without a prior atmospheric correction. The algorithms indicate the extention of the blooms by masks, which are based on threshold values of remote sensing reflectances retrieved by the processing system. The intensity of the blooming region is given by the particular phytoplankton concentration derived. While the overall structure of the processing system is general, distinct optical properties of different types of algal blooms make it necessary to apply tailored inversion algorithms, but also offer the possibility to utilize these characteristics in remote sensing and to distinguish the respective blooms from other oceanic or atmospheric events.

Here, specific algorithms for two distinct types of algal blooms are developed: (1) cyanobacterial blooms occuring in the Baltic Sea in summer, and (2) globally abundant coccolithophore blooms in the open oceans. Both types of blooms occur frequently and they are large enough to be recognized in medium resolution satellite data. Each of them is characterized by a unique set of optical properties, which is dicussed in detail in this work. Cyanobacterial blooms are characterized by their specific spectral absorption behaviour, while coccolithophore blooms exhibit distinct scattering characteristics. The basic algorithms consider these specific optical properties. For the Baltic Sea the typical in-water constituent concentration are taken into account and for coccolithophore blooms the marine calcite concentration is derived.

For each of the bloom types the specific algorithms for bloom extent and intensity derivation are described. Focus is on the sensitivity of the bio-optical models, i.e., the bulk optical properties of the in-water constituents as well as the phytoplankton concentration ranges and their dependencies to other parameters. Performance and sensitivity of the algorithms are analyzed and restrictions are discussed. The application of the algorithms to MERIS Level-1b data is demonstrated for both bloom types. Results are compared against MODIS-Aqua satellite data products for coccolithophore blooms and against available *in-situ* measurements for the Baltic Sea.

Zusammenfassung

Die vorliegende Arbeit beschäftigt sich mit der Anwendung und Entwicklung einer Methode zur Erkennung aussergewöhnlicher Algenblüten in Ozeanen aus multispektralen Daten satellitengetragener Sensoren. Es wird untersucht, inwieweit eine Erkennung von Phytoplanktonblüten aus radiometrischen Satellitendaten möglich ist und welchen Beschränkungen die Qualität der Ergebnisse unterliegt. Der hier gewählte Ansatz basiert auf der expliziten Nutzung makroskopischer optischer Eigenschaften der Wasserinhaltsstoffe.

Die Verfahren benutzen MERIS Level-1b Daten, d.h. Messungen der Strahldichten am Oberrand der Atmosphäre, ohne vorhergehende Korrektur des Einflusses der Atmosphäre. Die entwickelten Algorithmen liefern als Resultat die räumliche Ausdehnung der Phytoplanktonblüten in Form einer Maske, die auf Schwellwerten der abgeleiteten Reflektanzen an der Wasseroberfläche basiert. Die Intensität der Algenblüten wird anhand der jeweiligen abgeleiteten Phytoplanktonkonzentrationen angegeben. Die entwickelten Algorithmen basieren auf Rechnungen mit dem Strahlungstransfermodell MOMO zur Vorwärtssimulation von Strahldichten in Abhängigkeit von Wasserkörper- und Atmosphäreneigenschaften und einem künstlichen neuronalen Netz zur Inversion.

Während die zu Grunde liegende Struktur des Prozessierungssystems allgemein gülig ist, erfordern die deutlich verschiedenen optischen Eigenschaften der Algenarten die Anwendung spezifischer Parameterisierungen der Wasserinhaltsstoffe. Im Rahmen der vorliegenden Arbeit wurden spezifische Algorithmen für zwei Algenblütenarten entwickelt: (1) Phytoplanktonblüten von Cyanobakterien im Ostseeraum und (2) global auftretende Coccolithophoren im offenen Ozean. Beide Arten von Algenblüten treten regelmässig auf und haben eine ausreichende Ausdehnung, um sie in Satellitendaten mit mittlerer räumlicher Auflösung erkennen zu können. Jede dieser Arten zeichnet sich ausserdem durch einen Satz eindeutiger optischer Eigenschaften aus, die es ermöglichen sie aus Strahlungsmessungen zu detektieren. Cyanobakterienblüten sind durch ihr spezifisches spektrales Absorptionsverhalten charakterisiert, während Coccolithophorenblüten ausgeprägte Streucharakteristika aufweisen.

In der Arbeit werden für beide Arten von Phytoplanktonblüten die spezifischen Algorithmen zur Ableitung von Ausdehnung und Intensität der Blüte beschrieben. Für die Ostsee werden die typischen Wassereigenschaften berücksichtigt und fr Coccolihophorenblüten wird die partikuläre Calciumcarbonat Konzentration abgeleitet. Der Schwerpunkt liegt auf Ausführungen zu den angewendeten bio-optischen Modellen, d.h. den optischen Eigenschaften der Gesamtheit der Wasserinhaltsstoffe, sowie die berücksichtigten Spannen der Konzentrationen und ihren Abhängigkeiten. Leistungsfähigkeit und Empfindlichkeit der Algorithmen werden analysiert und ihre Grenzen diskutiert. Die Anwendung der Algorithmen auf MERIS Daten wird für beide Algenblütenarten demonstriert. Die Ergebnisse werden für Coccolithophorenblüten mit MODIS-Aqua Satellitenprodukte verglichen und für die Ostsee mit verfügbare *in-situ* Messungen validiert.

Contents

List of Figures **iii**

List of Tables **v**

1 Introduction **1**
- 1.1 Visible Spectral Radiometry of the Oceans from Space 1
- 1.2 Exceptional Phytoplankton Bloom Recognition 2
- 1.3 State of Research 4
- 1.4 Objectives of this Research and Outline 5

2 Radiometry and Bio – Optics **7**
- 2.1 Radiometry and Optical Properties of Water Bodies 7
  - 2.1.1 Basic Radiometric Quantities 7
  - 2.1.2 Apparent and Inherent Optical Properties 8
  - 2.1.3 Specific IOPs and Mie Theory 10
  - 2.1.4 Bulk IOPs 11
  - 2.1.5 The Equation of Radiative Transfer (RTE) 13
- 2.2 Biology of Marine Water Bodies 15
  - 2.2.1 Compounds of Natural Waters 15
  - 2.2.2 Phytoplankton 17

3 The Processing System **19**
- 3.1 The Forward Model 20
  - 3.1.1 The Radiative Transfer Model MOMO: Radiative Transfer Simulations . 20
  - 3.1.2 Bio-optical Model for Inherent Optical Properties 21
  - 3.1.3 Description of the Atmospheric Model and the Geometry Setup 24
  - 3.1.4 Further Effects and Model Restrictions 25
- 3.2 Inversion Algorithm 28
  - 3.2.1 Artificial Neural Network Architecture 29
  - 3.2.2 Artificial Neural Network Training 29
  - 3.2.3 Discussion of the Inverse Problem 33
- 3.3 The Retrieval Process 34
- 3.4 Characteristics of Envisat MERIS Data 35

4 Algorithm for the Baltic Sea 37
4.1 Background . . . 37
4.1.1 The Baltic Sea Basin . . . 37
4.1.2 Optical Characterization . . . 38
4.1.3 Phytoplankton Blooms of *Cyanophycaea* . . . 39
4.1.4 Algorithms for *Cyanophycaea* . . . 40
4.2 Bio-optical Model for the Baltic Sea . . . 41
4.2.1 Parameterization of Absorption . . . 41
4.2.2 Parameterization of Scattering . . . 50
4.2.3 Concentration Ranges and Dependencies . . . 51
4.2.4 Sensitivity . . . 53
4.2.5 Effects of Vertical Stratification . . . 55
4.2.6 Discussion of the Bio-optical Model for the Baltic Sea . . . 60
4.3 Algorithm Performance and Sensitivity . . . 60
4.4 Cyanobacterial Bloom and Surface Accumulation Mask . . . 61
4.5 Comparison of Derived Bio-geophysical Producs . . . 63
4.6 Discussion and Conclusion . . . 65

5 Particulate Inorganic Calcite Retrieval 66
5.1 Background . . . 66
5.1.1 The Oceanic Carbon Cycle . . . 67
5.1.2 Occurences of *Emiliania huxleyi* Coccolithophore Blooms . . . 68
5.1.3 Algorithms for Coccolithophore Bloom Detection . . . 69
5.2 Bulk IOPs for Coccolithophore Blooms . . . 70
5.2.1 Parameterization and Sensitivity . . . 70
5.2.2 Concentration Ranges and Dependencies . . . 73
5.2.3 Discussion of the Bio-optical Model for PIC . . . 75
5.3 Algorithm Performance . . . 75
5.4 Demonstration of the Algorithm and Comparison . . . 77
5.4.1 Derived Remote Sensing Reflectance R_{RS} . . . 78
5.4.2 Coccolithophore Mask . . . 80
5.4.3 Calcite Concentration (PIC) . . . 84
5.5 Discussion and Conclusion . . . 85

6 Summary and Outlook 87

List of Acronyms, Symbols, and Indices 90

Bibliography 96

Acknowledgements 105

List of Figures

2.1 Example of an underwater light field. 9
2.2 Radiant quantities commonly used in water optics. 14
2.3 Schematic overview of in-water constituents. 14

3.1 Schematic overview of the processing system. 20
3.2 Volume scattering function, absorption and scattering of pure and seawater. . . . 23
3.3 Schematic overview on the Aerosol Models. 26
3.4 Examples of the distribution of aerosol model variables. 27
3.5 Measured AOT by the Aeronet system. 27
3.6 Example of the architecture of the Artificial Neural Network (ANN). 30
3.7 Relative error and histogram distribution of the full and the subset synthetic dataset. 33
3.8 MERIS, MODIS and SeaWiFS spectral bands. 36

4.1 Chlorophyll-a concentrations in the Baltic Sea. 40
4.2 Comparison of specific chlorophyll-a absorption coefficients. 42
4.3 Specific absorption coefficients a^*_{Chla} for cyanobacteria. 43
4.4 Regression for a_{Ph} in $Chla$. 44
4.5 Comparison of phytoplankton absorption power model parameters. 44
4.6 Comparison of bulk phytoplankton absorption 45
4.7 Impact of the parameterization of a_{Ph}. 46
4.8 Comparison of spectral a_{YS} absorption coefficients. 47
4.9 Impact of S_{YS} on radiances. 48
4.10 Scattering of TSM in the Baltic Sea. 50
4.11 Phase function for cyanobacteria as given by Volten et al. (1998). 51
4.12 Histogram distribution of in-water constituent concentrations in the Baltic Sea. . 52
4.13 Dependencies of in-water concentrations in the Baltic Sea. 52
4.14 Concentration ranges of in-water concentrations for the Baltic Sea. 53
4.15 Sensitivity of reflectance for varying YS and [$Chla$]. 54
4.16 Sensitivity of reflectance for varying TSM and [$Chla$]. 55
4.17 R_RS for varying phytoplankton concentrations. 56
4.18 Example of spectral measurements by MERIS over the Baltic Sea. 57
4.19 Example of a stratified water body. 58

4.20 Example of a stratified phytoplankton bloom. 58
4.21 Look-up table diagram for L_{TOA} ratios. 59
4.22 Comparison of retrieved and simulated products vs. test data for FUB-Baltic. . . 61
4.23 Example of the cyanobacteria bloom mask for the Baltic Sea. 62
4.24 Example of MERIS measurements. 63
4.25 Comparison of retrieved products to *in-situ* data. 64

5.1 Scattering properties of PIC. 71
5.2 Phase function for *E. huxleyi* with coccoliths. 72
5.3 Correlation of Ph and YS. 74
5.4 Histogram of in-water concentration distribution. 74
5.5 R_{RS} and L_{TOA} at 412.5nm for varying PIC and $[Chla]$. 75
5.6 Comparison of retrieved and simulated R_{RS} of the test data. 76
5.7 Comparison of retrieved and simulated PIC of the test data. 77
5.8 Look-up table diagram for $R_{RS}(412.5\,\text{nm})$ against $R_{RS}(560\,\text{nm})$. 77
5.9 Example of L_{TOA} and R_W MERIS measurements. 79
5.10 Comparison of FUB-PIC and ESA-Level-2 reflectance. 80
5.11 Comparison of coccolithophore masks. 82
5.12 Cloud mask and coccolithophore bloom interactions. 83
5.13 PIC comparison FUB-PIC vs. MYD23. 84
5.14 Comparison of PIC concentrations. 85
5.15 Scatter diagram for MERIS FUB-PIC vs. MODIS MYD23. 85

List of Tables

2.1 Units and symbols of apparent optical properties 10

3.1 Parameterization of the atmosphere model. 25
3.2 Noise added to training data. 32

4.1 Relative contributions in the Baltic Sea. 38
4.2 Algorithms for cyanophycaea bloom recognition in the Baltic Sea 41
4.3 Setup corresponding to Fig. 4.7. 46
4.4 YS and NAP model for the Baltic Sea. 47
4.5 Parameters for sensitivity study shown in Fig. 4.9. 48
4.6 Parameterization of IOPs for the Baltic Sea 49
4.7 In-water concentration ranges in the Baltic Sea. 52
4.8 Setup for sensitivity study for changing [$Chla$ 53
4.9 Setup for sensitivity study for changing [$Chla$] and TSM. 54
4.10 FUB-BALTIC cyanobacterial mask setting. 62
4.11 Comparison of derived geo-physical products. 65

5.1 Algorithms for coccolithophore bloom recognition. 70
5.2 Parameterization for *coccolithophore* blooms. 73
5.3 Setup for the sensitivity shown for varying PIC and [$Chla$]. 74
5.4 FUB-PIC coccolithophore mask setting. 81

Chapter 1

Introduction

1.1 Visible Spectral Radiometry of the Oceans from Space

Ocean remote sensing from space has become a widely used and unique source of continuous, global, and recurrent measurements of ecological indicators describing oceanic, coastal, and inland waters. During the last 20 years, optical observations of the oceans have been collected by experimental visible, spectral satellite radiometers, as the Coastal Zone Color Scanner (CZCS), the Sea-viewing Wide Field-of-view Sensor (SeaWiFS), the Moderate Resolution Imaging Spectroradiometer (MODIS), the MEdium Resolution Imaging Spectrometer (MERIS), and others [Gordon and Morel (1983), Doerffer and Fischer (1994), O'Reilley et al. (1998), Rast et al. (1999)]. In 2013, the European Space Agency will start an operational polar orbiting satellite, Sentinel-3, with the Ocean and Land Colour Imager (OLCI) instrument onboard, a sensor similar to MERIS.

Geometric, spectral, and radiometric resolution of the satellite data have been improved. MERIS, e.g., as the most advanced of these sensors, offers 15 multi spectral bands and a medium spatial resolution of $1.1\,\mathrm{km}^2$ for global ocean applications. With time, advanced algorithms have been developed to derive more detailed geophysical and bio-geophysical information. The early missions' goal to monitor chlorophyll-a concentration in open oceans as a measure of global phytoplankton biomass has been extended to, e.g., the monitoring of the water composition, the detection of oil spills, or the improved retrieval of optical properties in coastal zones [Babin et al. (2008), Nair et al. (2008), Vargas et al. (2009)].

Remote sensing is an indirect measurement from distance. Visible optical radiometers collect the reflected electromagnetic radiation of remote objects. All geophysical parameters of these remote objects have to be retrieved from the measured radiant intensities by applying appropriate algorithms. Geophysical products routinely derived from visible satellite radiometry data are the water-leaving radiance at sensor wavelengths, the optically significant in-water constituents phytoplankton pigment concentration, colored dissolved organic matter absorption, non-pigmented particulate matter concentration, and optical water properties such as absorption and scattering coefficients (Sathyendranath, 2000a).

All these bio-geophysical products are indicators of the physical, biological, and chemical state of the oceans. Authorities and initiatives like the European Union Water Framework Directive (WFD), the Global Ocean Observing System (GOOS) of UNESCO, or the European network Global Monitoring for Environment and Security (GMES) require a dense and frequent monitoring of the ocean's composition to assess the marine role in Earth system dynamics. Of particular importance are climate research related applications as to record indicators of the ocean's response to climate change, and to calibrate, evaluate, and validate bio-geochemical ocean models [Gregg (2002), Le Quéré et al. (2005)].

Lately, space and time binned products are provided for climatology purposes (Antoine, 2004). Combining data from different satellite sensors allows an improved derivation of geophysical products as well as a better spatial coverage and temporal resolution (Gregg, 2007). The assimilation of satellite data into geo-biochemical models permits the assessment of complex processes as, e.g., understanding the oceanic carbon cycle and the marine food web dynamics.

1.2 Exceptional Phytoplankton Bloom Recognition

Marine phytoplankton blooms are rapid and temporary increases of algae, typically of one or a small number of phytoplankton species (Smayda, 1997a). Mass occurrences of phytoplankton are common and natural events, which appear under favorable conditions as when sufficient sunlight and nutrients become available. Periodic spring blooms occur in most waters when increased sunlight leads to the formation of the thermocline and abundant nutrients are available in the upper ocean due to well mixed waters after winter season. In autumn, winds stir nutrient rich waters to the surface which often forms fall blooms (Smayda, 1997b).

Two exceptional phytoplankton bloom events are regarded to in this study: (1) the cyanobacterial bloom occuring in the Baltic Sea during the summer months, and (2) the global appearances of regional scale coccolithophore blooms. These blooming events have been selected because of their extent, large enough to be recognized from medium spatial satellite data, their particular influence on water optics, and their exceptional state in the ecosystem.

Phytoplankton is generally important to monitor, since it is the primary producer in the marine food web. Phytoplankton blooms, as exceptional occurences in the oceans, are a sensitive indicator for marine ecosystem change. To assess a bloom's duration, its extent, and its intensity can help to understand the particular Earth system and climate interactions (Hallegraeff, 2003). Especially for the densly populated Baltic Sea region, nowcasting and forecasting of the potententially toxic, and therefore harmful, cyanobacterial bloom is of great public interest as for fisheries and tourism. The WFD and the intergovernmental Helsinki Commission (HELCOM) for the protection of the marine Baltic Sea environment request information on the cyanobacterial blooms for environmental management purposes and to govern policy makers. Detailed information on the Baltic Sea cyanobacterial bloom is given in chapter 4. Coccolithophore blooms are interesting to observe, since they draw a strong link to air/sea carbon dioxide fluxes and ocean's acidification, which is referred to in chapter 5.

Phytoplankton bloom events have been increased in duration, intensity, and frequency on global scale during the second half of the 20th century [Anderson et al. (1989, 2000), Bianchi et al. (2000)]. Main reasons for the increase have been shown to be due to

- increased coastal eutrophication due to agriculture and aquaculture (Anderson et al., 2002),
- climate change related transformations (Taylor, 1990), (Smayda, 1997a) like
    - warming of surface sea water (Stumpf and Tomlinson, 2005),
    - declining pH-values of oceanic water (acidification) (Bianchi et al., 2000),
    - increasing storm events causing increased resuspension of spores (Babin et al., 2004),
    - ecosystem and marine diversity change (Andréfouët et al., 2008),
- transportation of alien phytoplankton species in ship ballast water (Hallegraeff, 2003).

The Global Ecology and Oceanography of Harmful Algal Blooms (GEOHAB) program of the Intergovernmental Oceanographic Commission (IOC) of UNESCO states the importance of new autonomous, continuous, and real-time ocean-observation technologies to permit the monitoring of marine phytoplankton blooms and in future to develop their prediction [Babin et al. (2005); Babin et al. (2008)]. Long-term goals are the determination of marine phytoplankton community structures, to assess dynamics and global phenology, to improve marine biomass estimations, to understand the oceanic carbon cycle and air/sea flux interactions. Although, oceanic plant biomass is less than 0.05% of lands biomass, the annual oceanic net primary productivity given in [PgC yr^{-1}] is with 48.5% almost the same as the terrestrial productivity (56.4%) (Falkowski et al., 1998). Climate change processes are expected to affect the magnitude of phytoplankton biomass and the timing of the annual cycle (Vargas et al., 2009). Thus, continuous and robust *in-situ* and remote sensing observations of marine biomass markers and bloom lifecycles are needed [Cullen et al. (1997), Babin et al. (2008)].

Remote sensing from space with visible, multi-spectral resolution radiometers strongly meets the demands of near real-time monitoring. It is the only autonomous observational technology allowing both: continuous and recurrent measurements as well as a wide spatial coverage appropriate to detect the extent of phytoplankton blooms. The revisit time is one day for MODIS satellite data and three days for MERIS. Strongest limitating factor is the Earth's cloud cover, which reduces the number of analyzable ocean measurements.

Phytoplankton species in the oceans are very diverse in space and time. Platt and Sathyendranath (2008) formulated the identification of phytoplankton species, which are also called phytoplankton functional types (PFTs) according to their role in the marine bio-geochemical cycle, as one major objective in ocean optics. Ocean water composition in general is varying between regions, especially in optically complex waters with more than one in-water compound, which demands the development of retrieval algorithms on regional scale to reach sufficient accuracy [Sathyendranath (2000b), Babin et al. (2003)].

Long-term objectives are to target the species, the concentration, and to trace all phases of the blooming cycle as well as to evaluate inter-annual changes and trends (Robinson, 2008). On this way, scientific questions have to be answered as, e.g., 'How to assess different phytoplankton populations from distance?' or 'How do varying optical properties affect the remote measured signal?'.

1.3 State of Research

Although a strong need to monitor phytoplankton blooms exists, they often remain unobserved by standard monitoring programs, both *in-situ* shipborne or buoy sampling and remote sensing. For a comprehensive overview on new *in-situ* observational technologies capable for phytoplankton bloom detection, the book by Babin et al. (2008) is recommended.

As discussed, visible, multi-spectral satellite radiometry offers global, recurrent measurements in combination with a medium spatial resolution, which allows the remote sensing of phytoplankton blooms. Standard remote sensing algorithms developed for open oceans and coastal waters are deriving radiant quantities at sea surface, optical properties of the surface waters, or bio-geophysical parameters as in-water constituent concentrations. To focus on the MERIS sensor, a standard global algorithm for open oceans (Antoine and Morel, 2000) and a standard algorithm for coastal waters (Schiller and Doerffer, 1999) have been developed. Also, further algorithms for coastal waters are available as by Schroeder et al. (2007a), which derives in-water constituent concentrations or the algorithm developed by Doerffer (2002), which can also derive water optical properties. Progress has been made, but still there are challenges as to derive in-water constituent concentrations in regional waters. Primary purpose of this study are two new applications of MERIS data, as (1) the development of a regional algorithm for the Baltic Sea, and (2) deriving the calcite concentration in global oceans. Both algorithms act as a basis from which the extent of the algalblooms is derived.

Further on, global datasets on phytoplankton functional types (PFT) are needed to recognize marine ecosystem composition and its influence on the oceanic bio-geochemical cycle. Remote sensing and the development of new algorithms is formulated to be one distinct source to access global PFT data (Le Quéré and Pesant, 2009). Bracher et al. (2008) recently published a new technique to retrieve PFTs. Using the Differential Optical Absorption Spectroscopy (DOAS) method, two phytoplankton groups were derived from very high spectral resolution SCIAMACHY (Scanning Imaging Absorption Spectrometer for Atmospheric Cartography) data. SCIAMACHY data has a 60 km spatial resolution, therefore it is not suitable for regional phytoplankton bloom detection. Using multi spectral satellite data, Uitz et al. (2008) studied the derivation of dominating phytoplankton size classes in open ocean waters, and Alvain et al. (2005) developed an empirical approach to retrieve dominant phytoplankton groups from SeaWiFS satellite data.

Concerning marine phytoplankton blooms, remote sensing standard algorithms usually do not consider the high in-water constituent concentrations of bloom events, atmospheric correction is difficult over these waters, and the specific optical features are not considered [Millie and Schofield (1995), Reinart and Kutser (2006), Ruddick et al. (2008)].

For visible ocean remote sensing particular methods have been developed to meet the need of regional algorithm development, which also allows the detection of marine phytoplankton blooms. Here, the basic principles of these algorithms are distinguished into four groups:

- algorithms that determine optical property variations between phytoplankton functional types (PFTs) e.g. (Nair et al., 2008),
    - bio-optical models differentiating absorption features e.g. (Sathyendranath et al., 2004) or
    - bio-optical models differentiating scattering properties e.g. (Gordon et al., 2001),
- band ratio algorithms (Simis et al., 2005a),
- algorithms that are based on radiance threshold values e.g. (Brown and Yoder, 1994), and
- anomaly maps of classified multi-spectral imagery e.g. (Stumpf et al., 2003).

For all these retrieval algorithms, parameterizations of the optical properties of the phytoplankton species have to be known. Also, prior knowledge of typical concentration ranges and vertical stratification in the water column is needed. For many dominating phytoplankton species and regional seas, species-specific optical properties have been published, like for coccolithophores (Brown and Yoder, 1994), diatoms (Sathyendranath et al., 2004), or nitrogen-fixing cyanobacteria *Trichodesmium* (Subramaniam et al., 2002).

Strongest limitations for the accuracy of the specific algorithms are related to the correction of the atmospheric influence (Babin et al., 2005). Most algorithms developed for phytoplankton bloom detection use atmospherically corrected water-leaving radiances as input. In general, atmospheric correction over non-open ocean waters is difficult due to varying aerosol loading in coastal regions and highly varying water composition, which leads to a biased derivation of bottom-of-atmosphere signals. Furthermore, the atmospheric correction does not imply the exceptional water signal occuring during blooming events.

1.4 Objectives of this Research and Outline

Objective of this study is to present a processing system to derive the extent and intensity of exceptional oceanic phytoplankton blooms from Envisat MERIS Level-1b data. The development of two new algorithms for the operational and continuous recognition of (1) blooms of *cyanophycaea* in the Baltic Sea and (2) coccolithophore blooms in the North Atlantic are presented.

The remote optical detection of cyanobacterial and coccolithophore blooms is possible since they occure with a unique set of optical properties. These blooms show specific compositions of bloom-forming compounds with distinguishable optical properties. Cyanobacterias are characterized by their exceptional absorption features, coccolithophores show a very specific backscatter behaviour. This work is focused on interpreting top-of-atmosphere signals rather than bottom-of-atmosphere information, to avoid errors introduced by unconsidered water signals.

Outline: An overview on fundamentals of optical remote sensing is given in ‘Radiometry and Bio-Optics‘ (chapter 2). The theory on radiant quantities, the radiative transfer equation, and bio-optical properties of in-water constituents is provided. Background information on the biology of water bodies are lined out. The following chapter ‘The Processing System‘ (chapter 3) utilizes the given fundamentals. The radiative transfer model MOMO is shortly decribed as well as the mathematical-physical setup of the coupled atmosphere-ocean system with its optical properties. The description of the applied regression technique Artificial Neural Networks for the inversion of the forward simulations is given. At the end of chapter 3 the MERIS satellite data are introduced.

The following two chapters describe the developed algorithms to derive phytoplankton bloom intensity and extent from Envisat MERIS top-of-atmosphere radiance measurements. Chapter 4 refers to cyanobacterial blooms and chapter 5 to blooms of coccolithophores. Each chapter begins with background information on the relevance of the algal bloom within the regional and global marine ecosystem. Based on available *in-stu* optical data, the applied bio-optical model parameterizations and the concentration ranges are given. The sensitivity of the algorithms is given and applications are demonstrated for validation examples. Chapter 6 finally summarizes the results presented and gives an outlook to future work on the detection of exceptional phytoplankton blooms.

Chapter 2

Theoretical Fundamentals of Radiometry and Bio – Optics

This chapter gives an introduction to fundamentals on remote sensing of water bodies. It provides a pool of all relevant background information utilized in the following chapters. Theoretical background on radiometry, physical quantities, and equation notations are provided. Information on biology of oceans, ecosystem dynamics in marine waters, and phytoplankton blooms are given at the end of this chapter.

2.1 Radiometry and Optical Properties of Water Bodies

Fig. 2.2, which can be find at the end of this section 2.1 on page 14, illustrates the relationships between radiant quantities and typical optical properties used in ocean optics in general, as well as in this study. All quantities and properties are introduced and defined in the following.

2.1.1 Basic Radiometric Quantities

The science of measuring radiant energy is named radiometry or radiation physics[1]. It characterizes a light field in terms of its power and energy. The fundamental radiometric property to describe the distribution of a radiation field is radiance $L(\theta, \phi, \lambda)$. Spectral radiance or intensity L is the energy emanating, as a narrow beam, from a source in a specified zenith angle θ and azimuth direction ϕ per unit solid angle and per unit area normal to the incident beam at a given wavelength λ. It is the radiant flux per unit area normal to the beam. Units of radiance are $[\mathrm{Wm^{-2}sr^{-1}nm^{-1}}]$.

All other radiometric quantities can be derived from radiance L. For radiance that incidents on a surface or sphere the term spectral irradiance $E(\lambda)$ is used. It is a measure of the flux of energy through a plane or a point weighted by the cosine of the incident angle θ. Spectral irradiance is

---

[1] Nomenclature and symbols are following Mobley (1994) who adobts recommendations of the Committee on Radiant Energy in the Sea of the International Association of Phyical Science of the Ocean (IAPSO). For reasons of clarity, only quantities used in this work are introduced. For further reading, excellent reviews can be found, e.g., in Mobley (1994), Kirk (1994), IOCCG (2000), and Zaneveld et al. (2005).

derived by integration of the radiance field over a defined solid angle, units are [$\mathrm{Wm}^{-2}\mathrm{nm}^{-1}$]. Irradiance that incidents a plane perpendicular to the beam direction is called plane irradiance $E(\lambda)$ and is given as the cosine-weighted integration over a hemisphere of the radiance field. Downwelling irradiance $E_d(\lambda)$ is the irradiance from the whole upper hemisphere, while upwelling irradiance $E_u(\lambda)$ is the irradiance from the whole lower hemisphere. The quantities are expressed in Eq. (2.1) and Eq. (2.2), respectively. Irradiance incident on a point is called scalar irradiance $E_o(\lambda)$ and results from the unweighted integration of radiance over the whole sphere, given in Eq. (2.3).

$$E_d(\lambda) = \int_0^{2\pi} d\phi \int_0^{\pi/2} L(\theta,\phi,\lambda)\cos(\theta)\sin\theta d\theta \tag{2.1}$$

$$E_u(\lambda) = -\int_0^{2\pi} d\phi \int_{\pi/2}^{\pi} L(\theta,\phi,\lambda)\cos(\theta)\sin\theta d\theta \tag{2.2}$$

$$E_o(\lambda) = \int_{4\pi} L(\theta,\phi,\lambda) d\Phi \tag{2.3}$$

All radiant quantities are location dependent, in particular on the altitude because of atmospheric and oceanic stratification. By definition, satellite sensors measure the top-of-atmosphere (TOA) radiance distribution. TOA is the given altitude, where air is so thin that atmospheric pressure or mass becomes negligible. Here, TOA is considered to be at 50 km and all heights above. Bottom-of-atmosphere (BOA) signals emerge at sea level or from land surfaces. The radiance and irradiance distributions within a water body are varying with depth and result from the incident radiance, the optical properties, and the reflectivity of the sea bottom.

Fig. 2.1 illustrates the attenuation of the light field for L, E_d, and E_u within a vertically inhomogeneous water body. The light field changes depending on varying optical properties, here examplified by the total extinction coefficient c_{total}. It can be seen that E_d and E_u show higher values than L because of the integration of all intensities over a hemisphere. Upwelling irradiances E_u have smaller values than downward irradiances E_d, because of light attenuation in both directions, downward and upward.

2.1.2 Apparent Optical Properties (AOPs) and Inherent Optical Properties (IOPs)

Apparent Optical Properties (AOPs)

Radiometric quantities of a water body depend on the directional structure of the ambient radiance field and the composition of the medium. Apparent optical properties (AOP) are differential properties such as ratios and depth derivatives of the radiance field (equations can be find in Tab. 2.1). They are used to indicate the rate of change of radiometric properties between different water bodies or within one water body, such as when, e.g., a phytoplankton bloom occurs. Passive optical remote sensing is a measure of AOPs, thus the sensors are called AOP sensors.

Commonly defined AOPs are reflectance R, remote-sensing reflectance R_{RS}, and diffuse attenuation k_d. In aquatic science also often used are water-leaving radiance L_W, which is the radiance

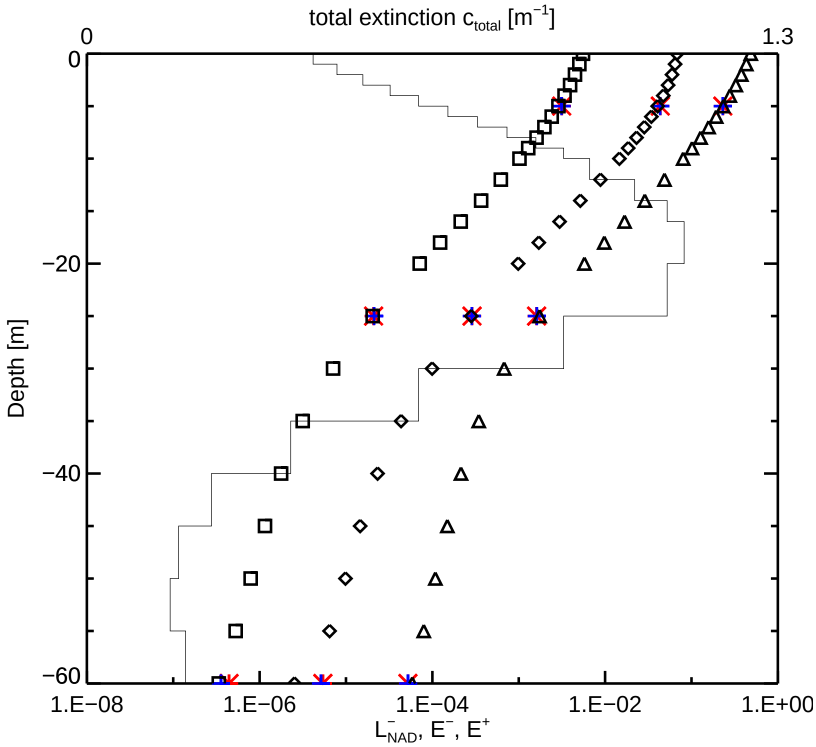

Figure 2.1: Underwater light field at 412.5nm (MERIS band 1) in lognormal scale for a vertically inhomogeneous medium with a bloom depth of -17m. The solid line is the total extinction coefficient corresponding to the upper x-axis. Shown are results for the radiant quantities: nadir radiances L_{NAD} (□), upward scalar irradiance E_u (◊), downward irradiance E_d (△). Colored stars denote comparisons to the Hydrolight model (Mobley et al., 1993) (red star) and the model by Bulgarelli et al. (1999) (blue star) for 5m, 25m, and 60m depth.

L at sea surface, and normalized water-leaving radiance L_{WN}, which is approximately the radiance exiting the sea surface in the absence of the atmosphere and with the sun at the zenith. Tab. 2.1 summarizes the most important radiant quantities and AOPs, all parameters are given at a distinct wavelength λ, which is omitted for brevity.

Inherent Optical Properties (IOPs)

If water is transilluminated by a light source, the modification of the radiant field is defined by the inherent optical properties (IOPs) of the water body. IOPs are properties of the hydrosols independent of the structure of the ambient light field. In other words, IOPs are in-water optical properties whose magnitude solely depend on the substance itself. In opposite to AOPs it is possible to measure IOPs in laboratories from previously taken and stored water samples.

Modeling the IOPs depends upon the scale the water body is analyzed. There are great differences in instrumentation and derived quantities between, e.g., single marine particles analyzed and the analyzation of large volumes of water. Bio-optical models consider the IOPs level of detail from specific to bulk optics. Specific IOPs provide the linkage between the concentrations

Table 2.1: Units and symbols of radiant quantities and apparent optical properties (AOPs).

Quantity	Symbol	Equation	SI Unit
water-leaving radiance	L_W	–	$[W\,m^{-2}\,sr^{-1}]$
normalized water-leaving radiance	L_{WN}	$E_0\,\frac{L_W}{E_d}$	$[W\,m^{-2}\,sr^{-1}]$
remote-sensing reflectance	R_{RS}	$\frac{L_W}{E_d}$	$[sr^{-1}]$
radiance reflectance	R_W	$\pi\,\frac{L_W}{E_d}$	$[-]$
normalized water-leaving reflectance	R_{WN}	$\pi\,\frac{L_{WN}}{E_0}$	$[-]$
irradiance reflectance, irradiance ratio	R	$\frac{E_u}{E_d}$	$[-]$
diffuse attenuation coefficient for downward irradiance	k_d	$\frac{dE_d}{dz}\,\frac{-1}{E_d}$	$[m^{-1}]$

of compounds and resulting bulk IOPs.

AOPs and IOPs are often referred to as geophysical parameters, whereas the in-water constituent concentrations are called bio-geophysical parameters.

2.1.3 Single-particle IOPs and Mie Theory

Referring solely to specific IOPs of particles, often the term single-particle optics is used. Considerung a single, individual particle, e.g., an algal cell, the particle is assumed to be a homogeneous sphere. Mathematical functions for non-spherical particles are much more complicated to derive than for sphericals as the particle shape, internal geometry and its surface roughness have to be taken into account [Chen and Stamnes (1998), Hovenier (2000)]. Quirantes and Bernard (2004) show in their study a minor dependence of extinction and scattering efficiencies on the particles shape, but a high sensitivity of the backscattering efficiency. All these single-particle optical properties are introduced in this section.

The complex index of refraction of a spherical particle, comprising its scattering properties, is denoted:

$$m_r = n_r - ik_r. \tag{2.4}$$

The imaginary part of the refractive index k_r gives the extinction of light passing through the particle. The real part of refractive index n_r describes how the light is redirected or scattered as is passes the particle.

Optical properties, as the absorption and the scattering coefficient or the volume scattering function (all properties are introduced in section 2.1.4) can be calculated by the complex index of refraction and applying an optical method called *Mie Theory*. The method was published by Mie in 1908 and can be found in Hulst (1957) or Bohren and Huffman (1983).

Mie's solution can be presented in terms of absorption and scattering efficiencies, or total absorption and total scattering cross sections σ_a and σ_b. Efficiency Q gives the fraction of intensity incident on a sphere that is absorbed or scattered by the sphere. The optical efficiency factors for absorption and scattering (Q_a, Q_b) are the main quantitative characteristics of extinction by a single spherical particle. Cross section σ in [m^2], obtained from *Mie Theory*, is the area of the incident beam that has an intensity equal to the power absorbed or scattered by the sphere. Cross sections σ depend on the complex refractive index m_r, the number density of the particle n or the cell population size distribution of the particles n_D, and on wavelength λ of the incident light.

$$\sigma(D, m_r, \lambda) \ \equiv \ QA = Q\frac{\pi D^2}{4} \tag{2.5}$$

In aquatic optics, the particle-specific cross sections are often called specific IOPs, or mass-specific IOPs. Here, for absorption and scattering cross sections σ_a and σ_b, equivalently the terms specific absorption coefficient a^* and specific scattering coefficient b^* are used:

$$\sigma_a(\lambda) \ \equiv \ a^*(\lambda), \tag{2.6}$$

$$\sigma_b(\lambda) \ \equiv \ b^*(\lambda). \tag{2.7}$$

From cross sections σ the bulk optical properties can be derived.

2.1.4 Bulk IOPs

Radiative transfer theory utilizes macroscopic quantities such as bulk IOPs. Remotly measured radiant intensities refer to, e.g., the bulk IOPs of a volume of water and the combined effects of all in-water compounds. Bulk IOPs are linked to single-particle or specific IOPs via the concentration. Fig. 2.2 illustrates the radiant quantities described by the optical properties commonly used in water optics.

The bulk IOP coefficient γ is the product of the particle-specific cross section σ and the number density n of the particles in case of mono-specific compositions with constant size distribution:

$$\gamma(\lambda) \ = \ \sigma(\lambda)\, n. \tag{2.8}$$

In case of mixtures, the contributions of all individual particles are summed up:

$$\gamma(\lambda) \ = \ \int_{all m_r} \int_{all D} \sigma(D, m_r, \lambda) n(D) dD dm_r. \tag{2.9}$$

D denotes the diameter of the sphere of the geometric cross sectional area, λ the wavelength of the incident light, m_r the complex refractive index, and n_D the cell population size distribution of the particles.

The bulk IOP coefficients $\gamma(\lambda)$ are the absorption coefficient $a(\lambda)$, the scattering coefficient $b(\lambda)$, and the extinction coefficient $c(\lambda)$ in units of [m^{-1}]. λ denotes the spectral dependancy. Sometimes, the scattering coefficient b is referred to as the total scattering coefficient to highlight that the scattering process over the whole solid angle is meant. In comparison, the differential scattering coefficients back-scattering and forward-scattering coefficients (b_b, b_f) indicate the scattering at angles from 90° to 180°, respectively in the range of 0° to 90°.

The extinction coefficient, i.e. the beam attenuation coefficient, c is the sum of absorption and scattering:

$$c(\lambda) \ = \ a(\lambda) \ + \ b(\lambda). \tag{2.10}$$

The combined rate of radiant intensity loss due to absorption and scattering processes of all constituents x can be summed up as:

$$\gamma_{total}(\lambda) \;=\; \sum_{x=m}^{n}(\gamma_x(\lambda)). \tag{2.11}$$

Correspondingly, γ_{total} is the total extinction coefficient c_{total}, the total scattering coefficient b_{total}, and the total absorption coefficient a_{total}.
From extinction and scattering coefficients, the single-scattering albedo ω_o can be derived.

$$\omega_o(\lambda) \;=\; \frac{b(\lambda)}{a(\lambda)\;+\;b(\lambda)} \tag{2.12}$$

In plane-parallel water bodies, optical depth or optical thickness τ is defined as the extinction coefficient integrated over a geometrical depth z, where optical depth τ is non-dimensional:

$$\tau(\lambda) \;=\; \int c(z,\lambda)dz. \tag{2.13}$$

Transmission $\mathcal{T}$ is the intensity transmitted through an optical medium and is defined as:

$$\mathcal{T}(\lambda) \;=\; e^{-\tau(\lambda)} \;=\; e^{-\int c(z,\lambda)dz}. \tag{2.14}$$

Therefore, the extinction c is the logarithmic expression of the transmission $\mathcal{T}$.
Scattering implies a change in direction of the incident beam and total scattering can be partitioned into its angular components. The non-normalized scattering function is called volume scattering function (VSF) $\beta(\Psi)$, with dimensions of [$\mathrm{m}^{-1}\mathrm{sr}^{-1}$]. The VSF quantitatively describes the directional dependency of the intensity L of electromagnetic radiation scattered by the particle. Ψ is the scattering angle. The polarizational state of light is neglected here. The dependence of the VSF on the azimuth angle ϕ is negligible due to the assumption of spatially homogeneous particles with an axial symmetrical scattering function.

$$\beta(\Psi,\lambda) \;=\; \lim_{dV\to 0}\frac{dL(\Psi,\lambda)}{E(\lambda)\;dV} \tag{2.15}$$

Physical interpretation of the VSF is the scattered intensity L (per unit incident irradiance E) scattered per unit volume dV of water. Considering no internal sources and only contributions from elastic scattering processes, integrating the VSF over all solid angles gives the total scattering coefficient b. Ψ is the solid scattering angle.

$$\beta(\Psi,\lambda) \;=\; b(\lambda)\;p(\Psi) \tag{2.16}$$

Deviding the VSF by scattering coefficient b yields the scattering phase function $p(\Psi)$ in units [sr^{-1}]. This allows the division of scattering processes into a factor of *strength* b and a factor of *angular distribution* $p(\Psi)$, which is independent of the particle concentration. Often it is convenient to approximate the shape of the phase function by an analytic formula. Formulas most commonly used are Henyey-Greenstein and Fournier-Forand scattering phase functions (Zhang et al., 2003). From *Mie Theory* the exact phase function $p(\Psi)$ can be obtained.

2.1.5 The Equation of Radiative Transfer (RTE)

Measured radiant quantities, such as extinction c or the VSF, can be physically characterized and modeled using radiative transfer theory. Radiative transfer theory aims to describe the interaction of light with matter and to quantify all the processes that affect the direction and the quantity of photons. Intensity changes dL are due to extinction processes, which are absorption or scattering of photons out of the light beam, and due to intensivation by scattering into the direction of light propagation or by emission. The rate of increase of radiance is expressed via source function J. The emission part of source term J has only to be considered for all wavelengths longer than $3\,\mu$m.

The loss of radiance dL is proportional to extinction c at the optical depth τ along an infinitesimal optical path length $(d\tau/\cos(\theta))$. $\cos(\theta)$ is the cosine of the zenith angle θ, ϕ is the azimuth angle.

$$dL(\tau,\cos(\theta),\phi) \;=\; -\,L(\tau,\cos(\theta),\phi)\frac{d\tau}{|\cos(\theta)|} \tag{2.17}$$

The change of a monochromatic intensity is equivalent to the balance of light loss and gain, which gives the standard differential radiative transfer equation (RTE):

$$\frac{dL}{cdz} \;=\; |\cos(\theta)|\frac{dL}{d\tau} \;=\; -\,L \;+\; J. \tag{2.18}$$

For efficient numerical treatment radiative transfer is calculated for diffuse and direct solar radiation independently. Diffuse light is the at least once scattered part of the radiation. The non-diffused solar radiation is called direct solar beam radiation. Different methods exist to solve the RTE, analytically or numerically. The radiative transfer model MOMO, used in this study, is a numerical solution of the RTE. Details are given in section 3.1.

The RTE for, e.g., an oceanic situation comprising a plane-parallel assumption without inernal sources (i.e. inelastic scattering or emission) for a vertically homogeneous medium can be written as

$$\cos(\theta)\frac{dL(\tau,\lambda,\theta,\phi)}{d\tau} \;=\; -\,L(\tau,\lambda,\theta,\phi) \;+\; \omega_o(\lambda)\int_0^{4\pi} p(\cos(\theta))L(\tau,\lambda,\theta'\phi')d\Psi. \tag{2.19}$$

From Eq. (2.19) and Eq. (2.13) it is evident that total extinction coefficient c, single-scattering albedo ω_o, and scattering phase function p completely describe the IOPs of an isotropic, plane-parallel medium. In this study, the extinction coefficient c and the single-scattering albedo ω_o are calculated from the bulk absorption and scattering coefficients (a, b), which are based on the specific IOPs. The phase function $p(\Psi)$ is obtained from published measurements or or the Fournier-Forand scattering phase function model in combination with *Mie Theory* as derived by Zhang et al. (2003).

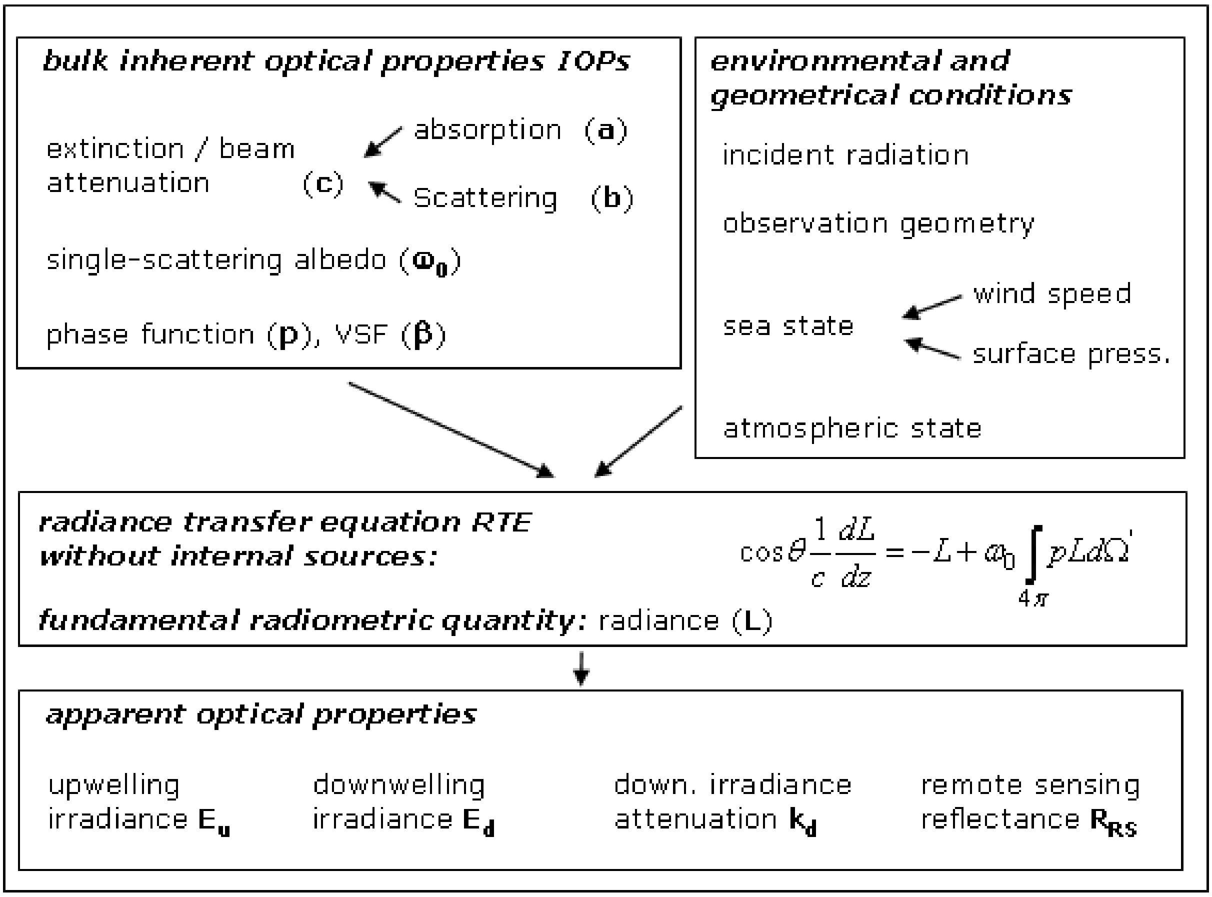

Figure 2.2: Radiant quantities described by AOPs and IOPs, commonly used in water optics.

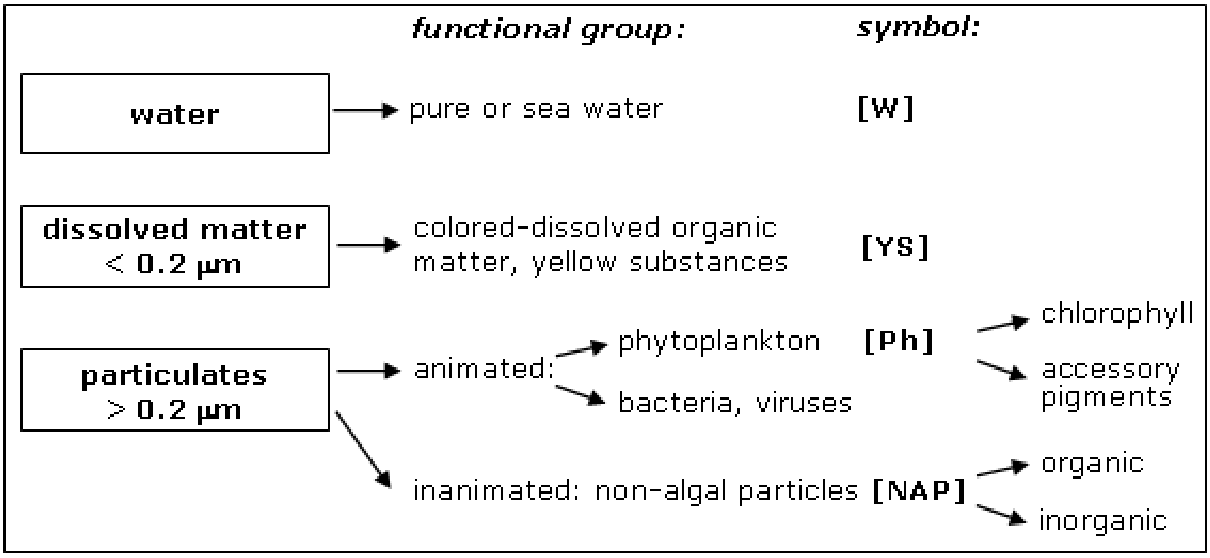

Figure 2.3: Schematic overview of in-water constituents as used in this study. A desription is given in section 2.2.1

2.2 Biology of Marine Water Bodies

This section gives background information on optical properties of natural water bodies, their biology and composition. All components in the ocean contribute to the bulk optical properties of a water body. A concept of 5 groups of in-water substances is presented and the relevant notations are given on the basis of Babin (2000). Further on, basics are given to phytoplankton species differentiation and the pyhtoplankton bloom cycle in the oceans to initialize chapters 4 and 5.

2.2.1 Compounds of Natural Waters

Natural water is composed of constituents of a large range of sizes: from water molecules with sizes of about 0.1 nm to large microplankton of 100 μm diameter. These constituents can be divided into particulate and dissolved matter. A differentiation between compounds of organic or inorganic origin as well as their living or non-living nature is also well established. Fig. 2.3 on page 14 gives a schematic overview on in-water compounds as used in this study. Symbols in Fig. 2.3 are given according to this section.

Following the definition given in the MERIS protocols on *in-situ* measurements (Doerffer, 2002) all in-water constituents that pass a membrane filter with a pore size of 0.2 μm are called dissolved. Everything remaining on the filter and thus larger than 0.2 μm is called particulate. 0.2 μm is the smallest particle size resolvable under an optical microscope.

From small to larger compound sizes, the most important groups of light-influencing components are described here. The section is mainly based on fundamentals given in Kirk (1994) and Mobley (1994).

Pure water and seawater (W): Pure or distilled water consists exclusivly of water molecules. In small quantities water appears colourless. Oceanic waters on sunny days clearly show a blue colour, which is caused by water molecules' weak absorption in the blue and green region, but strong absorption in the red region of the electromagnetic spectrum. At wavelengths above 550 nm absorption increases significantly, above 700 nm it is the predominant feature of the water spectrum. Seawater consists of pure water plus dissolved salts. On practical salinity scale (psu) the sea salt content varies between regions typically from 7 psu, e.g., in the Baltic Sea, to 38 psu. In open oceans the average value is 35 psu. Sea salts have a negligible effect on absorption in the visible photosynthetic spectral range but cause an increase in scattering (Pegau et al., 1997). The water absorption coefficient is temperature dependent in the near infrared portion of the spectrum (Pegau et al., 1997). The spectral behaviour is illustrated in Fig. 3.2. In the following, symbol W is used to indicate seawater.

Dissolved organic compounds (YS): When organic matter decomposes, most of it is broken down by microbial actions to carbon dioxide and inorganic forms of nitrogen, sulphur, phosphorus as well as a complex group of humic and fulvic acids referred to as *yellow substances*, *gelbstoff*, *gilvin* or *chromophoric dissolved organic matter* (CDOM). All natural waters contain varying concentrations of CDOM with highest concentrations in rivers, lakes and coastal waters because of decayed terrestrial vegetation. CDOM dominated waters show a yellow to brown color. CDOM strongly absorbs in the blue region of the spectrum with an exponential decrease towards longer wavelengths. Spectral absorption signatures are shown in Fig. 4.8. CDOM is supposed to be non-scattering material. For consistent terminology with MERIS protocols (Doerffer, 2002) the symbol YS is used to denote CDOM.

Animated particulates (Ph): Animated or living organic particles, larger than 0.2 μm membrane filter size, are defined to be microalgae or phytoplankton. Phytoplankton are microscopic plants which occur in a wide diversity of species, shape and concentrations. Cell sizes range from 1.0 μm to more than 200 μm. Photosynthetic pigments, most important chlorophyll-a, within the algal cells absorb the light strongly in the blue and the red part of the spectrum showing distinct absorption features. Most phytoplankton species are much larger than the wavelength of visible light, thus they are efficient scatterers with strong scattering in the forward direction and a small contribution to backscattering. Examples on different spectral signatures are shown, e.g., in Fig. 4.3. Symbol for Phytoplankton is Ph. In most studies the chlorophyll-a pigment is used as a proxy for phytoplankton biomass and Ph is parameterized in terms of chlorophyll-a concentration, denoted as $[Chla]$. If Ph is parameterized to the sum of concentrations of all chlorophyll containing phytosynthetic pigments and the accessory phycoerythrin pigment, denoted as $[TChl]$. Units for $[Chla]$ and $[TChl]$ are [mgm^{-3}].
From the three plankton functional groups zooplankton, phytoplankton, and bacterial plankton, only phytoplankton ist considered within a bio-optical water model. Here and in most hydro-optical models, bacteria are defined to be associated with phytoplankton (Babin, 2000), zooplankton is neglected.

Inanimated organic particulates (NAP1): Inanimated or non-living particles of organic origin are called *organic detritus* or *organic suspended solids* (OSS). They are produced when algal cells die or break. The IOPs of organic detritus are not that well characterized as CDOM due to the wide range of material. Organic detritus shows significant absorption only at blue wavelengths. Detritus can be treated as an particle group associated to phytoplankton. To measure detrital absorption, it is separated from phytoplankton pigment absorption by bleaching the pigments on a glass fibre filter holding all suspended material. The MERIS protocol (Doerffer, 2002) defines the combined absorption by yellow substance and bleached particles (YSBPA), which is the bleached particles absorption (BPA) added to the spectral absorption coefficient of YS.

Inanimated particulates (NAP2): Inanimated or inorganic particles or sediments consist of minerals, quartz sand or metal oxids. Their sizes range from 1.0 to 100 μm. High loads of inorganic particles decisively influence total scattering yielding in turbid waters. In other studies, the terms *sediments* (sed) or non-algal particles NAP are used to define inorganic particles.

In general, different notations exist for non-living organic and inorganic particles. Accumulated non-living organic and inorganic particle concentration, parameterized as particles dry weight, is sometimes denoted as total suspended matter (TSM). In this study, the term non-algal particles (NAP) is used for sum of all organic an inorganic particles other than phytoplankton (Babin et al., 2003), Ph is used for Phytoplankton, YS for yellow substances, and W for seawater.

Particles larger than 100 μm such as living zooplankton or non-living particles of various kind can cause strong optical effects but they have not been quantified in bio-optical models. Other optically significant effects caused by airbubbles, foam or sunglint are addressed in section 3.1.4.

2.2.2 Phytoplankton and Phytoplankton Bloom Events

Phytoplankton Classification and Phytoplankton Functional Types (PFTs)

Detailed descriptions on the biology of phytoplankton and their classification can be found, e.g., in the books from Rao (2006) and Kirk (1994). As lined out in the previous section, phytoplankton is one optically active compound amongst others. During an algae bloom, phytoplankton is dominating the water-leaving signal.

In biological literature, phytoplankton species are ranked into divisions and classes on basis of their distribution of pigments in the algal cells. For example in the Baltic Sea and the North Atlantic, the phytoplankton species dinoflagellates (division: Pyrrophycophyta, class: Dinophyceae) and the diatom division, i.e. Bacillariophyta, contribute to spring blooms. Strong blooms of coccolithophores (division: Haptophyta, class: Prymnesiophyceae), with most abundant species *Emiliania huxleyi*, do appear in the North Atlantic on regional scale. Dinoflagellates, diatom species, and coccolithophores are the dominating producers of primary biomass in the global oceans. In the Baltic Sea, *Nodularia spumigena* and *Aphanizomenon flos-aquae*, species of the division Cyanophyta (cyanobacteria, blue-green algae or bacteria) occure as dominating phytoplankton in very intense summer blooms.

Ancillary to the biological classification, Sieburth et al. (1978) separated phytplankton into size classes of picophytoplankton (0.2 to 2 μm), nanophytoplankton (2 to 20 μm), microphytoplankton (20 to 200 μm), and mesophytoplankton (200 μm to 2 mm). Macrophytoplankton are all marine plants larger than 2 mm.

From bio-geochemical perspective a size-based classification alone is not sufficient, since the functional role of phytoplankton in marine ecosystems also depends on the nutrient, iron, or light uptake. Again, for satellite remote sensing purposes, a biological species dependend classification is too specified. Thus, a combination of both is applied and phytoplankton is classified into Phytoplankton Functional Types (PFTs), based on their bio-geochemical role in the marine ecosystem. Following Nair et al. (2008), PFTs are pico-autotrophs, nitrogen-fixers, calcifiers, silicifiers, and dimethylsulfid (DMS) producers. The classification of phytoplankton into functional types is complex as, e.g., the species *Emiliania huxleyi* is a calcifier and a DMS producer.

Phytoplankton Bloom Cycle

A phytoplankton bloom, i.e. an algae bloom, is a sudden increase of a phytoplankton population (Smayda, 1997a). Sufficient sunlight and available nutrients, favorable for the respective phytoplankton species, initialize its massive growth. Most phytoplankton blooms such as spring- and autumn blooms are natural occurences benefitial to the ecosystem. Only few blooms appear harmful to the ecosystem due to their intense occurence, large dispersion, their long duration, and their mechanical or toxic harmfulness.

A typical bloom lifecycle shows a well defined pattern of phytoplankton growth. It spans from the initiation via an often exponential growing, to the maximum stagnation phase, and finally a slow decline of phytoplankton biomass (Smayda, 1997a,b). Oceans in temperate climate zones, as the Baltic Sea and the North Atlantic, often show highest phytoplankton abundance in spring time with a secondary peak in autumn. Detailed decription of the annual cycle in the Baltic Sea is giving in the beginning of chapter 4. For information on the North Atlantic it is referred to chapter 5.

The phytoplankton bloom cycle is controlled by the availability of solar light and nutrients in the water. The heating of surface waters in spring stimulates the growing of pyhtoplankton in the nutrient enriched water from well mixed winter season. The phytoplankton stops growing in summer when all nutrients have been used up. Less available solar light in autumn leads to a cooling of the surface water and to mixing with deeper waters, which favors a second phytoplankton bloom. During winter, ocean water is well mixed and nutrients enter surface waters while low solar light availability limits phytoplankton growth.

Chapter 3

A Processing System for Envisat MERIS Data to Recognize Specific Phytoplankton Blooms

To interprete remote sensing data, algorithms are needed to retrieve the desired geophysical quantities. This study utilizes a particular processing system in which bio-geophysical quantities of a water body are derived from Envisat MERIS data. MERIS satellite data are characterized in the last section of this chapter (section 3.4).
Each step of the algorithm development is described in this chapter, a schematic overview is shown in Fig. 3.1. Procedures similar to the one presented here have been succesfully applied to visible ocean remote sensing as, e.g., the standard MERIS algorithm for coastal waters (Schiller and Doerffer, 1999) or the coastal water algorithm developed by Schroeder et al. (2007a). The method is based on radiative transfer (RT) forward simulations (section 3.1) and a regression performed by an artificial neural network (ANN) technique (section 3.2). A discussion of limitations of the used method can be found in section 3.2.3.

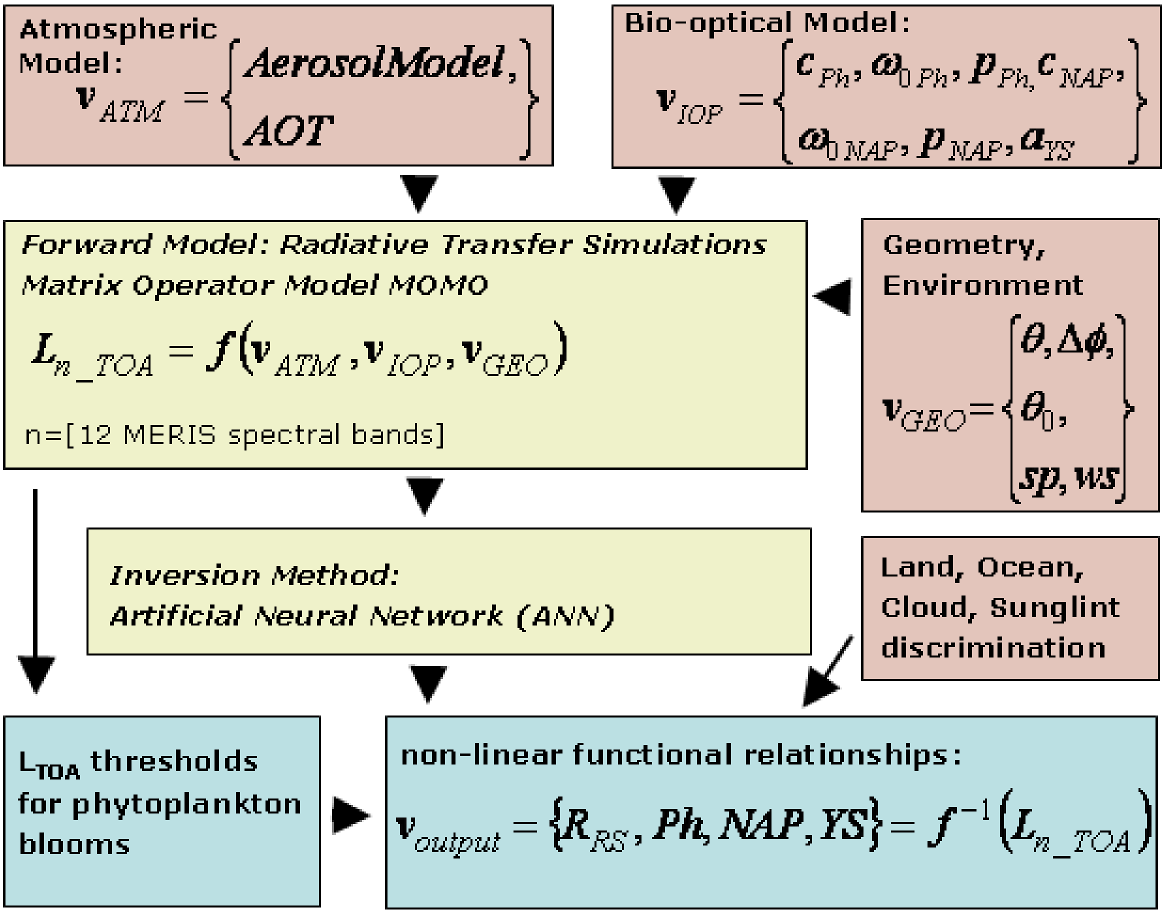

Figure 3.1: Schematic overview of the processing system.

3.1 The Forward Model

3.1.1 The Radiative Transfer Model MOMO: Radiative Transfer Simulations

Physical-mathematical models to calculate radiative transfer (RT) in the visible (VIS) and near-infrared (nIR) spectral range are various. However, to calculate radiance fields in coupled atmosphere-ocean systems only few models exist. Besides the Matrix-Operator MOdel MOMO (Fell and Fischer, 2001) used in this study, well known and widely validated models are, e.g., the Bulgarelli model based on the Finite Element Method (Bulgarelli et al., 1999) or the 6SV1 model (Second Simulation of a Satellite Signal in the Solar Spectrum, Vector, version 1) (Kotchenova et al., 2006). The Hydrolight model (Mobley, 1989), often used in ocean science communities, computes exclusively underwater light fields and does not account for the atmosphere.
MOMO is based on the work of Fischer (1983), Fischer and Graßl (1984), and Fell and Fischer (2001). An extensive discription of the numerical treatment of RT within MOMO can be found in Fell (1997) and Fell and Fischer (2001). The MOMO code, based on the matrix-operator method, calculates the radiation field in a stratified, coupled atmosphere-ocean system, which

is considered as a plane-parallel medium with optical properties depending only on the vertical coordinate. Therefore, MOMO is a 1-dimensional model. The plane-parallel, thus non-spherical, assumption is valid, since small horizontal areas of abut $1\,\mathrm{km}^2$ are considered here.

The main advantage of the matrix-operator method regards to its computational speed for calculations in optically dense media like clouds and water. The code calculates monochromatic azimuthally resolved radiances at a number of zenithal observation angles for all pre-defined depth levels and given solar incident angles. Physical processes of multiple scattering and the treatment of the sea surface as flat or rough are included in MOMO. Inelastic scattering processes are not accounted for in this setup. A vertical profile of optical properties can be considered by dividing the medium into a number of homogeneous layers.

The MOMO code was described and validated against other radiative transfer models in Fell and Fischer (2001). For selected problems of RT in atmosphere-ocean systems, the model intercomparisons show good numerical accuracy and computational efficiency for MOMO predictions. Differences reach maximal values of 5% for solar zenith angles smaller than 60° and observation zenith angles smaller than 30°. The comparison to the analytical solution of the RTE for semi-infinite atmospheric Rayleigh scattering show derivations smaller than 0.1% for solar and observation zenith angles smaller than 60°.

3.1.2 Bio-optical Model for Inherent Optical Properties of Water Bodies and Phytoplankton Blooms

Previous chapter 2 presented an overview of optically active in-water constituents. In the following, parameterizations of bulk inherent optical properties (IOPs) in relation to the concentrations of in-water compounds are given. They are presented in a form suitable for the use within a RT model, therefore the extinction coefficient c, the single-scattering albedo ω_o, and the phase function p are calculated.

Bio-geophysical parameters measured *in-situ* or derived from visible spectral satellite radiometry data are, e.g., absorption by yellow substances (YS), non-algal particle (NAP) concentration, and phytoplankton concentration (Ph) given as the concentration of chlorophyll-a $[Chla]$. In case of visible, multi spectral remote sensing, the conversion into YS, NAP, and Ph is from the spectral depending bulk absorption and scattering coefficients, as described in more detail in following paragraphs.

Different oceanic conditions demand an adjusted parameterization within an appropriate bio-optical model setup. For example, waters dominated by mono-specific phytoplankton blooms require an IOP parameterization including the phytoplankton group specific optical properties. Here, the choosen parameterization setup is outlined in general. It is suitable for optically complex waters with more than 1 varying in-water compound. Setups for the specific phytoplankton types cyanobacteria and coccolithophores are given explictely in chapter 4 and chapter 5.

Four-Component Model for Absorption

The total absorption coefficient is calculated by summing the absorbing contributions from all optically active components. For general setup, in this study four groups of in-water compounds are choosen to contribute to total absorption:

$$a_{total}(\lambda) = a_W(\lambda) + a_{YS}(\lambda) + a_{NAP}(\lambda) + a_{Ph}(\lambda). \quad (3.1)$$

Contributing constituents are seawater a_W, yellow substance a_{YS}, non-algal organic and inorganic particles a_{NAP}, and photosynthetic phytoplankton pigments a_{Ph}.

The spectral data of a_W is taken from Pope and Fry (1997) for the 412 nm to 727.25 nm spectral range and from Hale and Querry (1973) for all longer wavelengths (water temperature: 20°C). a_W is increasing with wavelength as displayed in Fig. 3.2.

Spectral absorption by YS is modeled as an exponential function decreasing towards longer wavelengths as suggested by Bricaud et al. (1981) with varying slopes S_{YS} depending on the geographical region. $a_{YS}(443)$ is the bio-geophysical parameter to be retrieved. S_{YS} is defined in chapters 4 and 5.

$$a_{YS}(\lambda) = a_{YS}(443)\exp(-S_{YS}(\lambda - 443)) \quad (3.2)$$

Non-algal organic and inorganic particle absorption is modeled as introduced by Babin (2000) with varying absorption coefficient $a_{NAP}(443)$ and varying slope S_{NAP}, both defined in chapters 4 and 5.

$$a_{NAP}(\lambda) = a_{NAP}(443)\exp(-S_{NAP}(\lambda - 443)) \quad (3.3)$$

The spectral absorption coefficient of phytoplankton pigments is calculated using the model of Bricaud et al. (1995) with tabulated coefficients A_{Ph} and B_{Ph}:

$$a_{Ph}(\lambda) = A_{Ph}(\lambda)[Chla]^{B_{Ph}(\lambda)}. \quad (3.4)$$

All absorption coefficients for YS, NAP, and Ph corresponding to blooms of cyanobacteria and coccolithophores are discussed in chapter 4 and chapter 5, respectively.

Three-Component Model for Scattering

YS is assumed to be non-scattering matter, thus, for general outline the scattering phase functions and scattering coefficients have to be defined for three components.

In this study, the total scattering coefficient is the sum of the three compounds seawater W, non-algal particles NAP, and phytoplankton Ph.

$$b_{total}(\lambda) = b_W(\lambda) + b_{NAP}(\lambda) + b_{Ph}(\lambda) \quad (3.5)$$

The spectral scattering coefficient for seawater is modeled as Morel (1974) and is valid for global salinity average of 35 psu. The seawater scattering coefficient is decreasing with wavelength as illustrated in Fig. 3.2. This Figure also shows a higher seawater scattering coefficient for a higher seasalt content. For more detailed information it is referred to the work by Zhang et al. (2009), who recently investigated in the salinity effect on seawater scattering.

$$b_W(\lambda) = 0.00288(\frac{\lambda}{500})^{-4.32} \quad (3.6)$$

Seawater phase function is modeled after Morel (1974):

$$p_W(\Psi) \;=\; 0.06225(1 + 0.835\cos^2\Psi). \tag{3.7}$$

As written in Eq. (2.15) the VSF for seawater $\beta_W(\lambda, \Psi)$ can be calculated from Eq. (3.6) and Eq. (3.7), examples for three wavelength are shown in Fig. 3.2.

From optical *in-situ* measurements only the combined contributions from Ph and NAP on the scattering coefficient can be directly assessed. Therefore, the scattering coefficient is related to the mass-specific scattering coefficient of particles b^*_{TSM} and the total particle concentration $[TSM]$ (Babin et al., 2003):

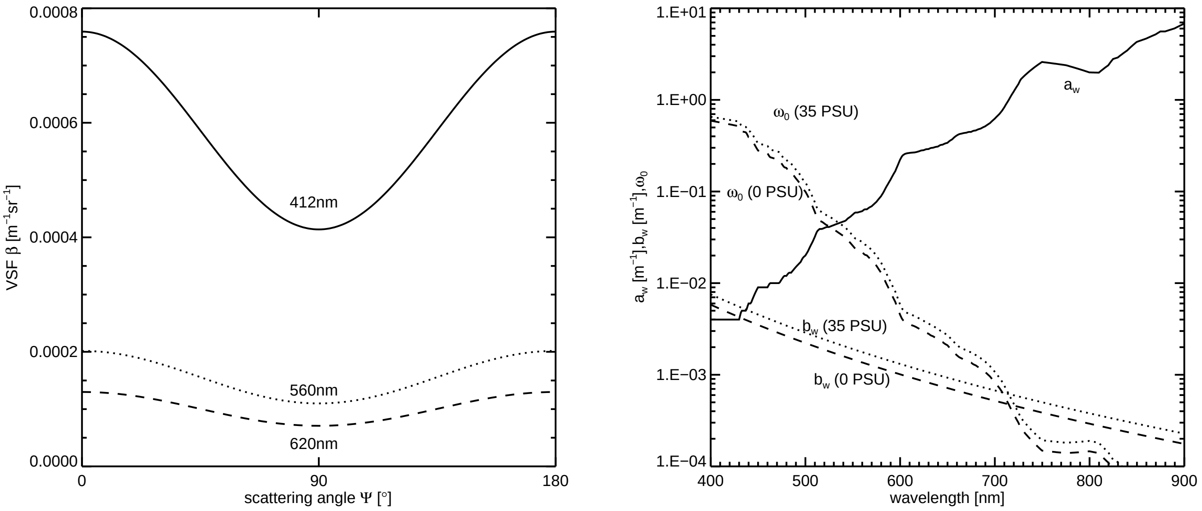

Figure 3.2: Volume scattering function of seawater for three wavelengths (left). Spectral dependance of pure and seawater: scattering coefficient b_W for 0 and 35 psu, absorption coefficient a_W, single scattering albedo ω_o and scattering coefficient b_W for 0 and 35 psu (right).

$$b_{TSM}(\lambda) \;=\; b^*_{TSM}(\lambda)[TSM]. \tag{3.8}$$

Ph spectral bulk scattering coefficient b_{Ph} and phase fundtions p_{Ph} are highly varying between phytoplankton species. Phase functions p for the sum of Ph and NAP are calculated from *Mie Theory* and applying the Fournier-Forand phase function model in the form given by Zhang et al. (2003).

Choosen parameterizations of b_{ph}, b_{NAP}, p_{Ph}, and p_{NAP} for the phytoplankton bloom cases concerned in this study, are given in chapter 4 and chapter 5.

From the bulk absorption (a_x) and scattering (b_x) coefficients of in-water compounds x the extinctions coefficients c_x and the single-scattering albedos ω_{ox} are calculated according to

Eq. (2.10) and Eq. (2.12), respectively. Comprising the output of the bio-optical water model used for the RT calculations, a vector containing all bulk optical properties is written:

$$\begin{aligned} v_{IOP}(\lambda) = \{ & c_W(\lambda), \omega_{oW}(\lambda), p_W(\Psi), \\ & c_{Ph}(\lambda), \omega_{oPh}(\lambda), p_{Ph}(\Psi), \\ & c_{YS}(\lambda) = a_{YS}(\lambda), \omega_{oYS}(\lambda) = 0, \\ & c_{NAP}(\lambda), \omega_{oNAP}(\lambda), p_{NAP}(\Psi)\}. \end{aligned} \tag{3.9}$$

3.1.3 Description of the Atmospheric Model and the Geometry Setup

The TOA signal measured at satellite sensor height is influenced by atmospheric, oceanic, and coupled atmosphere/ocean effects. The oceanic contribution is very little compared to the atmospheric contribution. According to the Earth's solar energy budget (Solomon et al., 2007) on global and spectral average only 13% of the measured VIS intensities at TOA originate from the reflection of incoming solar light at the Earth's surface. The major fraction originates from atmospheric processes and the reflection at clouds. Ocean satellite remote sensing in the VIS and nIR spectral range is only possible for cloudfree conditions. All other atmospheric effects have to be accounted for to extract information on the oceans as described here.

In the VIS and nIR spectral range following physical processes change photon paths in the atmosphere and have to be accounted for in the RT model: (a) Rayleigh scattering of direct and diffuse sunlight at air molecules, (b) absorption by atmospheric gases (ozone O_3, oxygen O_2, water vapor H_2O), (c) Mie scattering and absorption by aerosols and clouds. Air molecules, such as nitrogen (N_2), carbon dioxid (CO_2), ozone (O_3) and others, are much smaller than the incident radiance of the VIS and nIR spectral range, therefore the Rayleigh scattering model can be applied. The scattering properties of all other atmospheric compounds with sizes larger than the incident radiance wavelength are modeled as defined by *Mie Theory.* Some atmospheric gases also show strong absorption patterns in the VIS/nIR spectral range, which is taken into account.

Due to the high number of atmospheric variables, a model parameterization is choosen to approximate the atmospheric influence and provide suitable input for RT calculations. The atmospheric model is characterized as given in Schroeder et al. (2007a). All input parameters for the atmospheric setup as well as geometrical and environmental assumptions are reported in the following.

Vertical profiles of atmospheric pressure, temperature, and humidity are taken from the U.S. standard atmosphere (Anderson et al., 1986). The atmosphere model is defined to consist of 11 homogeneous, parallel layers, with the upper layer at 50 km. Eight aerosol layerings with 4 relative humidities and five different aerosol optical depths, distributed within the 11 model layers, are used to simulate the radiance fields. The setup of the aerosol models is illustrated in Fig. 3.3. O_3 loading is taken to be a constant of 344 DU for the simulations. Two different surface pressures and wind speeds are considered. 12 MERIS wavelengths are used to compute radiance L_{TOA} at TOA and remote-sensing reflectance R_{RS} just above sea surface: 412.5, 442.5, 490, 510, 560, 620, 665, 709.5, 753.5, 778.5, 865, and 885 nm. Simulations are done at 17 solar and observation zenith angles (θ_0,θ) between 0° and 87°. 25 azimuth angles ϕ are set up with equal spacing between 0° and 180°. Multiplying all varying components, which are also listed in Tab. 3.1 for a general overview, it gives a total of 160 combinations of atmospheric and environmental conditions for each wavelength as input for the RT calculations. A vector containing all varying atmospheric parameters is written as:

$$\begin{aligned} v_{ATM}(\lambda) \; = \; & \{8\, Aerosol\, Models(\lambda), 5\, AOTs(\lambda), \\ & 2\, surface\, pressures, 2\, wind\, speeds\}. \end{aligned} \tag{3.10}$$

Fig. 3.4 on page 27 illustrates some examples of the aerosol part of the atmosphere model. Five different aerosol optical thicknesses (AOT) are defined at 550 nm. Depending on the aerosol model and the relative humidity, AOTs for all other MERIS wavelengths are calculated.

Table 3.1: Parameterization of the atmosphere model, see also Schroeder et al. (2007a).

Component/Property	Value range
U.S. standard atmosphere	gaseous absorption of O_3, O_2, H_2O, geometrical upper limit: 50 km
number of model layers	11
ozone loading	344 DU
8 aerosol layerings:	
with 4 relative humidity	70,80,95,99%
5 aerosol optical thicknesses (AOT)	0.03,0.1,0.3,0.5,1 at 550nm
2 surface pressures (sp)	980, 1040 hPa
2 wind speeds (ws)	1.5,7.2 ms^{-1}
for 12 MERIS wavelengths	412.5,442.5,490,510,560,620, 665,709.5,753.5,778.5,865,885 nm

3.1.4 Further Effects and Model Restrictions

Beside the optically active in-water compounds (3.1.2) and the atmosphere (3.1.3), different physical processes impact the radiance field. The impacts not considered in the setup of this work are discussed in the following.

Polarization: All scattering processes by molecules, aerosols, hydrosols, and sea surface reflection introduce and modify the polarization state of radiation. In this study a non-polarized setup of MOMO is choosen, since the MERIS sensor does not provide information on polarization. For the polarized version of MOMO it is referred to Boettger et al. (2005). Also, in optical oceanography, polarization in combination with *in-situ* or remotely sensed data has not been widely used. Based on the polarized RT model OSOA, Chami (2007) studied polarization effects in open ocean and coastal waters theoretically and showed low polarization sensitivity measureable at TOA for varying chlorophyll-*a* concentrations in phytoplankton dominated waters. The results suggest to use information on the polarizational state of light to separate inorganic from

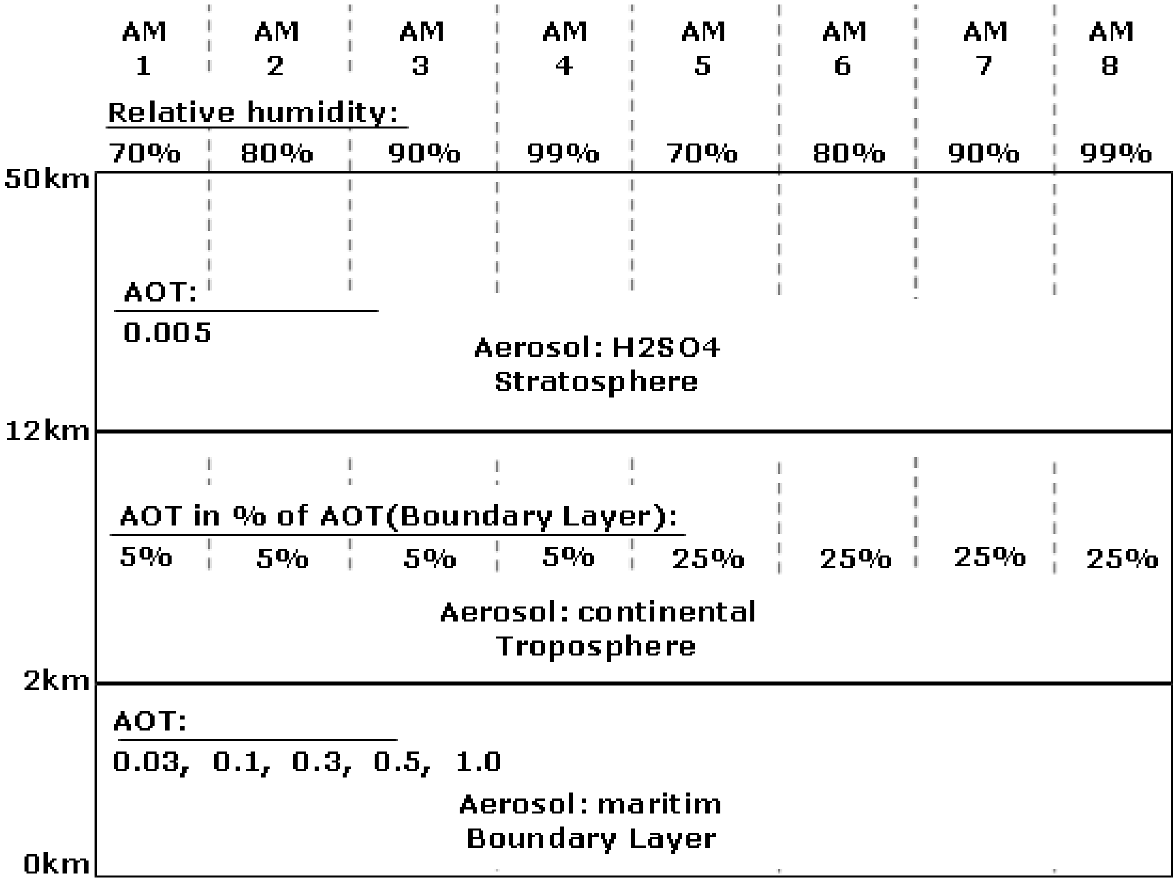

Figure 3.3: Schematic overview on the setup of the Aerosol Models (AM) as used in this study. The setup of the atmosphere model is taken from Schroeder et al. (2007a).

organic particles, which can be interesting, e.g., for the description of atmospheric aerosols, or for the remote sensing of scattering coccolithophore blooms as well.

Raman scattering: If incident energy is not conserved by the particle, inelastic scattering, i.e. trans-spectral scattering, occures as an internal source of radiation. In water, Raman scattering is the inelastic scattering of the water molecules. The molecule emits a photon of wavelength longer than the incident wavelength with a change in vibrational, rotational or electronic energy of the molecule. Raman scattering contributes to the in-water light field in clear open ocean waters in VIS spectral range up to 500 nm [Marshall and Smith (1990) , Bartlett et al. (1998)]. In this study the Raman effect is omitted from the MOMO model since optically complex, non-clear waters are studied (Fell and Fischer, 2001).

Fluorescence: Another inelastic process in water that transfers radiant energy from shorter to longer wavelengths is fluorescence. Fluorescence differs from Raman scattering because the

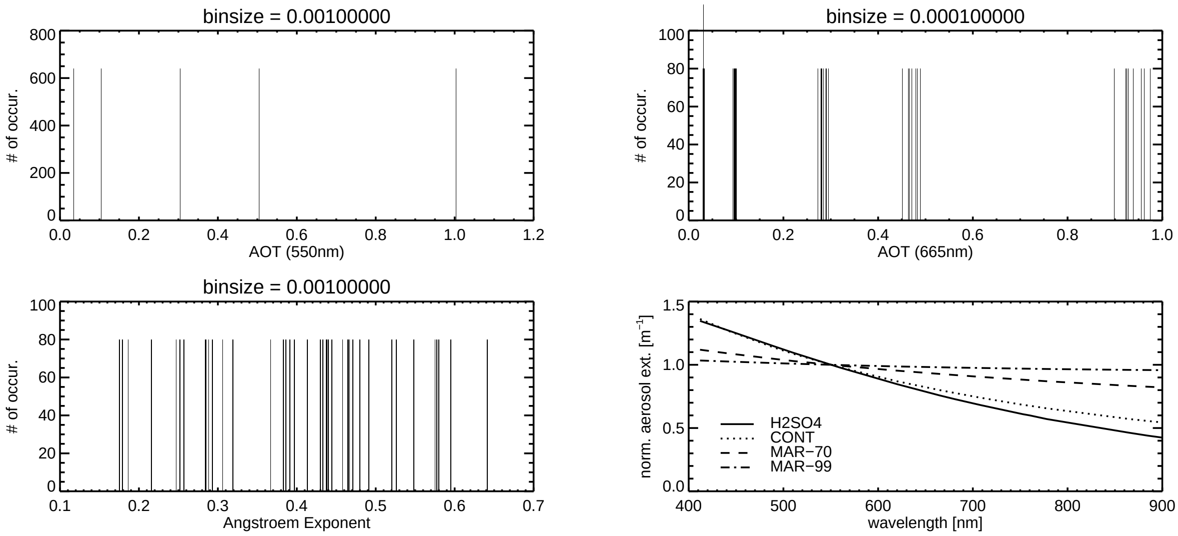

Figure 3.4: Examples of the distribution of aerosol model variables utilized within the atmosphere model to establish the synthetic dataset via RT calculations. Shown are the distribution of aerosol optical thickness (AOT) at 550nm (top left), the distribution of AOT at 665nm (top right), the Ångström Exponent (bottom left), and the spectral extinction coefficient c normalized at 550nm (bottom right).

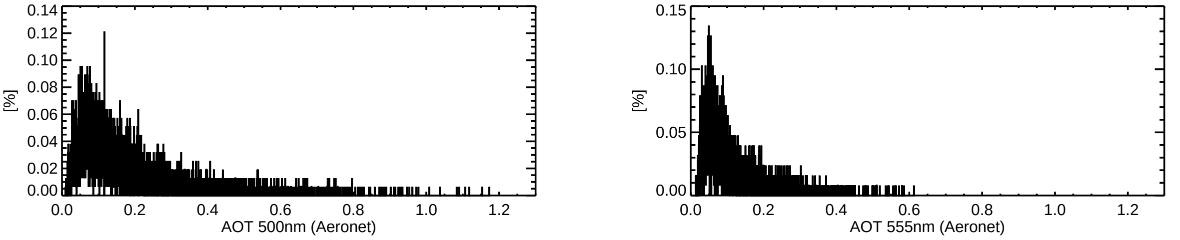

Figure 3.5: Measured AOT by the Aeronet system on Helgoland and Gotland (left) and on two stations in the Baltic Sea (right).

incident light is completely absorbed at a particular excitation wavelength. Contributions from fluorescence depend on [*Chla*] and YS. Sun-induced fluorescence can indicate [*Chla*] and algae photosynthetic activity [(Fischer and Kronfeld, 1990), (Fischer and Schüssel, 1990)]. The peak of sun-induced chlorophyll fluorescence is at 685 nm. Field studies showed fluorescence to be proportional to [*Chla*] in the range of $\leq$30 mg m^{-3} with a saturation effect for higher concentrations (Babin et al., 1996). Chlorophyll-*a* and YS fluorescence are neglected in the specific setup since fluorescence efficiencies for the phytoplankton species are unknown.

Adjacency effects: An area can be influenced by atmospheric scattering originating from an adjacent area. Also, near-shore, estuarine, and inland waters are influenced by the bright terrestrial vegetation, in particular in the nIR spectral range. In this study all oceanic areas less than 3 km away from land are excluded and are not handled in the retrieval.

Sea bottom effects: The sea bottom reflects light if the water body is shallow and clear. Absorption of pure water mainly limits the depth of penetration for wavelength longer than 650 nm, whereas absorption by phytoplankton pigments and CDOM limits penetration at wavelength shorter than 480 nm. Sun light can penetrate very clear oceans up to 200 m in the blue spectral range around 500 nm. Here, sea bottom effects are neglected by assuming a 500 m deep water column, thus no light reaches the bottom. Phytoplankton blooming regions can be assumed to be uninfluenced by bottom effects due to their off-shore location and their high optical density.

Sunglint: Sunglint is direct solar light reflected at the sea surface at the same angle as the observer zenith angle. The MERIS and MODIS sensors are not tilted away from the direction of reflection of sunlight at the air-sea interface, thus the data are significantly affected by sunglint contamination depending on the wind speed and the observation geometry. Sunglint is considered in the simulations.

Wind speed effects: Within MOMO, the sea surface slope distribution follows the statistical model of Cox and Munk (1954). The sea surface roughness is determind from two wind speeds of 1.5 and $7.2\,\mathrm{ms}^{-1}$. Wind speed dependent air bubbles, whitecaps, and foam can effect the optical properties of the sea surface. Whitecaps, which are breaking wave crests of buoyant bubble plums, impact climate by their high albedo and the production of marine aerosol (Frouin et al., 2001). Parameterization of whitecaps depends strongly on the wind speed, the air/water temperature difference, the sea state, and the region (Callaghan et al., 2008). Whitecaps are of sub-observation size for satellite remote sensing purposes. Moore et al. (2000) accounted a slight increase in surface reflectance with $R_W = 0.001$ to 0.002 in the 410 to 670 nm spectral range for wind speeds of 9 to $12\,\mathrm{ms}^{-1}$. Here, whitecap influence is neglected because of unknown full parameterization.

3.2 Inversion Algorithm

The previous section 3.1 described how a radiance measurement at TOA is influenced by the atmosphere/ocean system. The mathematical expression is formulated by the RTE. The inversion process is to derive the bio-geophysical parameters from the remote sensing measurements, which is not straightforward because the RTE is not invertible.

Algorithms to interpretate visible, multi-spectral remote sensing data of the oceans are often based on linear or logarithmic approximations of prior measured, empirical relationships. For example, the often used band ratio algorithms, which are ratios of particular sensor bands, are statistically linked to a certain target parameter. In optically complex waters with more than one varying component, the functional relationships between the measured radiant quantities and the derived target parameters are non-linear.

In this study, an inversion scheme called Artificial Neural Network (ANN) technique is applied, which accounts for the non-linear regression task. ANN applications are mathematical algorithms for non-linear statistical data modeling with the capability to learn complex relationships. ANN inversion approaches have been increasingly applied to oceanic remote sensing data, e.g., the ground segment processor of MERIS is based on ANN technology (Schiller and Doerffer, 2005). ANNs approximate the non-linear relationships by weight functions, which are then applied to the measured remote sensing data in the retrieval. The application of ANNs to the data is very fast. Another advantage of ANNs is the implied check, if the measured data is within the range of the data used for the algorithm development (Schiller and Doerffer, 1999).

Fundamentals on the theory of neural network techniques can be found, e.g., in Rojas (1993). Detailed information on the backpropagation algorithm applied in this study is also given in Fell (1997), Preusker (1999), Zhang et al. (2003), and Schroeder et al. (2007b).

3.2.1 Artificial Neural Network Architecture

A huge synthetic dataset of possible non-linear functional relationships between TOA radiances and remote-sensing reflectances as well as in-water constituent concentrations has been created with the RT forward simulations. For the ANN's learning process, i.e. the training of an ANN, the measured and target parameters are taken from this synthetic dataset.

The arificial neural network (ANN) algorithm used in this study has been developed by Preusker (2001). As illustrated in Fig. 3.6 it is a multilayer perceptrone (MLP) architecture consisting of three layers: an input layer, one hidden layer, and an output layer. Each layer consists of linear or non-linear computing elements, which are called neurons. The input layer of the ANN contains all measureable information as radiances and geometry. The output layer of the ANN contains the target quantities to be derived. The particular setups of the ANN layers are given in section 3.2.2. All neurons of the hidden layer are connected with every neuron in the input and output layers, whereas every connection is given a weight matrix W. The non-linear functional relationship is given through a non-linear activation function, which is here a sigmoidal function sig at each neuron of the hidden and output layer.

Within the ANN a back propagation method is used, which is a supervised learning technique that compares the results of the output layer to the truth of the synthetic training dataset. Within the learning procedure, the ANN traces errors and differences back to the initializing elements of the weight matrices in order to minimize the multi-dimensional error function Err of all weight matrices. Also, the trained ANN is presented to a second independent synthetic test dataset to verify the ANNs error.

Parameters affecting the performance of the trained MLP are the information content of the input data, the number of neurons in the hidden layer, and the level of noise added to the synthetic training data set.

3.2.2 Artificial Neural Network Training

From the oceans perspective on satellite remote sensing, the atmospheric portion of the TOA signal is unwanted and therefore has to be corrected. Within this study a 1-step inversion technique is choosen to derive in-water constituent concentrations directly from measured TOA radiances spectrums without an explicit prior atmospheric correction. In a 2-step process, first the bottom-of-atmosphere signal (BOA) is derived, which implies an explicit atmospheric correction. From the BOA spectrum the bio-geophysical parameters are retrieved. Schröder (2005)

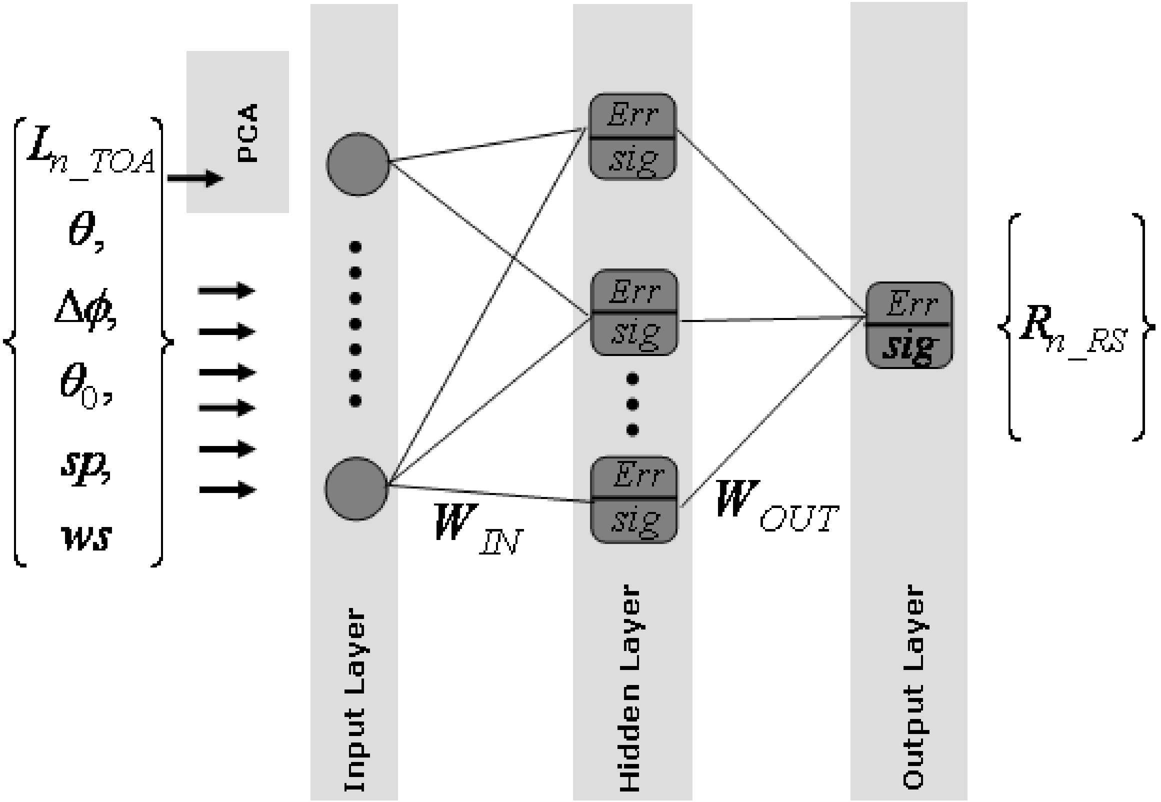

Figure 3.6: Example of the architecture of the Artificial Neural Network (ANN) build for the retrieval of remote sensing reflectance R_{RS}. *sig* stands for the non-linear activation sigmoidal function, *Err* is the multi-dimensional error function, which is minimized during the ANN training.

investigated in the performance of 1-step (direct) and 2-step (indirect) inversion schemes and showed a higher accuracy for 1-step retrieval methods for all constituent concentrations derived. Schroeder et al. (2007b) discuss, that the 2-step approach remains more sensitive to errors of the atmospheric correction.

Therefore, the input layer of the ANN is designed to receive the synthetic TOA radiance spectra, the geometry and the environmental information. The input layer of the ANN consisting of 18 neurons is written as:

$$\begin{aligned} v_{ANN-Input-Layer} = \{ & L_{TOA}(412.5, 442.5, 490, 510, 560, 620, 665, 709.5, \\ & 753.5, 778.5, 865, 885\, nm), \\ & \sin(\theta)\cos(\Delta\phi), \sin(\theta)\sin(\Delta\phi), \cos(\theta), \cos(\theta_0), \\ & windspeed(ws), surfacepressure(sp)\}. \end{aligned} \tag{3.11}$$

The ANN for the retrieval of eight remote-sensing reflectances R_{RS} to be derived at the MERIS wavelengths in the visible spectral range, contains eight neurons in the output layer.

$$v_{ANN-Output-Layer\,1} = \{R_{RS}(412.5, 442.5, 490, 510, 560, 620, 665, 709.5\, nm)\} \tag{3.12}$$

For each bio-geophysical target parameter one ANN ist trained for the purpose of choosing the best ANN independently. The ANNs for the in-water constituent concentrations receive one neuron in the output layer.

$$v_{ANN-Output-Layer\,2} = \{[\log(Ph)]\} \tag{3.13}$$

$$v_{ANN-Output-Layer\,3} = \{[\log(NAP)]\} \tag{3.14}$$

$$v_{ANN-Output-Layer\,4} = \{[\log(YS)]\} \tag{3.15}$$

To choose an appropriate number of neurons in the hidden layer no universal rule exists. Based on setups from Schiller and Doerffer (2005) and Schröder (2005), ANNs of 60, 80, 100, and 120 neurons in the hidden layer are trained for all the target parameters. From these ANNs the 'best' performing ANN was choosen as described in section 3.2.2.

The synthetic dataset

From all possible IOP combinations, 20 equally distributed triplets are randomly selected and used as input for the RT calculations. As introduced in section 3.1.3, the atmosphere model contains 160 different atmospherical and environmental states depending on the wavelength. For each atmospherical state and for each wavelength a triple of the bio-geophysical parameters Ph, NAP, and YS are choosen from the bio-optical water model. The bio-optical models with the concentration ranges for the cyanobacterial bloom in the Baltic Sea and the coccolithophore bloom are defined in chapters 4 and 5. One bio-geophysical parameter triple gives 1920 different combinations depending on wavelength as input for the RT model.

The RT simulations are performed for 17 solar and observation zenith angles θ, and 25 azimuth differences $\Delta\phi$ (see section 3.1.3). The complete synthetic dataset contains for each of the 12 wavelengths $160 \times 20 \times 17 \times 25$ possible non-linear relationships between synthetic $L_{TOA}(\lambda)$ values and the geophysical parameters $R_{RS}(\lambda)$, Ph, NAP, and YS.

From the complete synthetic dataset, two independet subsets, i.e. the training dataset and the test dataset, are independently and randomly selected. Each dataset contains 100.000 functional relationships for sunglint corrected L_{TOA} and 100.000 functional relationships for sunglint influenced L_{TOA}. The training dataset contains 200.000 relationships to *train* the ANN, the test dataset contains 200.000 functional relationships to *test* the ANN within the learning procedure. The subset size of 200.000 functional relationships showed to lowest relative error in the variance compared to the full synthetic dataset as shown in Fig. 3.7.

Before the subset datasets are presented to the ANN, the synthetic data are modified. The in-water constituent concentrations are log-transformed prior presenting it to the ANN to decrease the orders of magnitude and to cover design issues in the backpropagation ANN. Principle component analysis is performed of the synthetic L_{TOA} spectra to permit spectral decorrelation of the correlated input spectrum. Gaussian distributed noise as given in Tab. 3.2 is added to the synthetic training data to create an ANN, which is robust with respect to noisy input. The noise for the synthetic L_{TOA} corresponds to the radiometric sensitivity of the MERIS sensor.

Table 3.2: Gaussian distributed noise added to training dataset.

$v_{ANN-INPUT}$	Noise [%]
L_{TOA} (412.5,442.5,490,510,560,620,665 709.5,753.5,778.5,865,885nm)	0.2
L_{TOA}(*sun glint corrected*) (412.5,442.5,490,510,560,620,665 709.5,753.5,778.5,865,885nm)	0.2
$[\log(Ph)]$	0.001
$[\log(NAP)]$	0.001
$[\log(YS)]$	0.001
wind speed (ws)	2
surface pressure (sp)	2
$\sin(\theta)\cos(\Delta\phi)$	0.001
$\sin(\theta)\sin(\Delta\phi)$	0.001
$\cos(\theta)$	0.001
$\cos(\theta_0)$	0.001

Performance of the ANN

The performance of the ANN training is evaluated by applying it to an unseen test dataset, independently taken from the synthetic dataset. To determine the 'best' ANN, two error measures are compared: the root mean square error $RMSE$, which is a measure of the variation of the derived quantity, and the $BIAS$, or mean deviation, which are defined as:

$$RMSE = \sqrt{\frac{\sum(x_{Train} - x_{Test})^2}{n}} \tag{3.16}$$

$$BIAS = \frac{\sum(x_{Train} - x_{Test})}{n}. \tag{3.17}$$

To illustrate the size of the subset dataset, i.e. the size of the test and training dataset, compared to the complete synthetic data, the variance of the complete and subset dataset is calculated. For L_{TOA} of MERIS band one at 412.5 nm, Fig. 3.7 exemplarily shows the relative error RE of the variance σ^2 between the complete, synthetic dataset and a growing number of samples for the subset dataset. The relative error RE is calculated as:

$$RE = \frac{\sigma^2_{subset} - \sigma^2_{complete}}{\sigma^2_{complete}} 100\%. \tag{3.18}$$

σ^2 is the variance:

$$\sigma^2 = \frac{\sum(L_{TOA} - \overline{L}_{TOA})^2}{N-1}. \tag{3.19}$$

The standard deviation σ is the positive square root of the variance:

$$\sigma = \sqrt{\frac{\sum(L_{TOA} - \overline{L}_{TOA})^2}{N-1}}. \tag{3.20}$$

For a subset dataset containing 100.000 functional relationships the relative error RE of the standard deviation σ is 0.2% at a confidence level of 99.9%, for 200.000 functional relationships the RE is 0.015%. The right panel of Fig. 3.7 shows the histogram distribution of the full (black curve) and the subset dataset (blue curve) for L_{TOA} of the first MERIS spectral band at 412 nm.

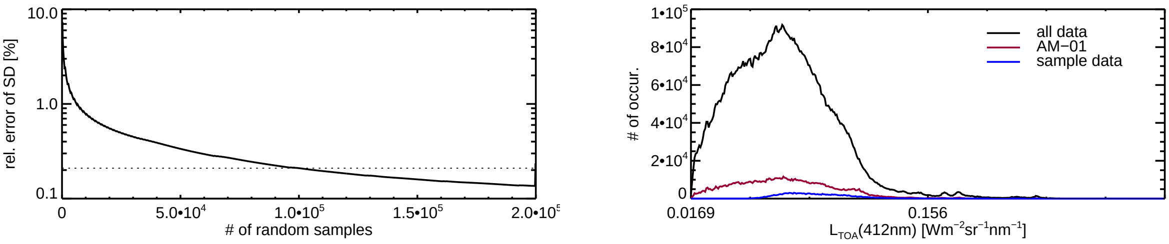

Figure 3.7: (left:) Relative error of standard distribution for L_{TOA}(412.5nm) depending on the size of the subset dataset. (right:) Histogram distribution of full (black line) and subset (red line) synthetic data set for L_{TOA}(412.5nm).

3.2.3 Discussion of the Inverse Problem

In the following, problems are discussed concerning the inversion process for visible, multi-spectral remote sensing of the oceans. Difficulties are caused by (1) the non-linear functional relationships and the applied inversion technique, (2) the ambiguity of the high number of varying bio-optical properties, and (3) the strong atmospheric influence on the measured TOA signal with only minor fraction contributing from the ocean.

(1) The functional relationship between measurements and target parameters, as described by the RTE (section 2.1.5), is non-linear and complex, which does not allow an analytic inversion. The non-linearity problem can be solved applying a functional assumption or using statistical empirical regression techniques. An ANN is one possible method to be applied. An ANN is a semi-analytical algorithm approximating the functional relationship. Hence, the approximation introduces an error. Intercomparisons published in Lee (2006) examine the variability and errors of different inversion methods. The tested ANNs therein show an overall very good performance compared to other methods. The adavantage of ANNs is also the fast application of their output weight matrices to satellite data, compared to look-up-tables.

(2) A second source of errors are ambiguous IOPs due to their addititive nature (see also section 2.1.4). Identical sums of total absorption coefficients a_{total} and total scattering coefficients b_{total} can result from different specific IOPs. Furthermore, different total IOPs can result in identical single-scattering albedos ω_o (see 2.12) or total extinction coefficients c_{total} used within the RTE (see 2.19) and the RT model. Thus, the solution of the inversion can not be unique. Defoin-Platel and Chami (2007) discuss in detail this non-uniqueness problem and the mathematically non-bijection constraints. An ANN based inversion technique is choosen as it allows the use of information on multi-spectral scale.

For the atmospheric and oceanic models a restricted number of variables are choosen. Here, the vector containing the oceanic input is composed of seven varying bulk optical properties, which are co-varying with three bio-geophysical parameters.

$$\begin{aligned} v_{IOP}(\lambda) \;&=\; \{c_{Ph}(\lambda), \omega_{oPh}(\lambda), p_{Ph}(\Psi), \\ &\qquad a_{YS}(\lambda), c_{NAP}(\lambda), \omega_{oNAP}(\lambda), p_{NAP}(\Psi)\}. \end{aligned} \tag{3.21}$$

A vector containing all varying atmospheric conditions, applied in this study, can be written as:

$$v_{ATM}(\lambda) \;=\; \{8\, Aerosol\, Models(\lambda), 5\, AOTs(\lambda)\}. \tag{3.22}$$

Varying geometric conditions and all environmental conditions, which are measured data are composed in following vector:

$$v_{GEO} \;=\; \{\theta_0, \theta, \Delta\phi, wind\, speed, surface\, pressure, relative\, humidity\}. \tag{3.23}$$

The parameters of v_{GEO} are known for MERIS Level-1b measurements. v_{ATM} and v_{IOP} are the varying, independent atmospheric and oceanic variables, that have to be derived from the measured TOA signal. Restricting assumption for the atmosphere are described in section 3.1.3. For the bio-optical ocean model the number of variables is restricted to varying Ph, NAP, and YS triples, which means that all IOPs stated in v_{IOP} are parameterized specifically for the considered phytoplankton bloom and region in terms of Ph, NAP, and YS.
(3) As discussed in the beginning of section 3.1.3 in average only about 13% of the measured intensity at TOA is from the ocean, the major fraction originates from the atmosphere. Therefore, the TOA signal differences to be interpreted are very small, which limits the retrieval accuracy in general.

3.3 The Retrieval Process

Before applying the trained ANNs to observational data, i.e. MERIS Level-1b data, three further processing steps have to be completed.
(1) MOMO simulations are performed for spectral solar irradiance $E_0 = 1$. Therefore, spectral TOA radiances measured by the MERIS sensor (L_{TOA}^{MERIS}) are normalized to measured bandpass weighted mean solar irradiance (E_0^{MERIS}) provided within the Level-1b dataset.

$$R_{normTOA}^{MERIS}(\lambda) \;=\; \frac{L_{TOA}^{MERIS}(\lambda)}{E_0^{MERIS}(\lambda)} \tag{3.24}$$

(2) Within MOMO, stratospheric ozone absorption is treated as broadband continuum absorption decreasing the spectral solar irradiance and the upwelling radiance field at TOA in the spectral range of the Chappuis band from 450 to 750 nm. For the simulations a constant depth integrated ozone loading of 344 DU is considered. MERIS auxillary Level-1b data files contain measured ozone transmission. Therefore, a correction coefficient is applied to the measured MERIS TOA radiances L_{TOA} before retrieving the geophysical and the bio-geophysical parameters.
(3) Within MOMO, radiance fields are calculated for azimuthal differences $\Delta\phi$ between the

observation angle and the solar angle. The retrieval processes is performed independently for each MERIS pixel. To avoid discontinuity of the nadir-viewing MERIS pixel caused by a change of azimuthal difference $\Delta\phi$ from 0° to 180°, MERIS geometry, given in radian coordinates, is transformed to the cartesian coordinate system.

Finally, the weight matrices W of the trained and selected ANNs are applied to each oceanic MERIS Level-1b observation in 12 spectral bands. sig is the sigmoidal activation function.

$$v_{geophysical\,parameter} = sig(W_{out} \,\#\, sig(W_{in} \,\#\, v_{ANN-Input})) \tag{3.25}$$

Within this step, the standard MERIS Level-1b land-ocean mask and a cloud mask developed by Preusker et al. (2005) to exclude all non-oceanic and cloudy pixels are applied. Then, the specific masks developed in this work are applied to all ocean pixels as decribed in chapters 4 and 5.

3.4 Characteristics of Envisat MERIS Data

To give a short introduction to the satellite data for which the algorithms are developed, the Medium Resolution Imaging Spectrometer MERIS onboard the Envisat satellite is described.

Envisat is a multi-disciplinary Earth observation satellite launched by the European Space Agency (ESA) on February 28th 2002. Envisat is a sun-synchronous polar orbiting platform with a nominal altitude of 799.8 km. The descending node equator crossing time is 10:00 a.m. Extensive information on Envisat as well as on the Medium Resolution Imaging Spectrometer MERIS can be found, e.g., in Rast et al. (1999) or Bézy et al. (2000).

MERIS is an imaging spectrometer with medium spatial and high spectral and radiometric resolution. MERIS data is available at 1.1 km^2 reduced resolution (RR), which are used in this study, and 0.3 km^2 full resolution (FR). The instrument consists of five identical optical sensors, each consisting of two-dimensional Charge Coupled Device (CCD) arrays, with a swath width all together of 1165 km and a cross-track field of view of 68.5 °. The Instantaneous Field of View (IFOV) for each MERIS pixel is 0.019 °.

MERIS simultaneously aquires observations in 15 spectral bands from 412.5 nm to 900 nm. The band setting is shown in Fig. 3.2 in comparison to MODIS and SeaWiFS spectral bands. The nominal bandwidth of each band is 10 nm except channels 8 and 10, which have a bandwidth of 7.5 nm, while the oxygen absorption band 11 has a bandwidth of 2.5 nm. From Fig. 3.2 it can be seen that spectral bands around 620 nm (band 6) and 709 nm (band 9) are only available on MERIS, and not on the MODIS or SeaWIFS sensors.

Compared to other visible multi-spectral sensors, MERIS has an increased radiometric accuracy and sensitivity. Radiometric sensitivity is 2.1^{-4} for the noise equivalent spectral reflectance at sea level $NE\Delta R$. Radiometric resolution is 3.0^{-5} Wm^{-2}sr^{-1}nm^{-1}.

Geolocated and calibrated top-of-atmosphere (TOA) radiances L_{TOA} and additional annotation data sets describing the quality of the measurements are stored in Level-1b data. Level-1b data also contain auxiliary information on surface wind speed, relative humidity at 850 hPa, and the total ozone column content acquired from the European Centre for Medium-Range Weather Forecasts (ECMWF) analysis data. Standard bio-geophysical parameters, i.e. the atmospheric,

land, and oceanic products, are stored in Level-2 data.
The data used here, are provided through MERIS Catalogue and Inventory (MERCI) system for validation purposes http://merci-srv.eo.esa.int/merci/welcome.do.

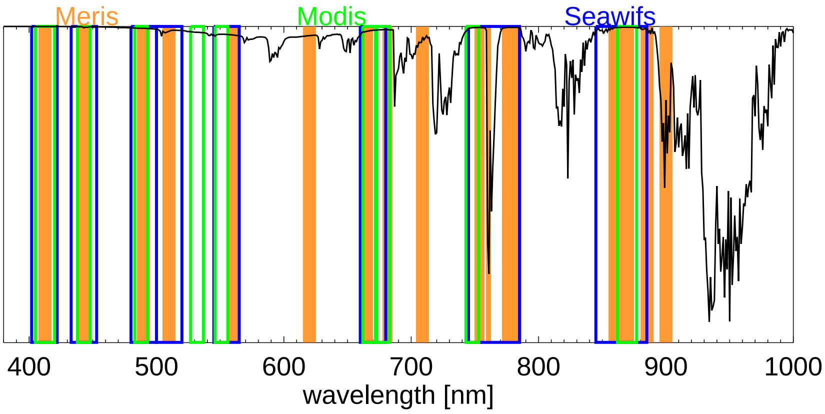

Figure 3.8: MERIS (orange, filled), MODIS (green) and SeaWiFS (blue) spectral bands. Nadir continuum transmission spectrum is given for a standard tropospheric atmosphere (black line). MERIS spectral band numbers are enumerated from 1 (412.5 nm) to 15 (900 nm).

Chapter 4

Algorithm for the Baltic Sea and the Detection of *Cyanophycaea* Phytoplankton Blooms

4.1 Background

4.1.1 The Baltic Sea Basin

The Baltic Sea Basin is a semi-enclosed sea, which sometimes is regarded as an extended fjord of the Atlantic Ocean or as a large estuary with low tides (Voipio, 1981). Caused by the morphometry, the water exchange with the North Sea is limited, with sporadic entering high saline and oxygen enriched surface waters. Together with the high freshwater input from rivers in the Northern and Southern Baltic, it results in the brackish nature of the Baltic Sea. The Baltic Proper has a permanent vertical haline stratification, with a brackish surface layer and a heavier saline bottom layer. The high fluvial input from the north and the saline enrichment from the south west cause a horizontal surface salinity gradient across the basin. The surface salinity decreases from 6 to 8 in the Gotland Sea, to 5 to 6 in the Bothnian Sea, down to 2 to 3 in the Bothnian Bay. Compared to other seas, salinity in the Baltic Sea is low.

Temperature variations of the surface waters are strongly linked with the seasonal cycle. Based on NOAA-AVHRR data, Siegel et al. (2006) showed an increase in summer temperatures during the 1990ies and first years of 2000s.

Eutrophication is the main environmental problem in the Baltic Sea, caused by an increased nutrient input from land and atmosphere as well as by the summer blooms of nitrogen-fixing cyanobacteria. Further, the increased primary production during spring blooms causes an increased organic matter enrichment on the basins' bottom, which leads to higher degradation rates of the organic matter and an anoxia in bottom waters. Based on *in-situ* measurements, Olsonen (2008) reports an increase of chlorophyll-a concentration of over 150% in the Northern Baltic Proper and the Gulf of Finland from the 1970s until the early 2000s. Chorophyll-a concentration in the Bothnian Sea increased more than 180% from the late 1970s until the late 1990s, and decreased thereafter. Diaz and Rosenberg (2008) called the Baltic Sea, the largest antrophogenic dead zone in the world. More detailed information can be found in Barale and Gade (2008) or in the book of the The BACC Author Team (2008).

4.1.2 Optical Characterization of the Baltic Marine Ecosystem

As salinity decreases from south to north, yellow substance (YS) absorption shows a south-north increase due to high river discharge in the Northern Baltic. The high YS contribution induces high absorption in the blue spectral region. Babin et al. (2003) report a contribution of 48% by YS to total absorption neglecting pure seawater absorption (see Tab. 4.1). High CDOM absorption leads to a relatively small signal emerging from sea, which makes the water dark compared to other coastal seas.

The high variability in non-algal particle (NAP) load causes a large variability in remote-sensing reflectance (Darecki et al., 2003). Babin et al. (2003) measured very high proportions of organic matter and a low mineral content. They report organic NAP with 87% and inorganic NAP with 13%. Kratzer and Tett (2009) show that the contribution of inorganic particulate matter decreases with the distance from the coastline.

The open Baltic Sea is dominated by phytoplankton development with a typical YS absorption background value of $0.2\,\mathrm{m}^{-1}$. Most exceptional compared to other marine ecosystems are the very dense phytoplankton blooms of *cyanophycaea* occuring in summer. They cause major environmental concern due to their increased nitrogen input and their potential toxicity. Cyanobacteria contain low to high concentrations of the accessory photosynthetic phycobilin pigments phycocyanin and phycoerythrin, which are responsible for distinct absorption features. The cyanobacteria cells can also cause high reflection near 650 nm. If cyanobacteria are dominating the phytoplankton biomass, the water body also shows high reflectance in the nIR spectral range above 670 nm. If, additionally, the phytoplankton bloom is present in surface waters, the dominance of pure water absorption on the water-leaving singnal is reduced or even compensated by phytoplankton reflectance (Ruiz-Verdú et al., 2008).

Table 4.1: Relative contributions of in-water constituent concentrations and IOPs to, taken from Babin et al. (2003).

Proportion	Unit/(Wavelength)	AV	SD
NAP:$[Chla]$	$\mathrm{g\,mg^{-1}}$	0.67	0.19
YS :$[Chla]$	$\mathrm{m^2mg^{-1}}$	1.58	0.49
YS :NAP	$\mathrm{m^2mg^{-1}}$	2.41	0.58
a_{Ph}:$(a_{total} - a_W)$	(443nm)	0.32±0.07	
a_{NAP}:$(a_{total} - a_W)$	(443nm)	0.2±0.05	
a_{YS}:$(a_{total} - a_W)$	(443nm)	0.48±0.07	

4.1.3 Phytoplankton Blooms of *Cyanophycaea* in the Baltic Sea

Cyanobacteria are photosynthetic active bacteria, which are counted as picophytoplankton with a cell size smaller than 2 μm. In the phytoplankton functional type (PFT) classification, cyanobacteria are pico-autotrophs and nitrogen-fixers.

Phytoplankton succession in the Baltic Sea shows a similar pattern every year. During spring warming the water becomes stratified and the phytoplankton remains in the sunlight exposed euphotic zone, which starts the spring blooming. The spring bloom in the Baltic occurs usually in the second half of April and is dominated by a mixture of diatoms and dinoflagellates. It follows a stagnation period in late spring to early summer (June). Fig. 4.1 illustrates the strong spring blooming with highest chlorophyll-a concentrations $[Chla]$ in April.

In July and August, thick surface accumulations of cyanobacteria can occur under warm, wind calm conditions and high solar radiation (Kahru, 1997). Wind-induced mixing and cloudy conditions can interrupt or terminate the bloom.

The summer bloom is dominated by nitrogen-fixing cyanobacteria of the species *Nodularia spumigena* and *Aphanizomenon flos-aquae. Nodularia sp.* is producing toxins, *Aphanizomenon flos-aquae* is non-toxic. The cyanobacteria use dissolved molecular nitrogen (N_2) as their nutrient source, which favors cyanobacteria to other phytoplankton species. The cyanobacteria can contain gas vacuoles enabling them to adjust their position in the water column. They float near the surface during the day for photosynthesis and sink at night to harvest nutrients. As shown in Fig. 4.1, monthly averaged maximum values and daily values of $[Chla]$ are lower for the summer months than for the spring months. This can be explained by an undersampling of cyanobacteria biomass by *in-situ* methods through their floating in the water column and by the fact that *cyanophycaea* contain lower $[Chla]$ compared its accessory pigment concentration. Further on, *in-situ* sampling is complicated in bloom regions and specific *in-situ* methods have to be used. Ships often destroy the spatial distribution of the blooms while sampling. Also, water-sampling does not depict the spatial patchiness of bloom structures (Kutser, 2004). On the example of the Baltic Sea, Rantajärvi et al. (1998) showed the non-adequateness of water-sampling from ferry boats to report phytoplankton changes during bloom conditions.

Usually, blooms of the algae class *cyanophycaea* are common in eutrophic freshwater bodies (Simis et al., 2005b). Nevertheless, blooms of cyanobacteria are native to the marine Baltic Sea due to its very low seasalt content (Bianchi et al., 2000). The impact of the mass occurences of cyanobacterial blooms on the Baltic is subject of various scientific studies [e.g., Kahru et al. (1994), Karjalainen et al. (2007)]. Continuous monitoring and the evaluation of long-time trends and ecosystem feedbacks of total phytoplankton biomass and cyanobacterial biomass are requested, e.g., from the intergovernmental Helsinki Commission (HELCOM) for the protection of the marine Baltic Sea environment.

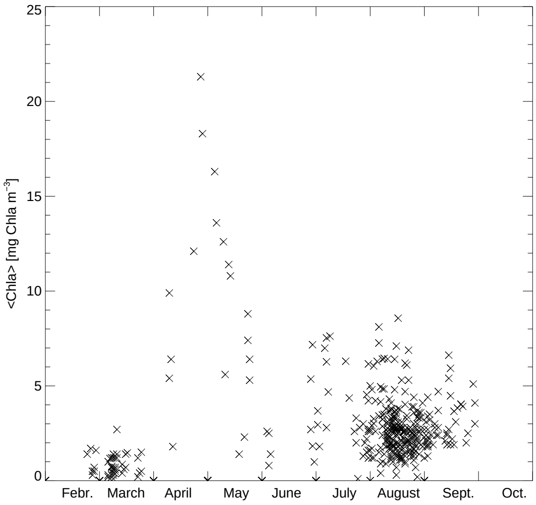

Figure 4.1: Daily surface concentrations of [*Chla*] in the Baltic Sea for the years 1979 to 2005. Data collected and owned by FIMR (Olsonen, 2008).

4.1.4 Algorithms for the Baltic Sea and for the Detection of *Cyanophycaea*

A number of experimental, empirical and semi-analytical algorithms adapted for specific Baltic Sea conditions do exist. For operational purposes Darecki et al. (2005) and Vepsäläinen et al. (2005) provide chlorophyll-a retrieval algorithms for SeaWiFS satellite data. For MODIS and MERIS data, standard operational algorithms are available, but no regional Baltic Sea algorithm (Ohde et al., 2007). The standard algorithms do not account for Baltic Sea typical high YS absorption, dense phytoplankton bloom conditions, and cyanobacteria dominated waters. This results in errors when applying the standard algorithms. Reinart and Kutser (2006) report highly variable results and insufficient accuracy for chlorophyll-a concentrations derived from SeaWiFS, MODIS, and MERIS data applying standard algorithms during blooming conditions. Specific algorithms for remote sensing of cyanobacterial biomass have been developed for freshwater lakes. A comprehensive overview on the existing algorithms for cyanobacteria biomass remote sensing in inland waters is given by Ruiz-Verdú et al. (2008).

Tab. 4.2 lists the three existing methods for the recognition of phytoplankton blooms dominated by cyanobacteria in the Baltic Sea. Two algorithms are based on supervised classification techniques but do not account for the specific optical properties of the Baltic Sea. Kutser et al. (2006) performes a case study based on a bio-optical water model accounting for *cyanophycaea.*

Table 4.2: Algorithms for cyanophycaea bloom recognition in the Baltic Sea. Ref.[1]: Hansson and Hkansson (2007), Ref.[2]: Kutser et al. (2006), Ref.[3]: *http : //www.environment.fi*

Satellite Data	Parameter	Unit	Period	Method	Ref.
NOAA-AVHRR	duration, extent, intensity	[days], [km^2], [km^{2}day^{-1}]	1997-2006	supervised classification	[1]
Landsat,MODIS, MERIS	$[Chla]$	[mg m^{-3}]	case studies	bio-optical modeling	[2]
MERIS	likelihood of surface algae	4-level likelyhood	2003-ongoing	supervised classification	[3]

4.2 Bio-optical Model for the Baltic Sea and the Sensitivity

In the following, the parameterization of the bio-optical water model for the Baltic Sea is defined. In this section, the bulk spectral IOPs are described and the concentration ranges are determined. The varying IOPs are discussed in the following. All IOPs used witin the bio-optical model for the Baltic Sea algorithm and within the sensitivity studies of this section are tabulated in Tab. 4.6 on page 49.

Objective is the full assessment of the macroscopic optical properties extinction coefficient c, single-scattering albedo ω_o, and phase function p. The vector of all varying IOPs for the Baltic Sea is written as:

$$\begin{aligned} v_{IOP-BALTIC}(\lambda) &= \{c_{Ph}([TChl],\lambda), \omega_{oPh}([TChl],\lambda), p_{Ph}(\Psi), \\ &\quad a_{YS}(a_{YS}(443),\lambda) \\ &\quad c_{NAP}([TSM],\lambda), \omega_{oNAP}([TSM],\lambda), p_{NAP}(\Psi)\}. \end{aligned} \tag{4.1}$$

4.2.1 Parameterization of Absorption

Phytoplankton Absorption a_{Ph}: Bricaud et al. (1995) showed with their paper, that $a_{Ph} \neq [Chla]$: the relationship between the bulk absorption coefficient a_{Ph} and the concentration $[Chla]$ is non-linear and can be parameterized by a two-parameter power model given in Eq. (3.4). Bricaud et al. (1995) and Bricaud et al. (1998) established a parameterization, which allows the estimation of phytoplankton absorption from the concentration accounting for the non-linear increase of the specific absorption with concentration. The relationship is defined for $[Chla]$ over three orders of magnitude from 0.02 to 25 mg m^{-3}. Staehr et al. (2004) re-investigated this parameterization for estuarine, coastal, and oceanic waters with mixed phytoplankton for the Skagerrak and and Kattegat region of the North Sea. The Staehr model is parameterized for $[Chla]$ up to 100 mg m^{-3}.

For medium range $[Chla]$ in the Baltic Sea of 1 to 5 mg m^{-3}, the parameterization by Staehr results in a gain in absorption of about a quarter around 442 nm compared to the Bricaud model. Illustrated in Fig. 4.2 the specific chlorophyll-a absorption coefficient a^*_{Chla} is shown to decrease for increasing $[Chla]$. It is a coupled result of (1) nutrient enrichment leading to an increased dominance of larger phytoplankton with high intracellular pigment concentration rather than increased cell number density, (2) pigment packaging, which is the effect of increased packaging and shading of the light absorbing pigments, and (3) a change in pigment composition.

In Fig. 4.2 the pre-dominant features of chlorophyll-a with a first absorption maximum around 440 nm and a second maximum around 670 nm are visible.

Phytoplankton blooms can reach very high phytoplankton concentration, especially in the Baltic Sea. Here, the spectral bulk absorption coefficients for mixed phytoplankton in the Baltic Sea is modeled as described in Eq. (3.4) with tabulated coefficients A_{aPh} and B_{aPh} from Bricaud et al. (1998).

Measurements of absorption for cyanobacterial biomass in the Baltic Sea including a quantification of the auxilliary phaeopigments are very rarely. Unpublished measurements from S. Kratzer and N. Stroembeck are shown in Fig. 4.3. The measured data from Stroembeck are laboratory *in-situ* measurements of grown cultures at concentrations higher than 100 mg m^{-3}. The measurements from S. Kratzer have been collected from Baltic Sea waters in 1998. Fig. 4.3 illustrates the measured a^*_{TChl} spectra and shows nicely the additional pigment absorption features around 560/580 nm from phycoerythrin and a slight increase in absorption around 620 nm caused by the phycocyanin pigment. $[TChl]$ is the sum of chlorophyll-a and additional pigments like phycocyanin.

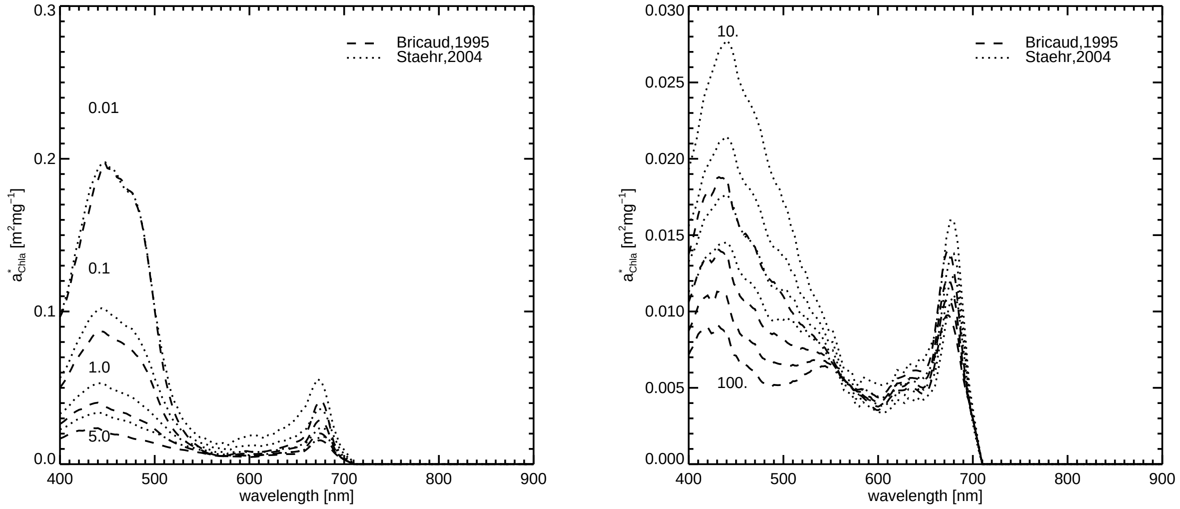

Figure 4.2: Varying specific chlorophyll-a absorption for mixed phytoplankton for (left) $[Chla]$ from 0.01 to 5 mg m^{-3} and (right) from 10 to 100 mg m^{-3}. Shown are parameterization from Bricaud et al. (1998) and Staehr et al. (2004). Pre-dominant features are chlorophyll-a absorption maxima around 440 nm and around 670 nm.

The a_{Ph}-model for cyanobacterias is derived in this work. The regression scheme is a two-parameter power model as introduced by Bricaud et al. (1995) and given in Eq. (3.4). Measurement data included in the parameterization is for cyanobacteria dominated phytoplankton only. Fig. 4.4 shows the distribution of the *in-situ* data and the calculated a^*_{Chla} values. When more *in-situ* measurements become available in future, a modification of the parameterization is expected as there is a large concentration gap between the water samples and the laboratory cultures. The overall tendency of the parameterization is taken as a good estimation as the A_{aPh} and B_{aPh} coefficients are in the range of the Bricaud and Staehr models which is shown in Fig. 4.5. The A_{aPh} values for cyanobacteria are slightly higher than the values for mixed phytoplankton, which can be explained by the weakly packaging effect of the cyanobacterias due to their smaller cell size. The spectral B_{aPh} values for cyanobacteria are less varying than the compared values, which is an effect of the additional absorption of the pigments phycoerythrin around 580 nm and phycocyanin around 620 nm.

Fig. 4.7 illustrates the sensitivity of the spectral remote sensing reflectances (left) and TOA radiances (right) for varying $[Chla]$ concentrations depending on the chosen a_{Ph}-model. The sensitivity study setup is tabulated in Tab. 4.3. The reference a_{Ph}-model is from Staehr et al. (2004). Shown are the differences of mono-specific cyanobacteria absorption model to the mixed phytoplankton model of Staehr. The differences are positive, which indicates a reduction of radiances, for all MERIS spectral band except band 6 at 620 nm. Due to the higher absorption of the picophytoplankton cyanobacteria reflectance and radiance decrease. At 620 nm the cyanobacteria dominated phytoplankton community increases reflectance. The model parameters choosen for the illustration are summarized in Tab. 4.3.

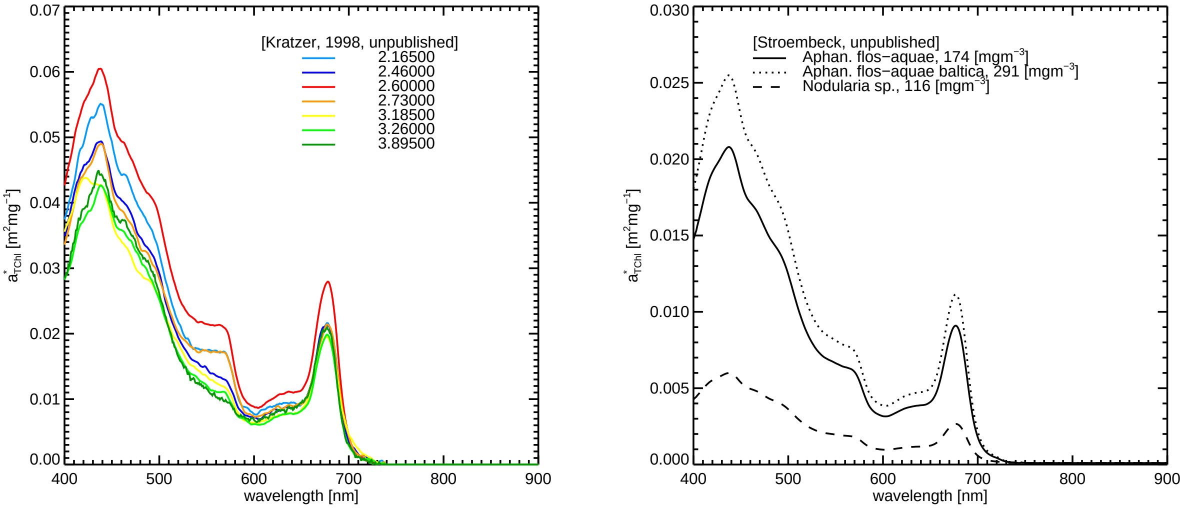

Figure 4.3: Absorption coefficients for a_{Ph} parameterized in $[Chla]$. The additional pigment absorption of phycoerythrin around 580 nm and phycocyanin around 620 nm can be seen compared to only a^*_{Chla} shown in Fig. 4.2. Data collected and owned by Drs. S. Kratzer and N. Stroembeck, respectively.

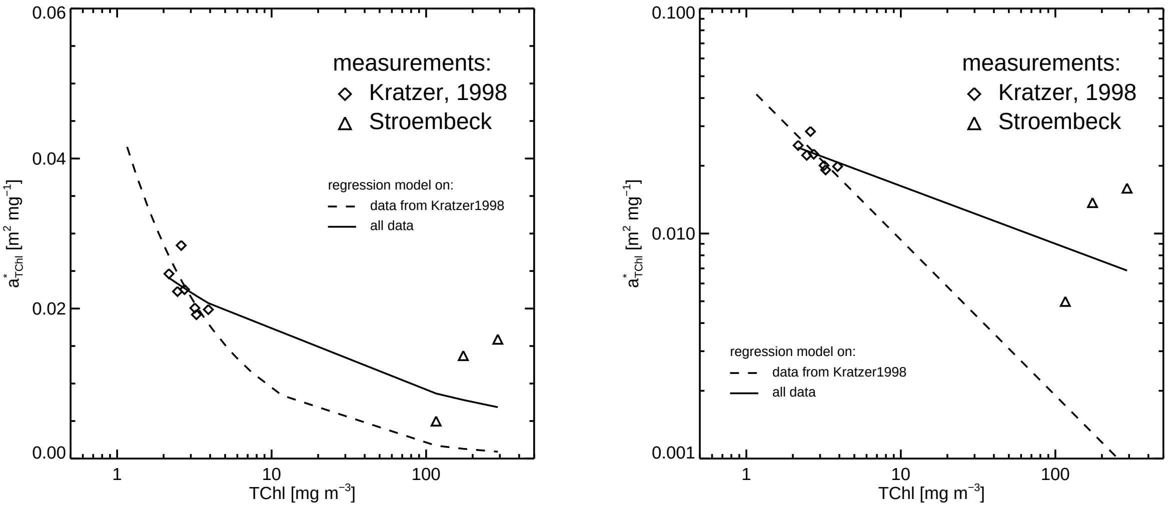

Figure 4.4: Regression for a_{Ph} in $[Chla]$ on log-transformed scale (left) and on log-log transformed scale (right). The regression model is a two-parameter power model in the form of $a^*(\lambda) = A_{aPh}(\lambda)[Chla]^{-B_{aPh}}$. Shown are two fits: including and excluding high $[Chla]$. Data collected and owned by Drs. S. Kratzer and N. Stroembeck, respectively.

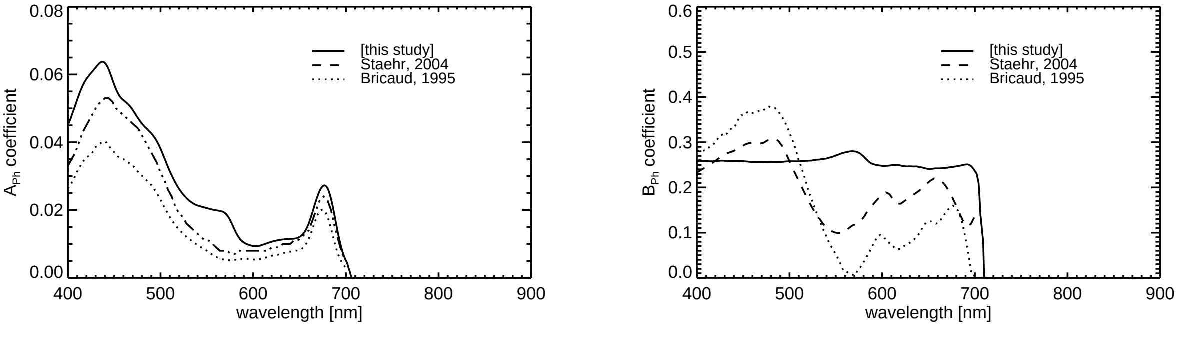

Figure 4.5: Comparison of the phytoplankton absorption power model parameters for Bricaud et al. (1995) and Staehr et al. (2004) compared to A_{aPh} and B_{aPh} derived in this work from S. Kratzer and N. Stroembeck data.

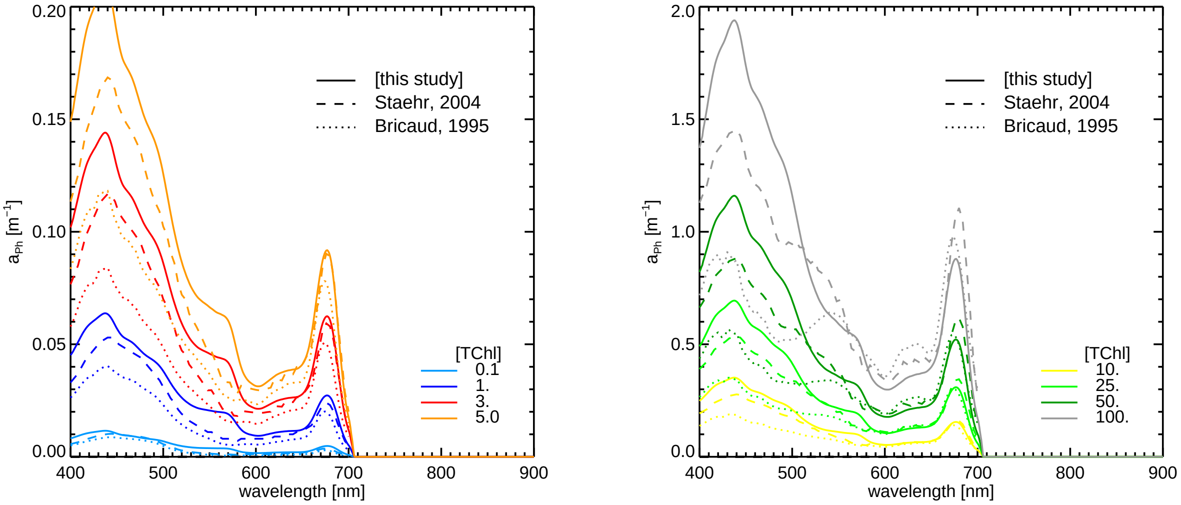

Figure 4.6: Comparison of bulk phytoplankton absorption for different models and concentrations.

Table 4.3: Setup for a_{Ph}-model sensitivity corresponding to Fig. 4.7.

$\Delta[\%]$ = *model mixed phytoplankton* − *model cyanobacteria*										
λ	[TChl]	[TSM]	[YS]	AOT(550)	AM	ws	ps	θ	θ_0	ϕ
var.	*var.*	2.7	0.3	0.03	1	7.2	1040	0	41	180

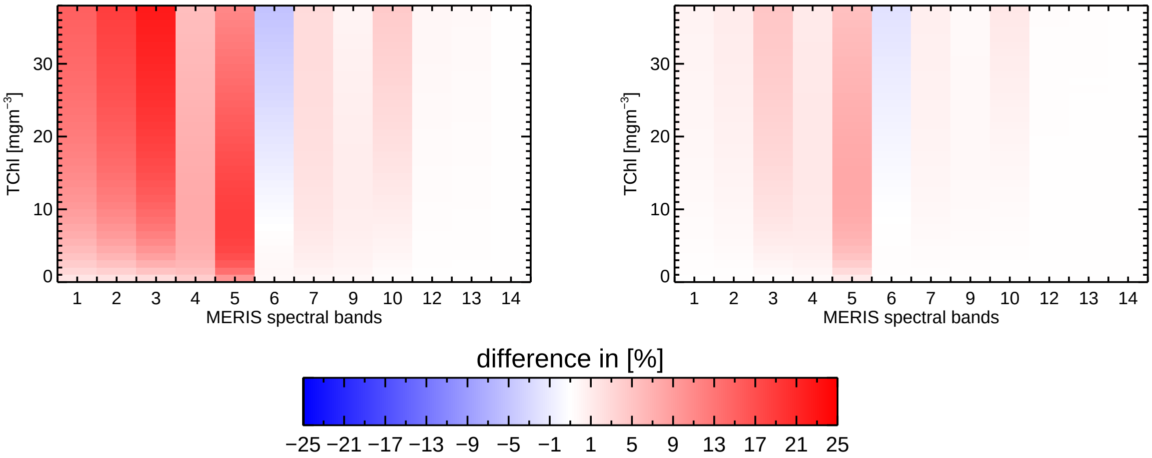

Figure 4.7: Impact of the parameterization of a_{Ph} on spectral remote sensing reflectance field and spectral TOA radiance (right).

Non-algal Particle Absorption a_{NAP} is modeled as given in Eq. (3.3) following Babin et al. (2003) with a parameterization derived from *in-situ* measurements in the South Baltic Sea. Absorption coefficient a_{NAP} and slope value S_{NAP} are listed in Tab. 4.6 and S_NAP is also given in Tab. 4.4. a_{NAP} and S_{NAP} vary little between geographical regions. For the Baltic Sea, the absorption in the blue spectral range is dominated by YS which is in most cases higher than NAP absorption (Kratzer et al., 2008).

Yellow Substance Absorption a_{YS} is parameterized as given in Eq. (3.2) with model parameters published by Schwarz et al. (2002), who compared a_{YS} models of different seas and showed maximum slope values for the Baltic Sea compared to others. Statistics of the slope value S_{YS} is listed in Tab. 4.4. Fig. 4.8 illustrates the spectral behaviour for YS absorption for two models: (1) Babin (2000) with $S_{YS} = 0.0176$, which is valid for most coastal regions and (2) Schwarz et al. (2002), with $S_{YS} = 0.0193$, which is valid for the Baltic Sea.

Table 4.4: YS and NAP model for the Baltic Sea, Ref.[1]: Schwarz et al. (2002), Ref.[2]: Babin et al. (2003).

S_{YS}				S_{NAP}				Ref.
MIN	MAX	AV	SD	MIN	MAX	AV	SD	
-	-	0.0193	0.0024	-	-	-	-	[1]
0.0177	0.0198	0.019	0.0005	0.0114	0.0147	0.013	0.0007	[2]

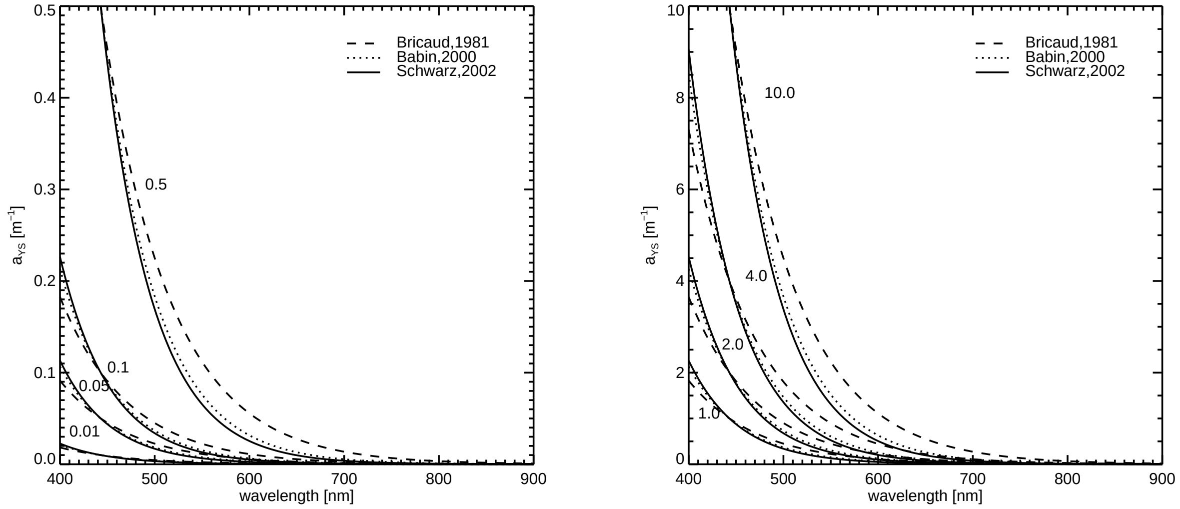

Figure 4.8: Comparison of spectral a_{YS} absorption coefficient parameterization normalized at 443nm for small to high YS absorption (left) and very high YS absorption (right).

The influence of S_{YS} is illustrated in Fig. 4.9. The average slope value S_{YS} of 0.0176 is valid for most coastal regions and is taken as the reference to which the differences are calculated. Negative differences indicate a gain in radiance or reflectance compared to the reference. The left panel of Fig. 4.9 shows differences in MERIS remote sensing reflectance for the Schwarz et al. (2002) model with a maximum of -16% in band 5 for high a_{YS}. For a typical background a_{YS} value of $0.2\,\mathrm{m}^{-1}$ the difference is -5%. The figure indicates that a S_{YS} valid for the specific region has to be considered. S_{YS} influences the water-leaving signal in the blue spectral range with maximum differences around 560 nm, which is the band most sensitive for phytoplankton abundance. Comprising, the influence of YS absorption in the Baltic Sea is twofold:

- the high YS amount with a typical value of $0.2\,\mathrm{m}^{-1}$ is reducing the water-leaving signal, and
- the steeper slope S_{YS} is increasing the water-leaving radiance for longer wavelength than the reference wavelength and is decreasing radiances at shorter wavelength.

Table 4.5: Parameters for sensitivity study shown in Fig. 4.9.

Δ [%] = *coastal model* (S_{YS} = 0.0176) − *baltic model* (S_{YS} = 0.019)										
λ	[TChl]	[TSM]	[YS]	AOT(550)	AM	ws	ps	θ	θ_0	ϕ
var.	4.0	2.7	*var.*	0.03	1	7.2	1040	0	41	180

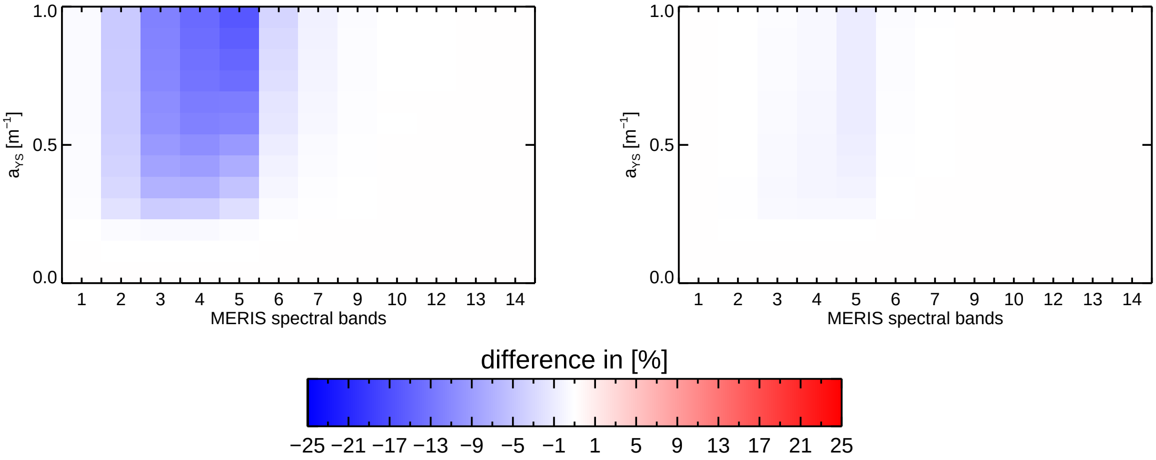

Figure 4.9: Impact of S_{YS} on remote sensing reflectance (left) and TOA radiances (right).

Table 4.6: Parameterization of IOPs of in-water constituents for the Baltic Sea.

Constituent	IOP Parameterization or Measurement	Ref.
Seawater:	$a_W(\lambda)$: directly measured	Pope and Fry (1997)
		Hale and Querry (1973)
	$b_W(\lambda) = 0.00288(\lambda/500)^{-4.32}$	Morel (1974)
	$p_W(\Psi) = 0.06225(1+0.835cos^2\Psi)$	Morel (1974)
Ph:cyano.	$a_{Ph}(\lambda) = A_{aPh}(\lambda)[Chla]^{B_{aPh}(\lambda)}$, with:	
	$A_{aPh}(\lambda)$, $B_{aPh}(\lambda)$: tabulated	this study
	$b_{Ph}(\lambda) = (\frac{550}{\lambda})\ A_{bPh}[Chla]^{B_{bPh}}$, with:	
	$A_{bPh} = 0.416, B_{bPh} = 0.766$	Babin (2000)
	$p_{Ph}(\Psi)$: directly measured	Volten et al. (1998)
Ph:mix.	$a_{Ph}(\lambda) = A_{aPh}(\lambda)[Chla]^{B_{aPh}(\lambda)}$,	
	$A_{aPh}(\lambda)$, $B_{aPh}(\lambda)$: tabulated	Bricaud et al. (1998)
NAP	$a_{NAP}(\lambda) = a_{NAP}(443)\exp(-(S_{NAP} \times (\lambda - 443)))$, with:	
	$S_{NAP} = 0.013$, $a_{NAP}(443) = 0.0216[TSM]^{1.0247}$	Babin et al. (2003)
	$b_{TSM}(\lambda) = A_{TSM}(\lambda)\ b^*_{TSM}(555)[TSM]$	Babin (2000)
	$b^*_{TSM}(555) = 0.49$, $A_{TSM}(\lambda)$: tabulated	Babin et al. (2003)
	$p_{TSM}(\Psi) = f([Chla]/TSM, \Psi)$	Zhang et al. (2003)
YS	$a_{YS}(\lambda) = a_{YS}(443)\exp(-(S_{YS} \times (\lambda - 443)))$, with:	
	$S_{YS} = 0.0193$, $a_{YS}(443)$: varying	Schwarz et al. (2002)

4.2.2 Parameterization of Scattering

Light scattering in the oceans is the 'first-order determinant for reflectance variability' as stated by Babin et al. (2003) and others. Scattering characteristics are very rarely measured, less often than absorption or concentrations. Particulary problematic is the assessment of the spectral behaviour of the scattering coefficient $b(\lambda)$ and the volume scattering function VSF $\beta(\Psi, \lambda)$. Comprehensive information on scattering in Baltic Sea waters are given in Babin (2000).

The *in-situ* measured scattering coefficient is the scattering coeffient of total suspended matter (TSM) b_{TSM}, that is: $b_{TSM}(\lambda) = b_{NAP1}(\lambda) + b_{NAP2}(\lambda) + b_{Ph}(\lambda)$. TSM are all organic and inorganic suspended particles. TSM weight, measured per unit volume seawater in $[\mathrm{g\,m^{-3}}]$, is a routinely measured bio-geophysical parameter in coastal waters. Here, non-algal particle scattering is given in relation to TSM dry weight following Eq. (3.8). The spectral mass-specific scattering coefficients b^*_{TSM} for the Baltic Sea are taken from Babin et al. (2003). $b_{TSM}(\lambda)$ is shown in Fig. 4.10, left panel, for varying concentrations, showing only a small spectral variability. Right panel of Fig. 4.10 shows the difference to the commonly used parametrization for coastal waters $b_{TSM}(\lambda) = 0.5[TSM]$, which does not account for a spectral variation. Maximum differences of 2 to $3\,\mathrm{m^{-1}}$ occur around 690 nm for a very high concentration of $25\,\mathrm{gm^{-3}}$ TSM.

Interestingly, the study by Babin et al. (2003) identified similar $b^*_{TSM}(555)$ of about $0.5\,m^2g^{-1}$ for different European coastal waters as the English Channel and the North Sea. $b^*_{TSM}(555)$ for the Baltic Sea is $0.49\,m^2g^{-1}$.

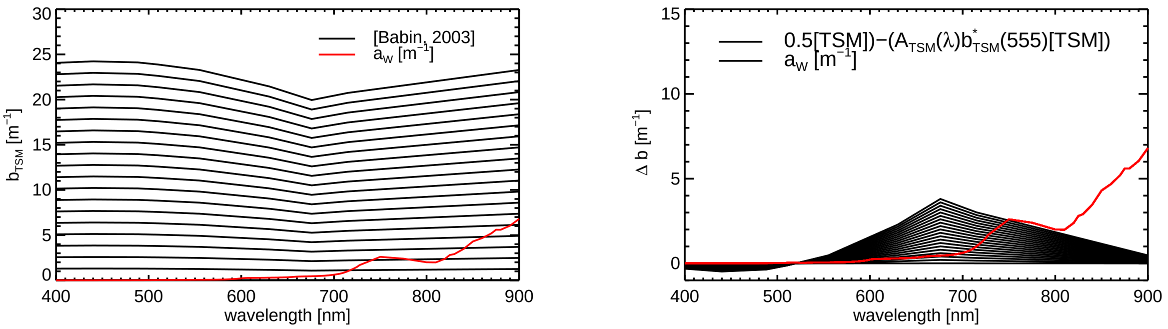

Figure 4.10: Scattering of TSM in the Baltic Sea, parameterized as given by Babin et al. (2003) (left) and the difference to the standard parameterization of $b_{TSM}(\lambda) = 0.5[TSM]$.

Phase functions: The angular dependency of scattering is rarely studied. Volten et al. (1998) performed laboratory measurements of light scattering from eight marine phytoplankton species. They published phase functions $p(\Psi)$ measured between 20° and 135° shown in Fig. 4.11. The angular distribution is restricted due to the measurement setup with a high bias for very small and very high angles caused by unwanted specular reflectance. This effect can be seen also for angles between 130° to 160° in Fig. 4.11. The strong forward peak below 20° and the backward scattering above 135° are extrapolated as given in Volten et al. (1998). The measured $p(\Psi)$ is

for the cyanobacteria species *Anabena*.
For mixed phytoplankton community structures the phase function parameterization of Zhang et al. (2003) is applied. It accounts for the ratio of $[TChl]$ to TSM concentration and also for the wavelength dependence.

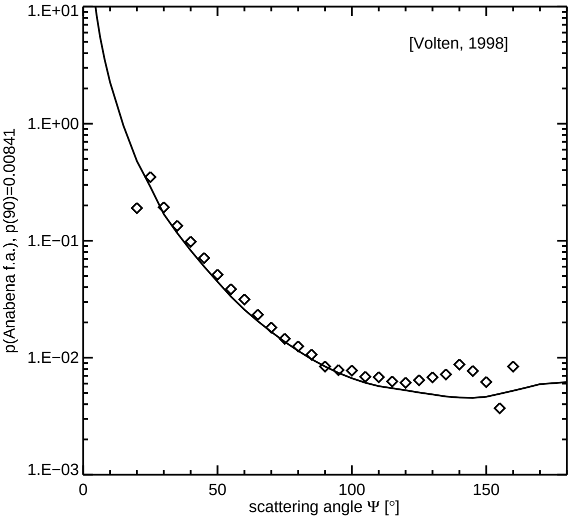

Figure 4.11: Phase function $p_{Ph}(\Psi)$ measured ($\Diamond$) and functional fit (solid line) by Volten et al. (1998) for the cyanobacteria *Anabena*. $p_{Ph}(\Psi)$ with given normalization to 90° with p(90°)=0.00841.

4.2.3 Concentration Ranges and Dependencies

The bio-optical models also describe the concentration ranges and dependencies of the bio-geophysical parameters. An overall collection of typical ranges *in-situ* measured is comprised in Tab. 4.7. Phytoplankton mass is given as the varying pigment concentration from 0.1 to 25 $\mathrm{mg\,m^{-3}}$ over three orders of magnitude for mixed phytoplankton and from 0.1 to 100 $\mathrm{mg\,m^{-3}}$ over four orders of magnitude for cyanobaterial biomass. TSM concentrations vary about three orders of magnitude from 0.1 to 35 $\mathrm{g\,m^{-3}}$, and YS about two orders of magnitude from 0.1 to 2.5 $\mathrm{m^{-1}}$. The histogram distributions of the log-scaled concentrations utilized within this bio-optical model are shown in Fig. 4.12.

The correlation ranges of the bio-geophysical parameters derived in this work are based on *in-situ* data from Babin (2000) and Kratzer et al. (2008) and are shown in Fig. 4.13. Lower and upper boundaries are defined by:

$$TSM([Chla])_{min} = 0.2[Chla]^{0.49}, \quad TSM([Chla])_{max} = 11[Chla]^{0.49} \tag{4.2}$$

$$YS([Chla])_{min} = 0.11[Chla]^{0.16}, \quad YS([Chla])_{max} = 0.9[Chla]^{0.16} \tag{4.3}$$

Fig. 4.14 shows the distribution of the concentrations of $[Chla]$, TSM and YS in the way utilized for the radiative transfer simulations. Presented are the data points, which are randomly selected accounting for Eq. (4.2) and Eq. (4.3) as well as the minimum and maximum ranges are shown.

Table 4.7: In-water concentration ranges in the Baltic Sea. Ref.[1]: Kratzer et al. (2008), Ref.[2]: Siegel et al. (2003), Ref.[3]: Babin et al. (2003), Ref.[4]: Darecki and Stramski (2004), Ref.[5]: Olsonen (2008)

Region	[*Chla*]			TSM			YS			Ref.
	MIN	MAX	AV	MIN	MAX	AV	MIN	MAX	AV	
Himmerfjärden	1.5	5.8	4.0	0.68	1.8	1.45	0.33	0.68	0.5	[1]
Open Baltic	-	-	2.2	-	-	0.92	-	-	0.42	[2]
Oder Lagoon	-	-	-	-	-	-	1.0	2.2	-	[2]
Greifswald Bay	3.0	20	-	4.0	32	-	0.5	1.3	-	[2]
Pomeran. Bight	0.5	18	-	1.0	14	-	0.2	0.9	-	[2]
Western Baltic	0.3	9.0	-	1.0	6	-	0.2	0.5	-	[2]
South Baltic	2.21	28.95	9.3	0.51	14.7	2.3	0.20	0.62	0.33	[3]
Baltic	0.3	100	2-3	-	-	-	-	-	-	[4]
Baltic	0.3	22.0	-	-	-	-	-	-	-	[5]
this study	0.1	25/100	-	0.1	35	-	0.1	2.5	-	

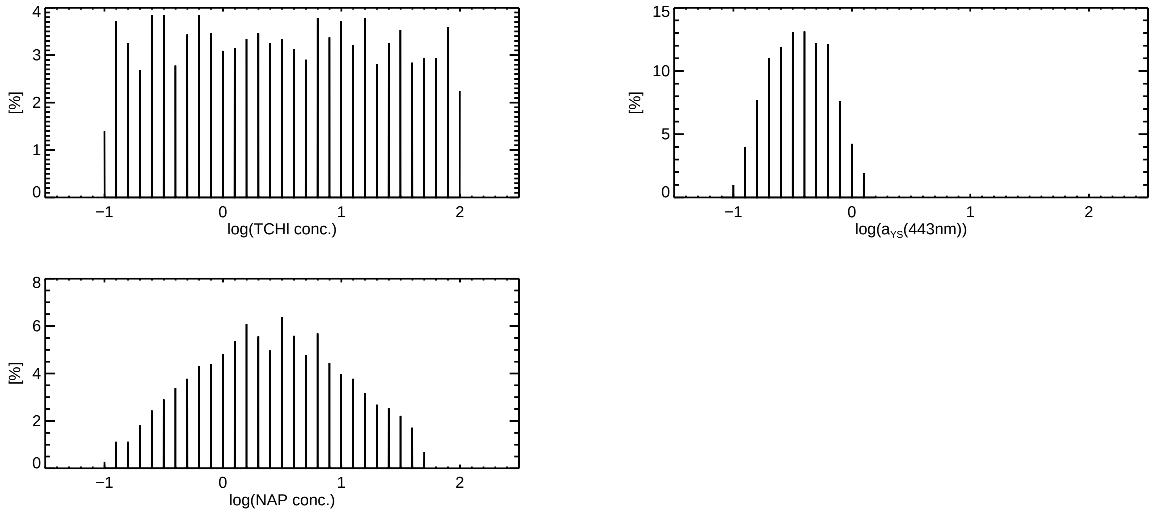

Figure 4.12: Histogram distribution of (a) [*Chla*], (b) YS, and (c) TSM for the Baltic Sea bio-optical model.

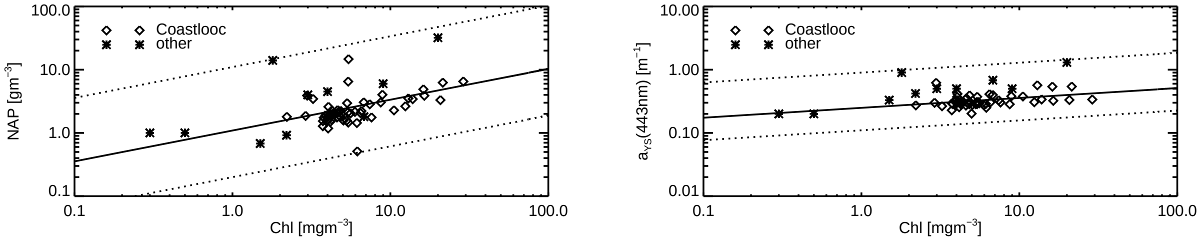

Figure 4.13: Scatter plots of TSM against [*Chla*] (left) and YS against [*Chla*] (right) as derived from *in-situ* data of Babin et al. (2003) and Kratzer et al. (2008).

The solid lines in Fig. 4.14 indicate the upper and lower concentrations as accounted for in the FUB-Case2 algorithm for standard coastal waters developed by Schröder (2005).

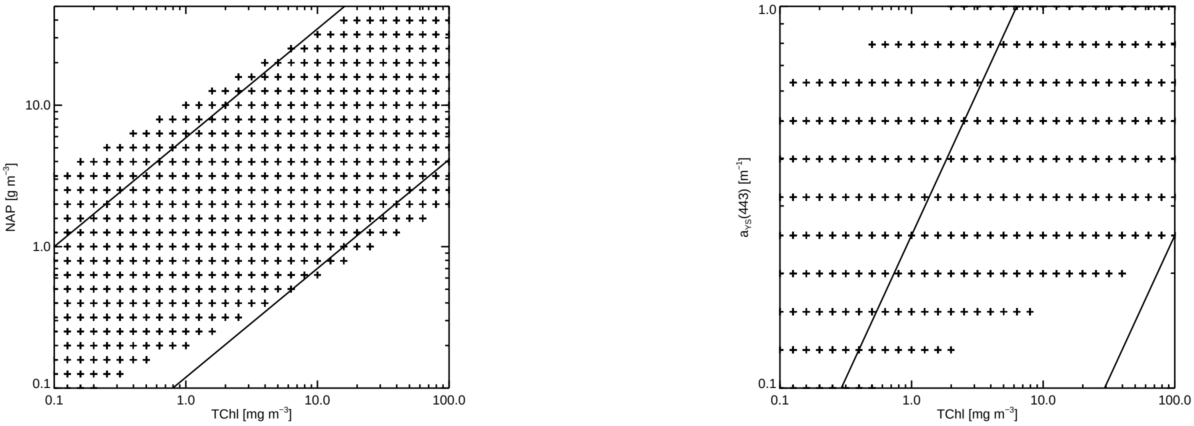

Figure 4.14: Concentration ranges of [*Chla*] vs. NAP (left) and [*Chla*] vs. YS (right) for the Baltic Sea bio-optical model.

4.2.4 Sensitivity

The sensitivity of remote sensing reflectance R_{RS} and TOA radiance L_{TOA} to parameters of the bio-optical model is studied. For increasing YS absorption and [*Chla*] concentrations simulated R_{RS} for MERIS spectral band 3 at 490 nm are shown in Fig. 4.15. Increasing YS leads to decreasing R_{RS} and increasing [*Chla*] increases reflectance. When YS absorption is dominating the signal, only small differences in R_{RS} can be seen for changing [*Chla*] at 490 nm. For high [*Chla*] concentration, YS absorption can be distinguished better from the reflectances because of the higher signal. The shown sensitivity of Fig. 4.15 can be also observed for the other MERIS bands in the blue and green spectral range.

An increase in TSM leads to an increase of R_{RS} and L_{TOA} throughout the spectrum. For MERIS spectral band 5 at 560 nm the sensitivity for increasing [*Chla*] and TSM is shown in Fig. 4.16.

Table 4.8: a

nd YS.]Setup for sensitivity study for changing [*Chla*] and YS corresponding to Fig. 4.15.

λ	[TChl]	[TSM]	[YS]	AOT(550)	AM	ws	sp	θ	θ_0	ϕ
490 nm	*var.*	2.7	*var.*	0.03	1	7.2	1040	0	41	180

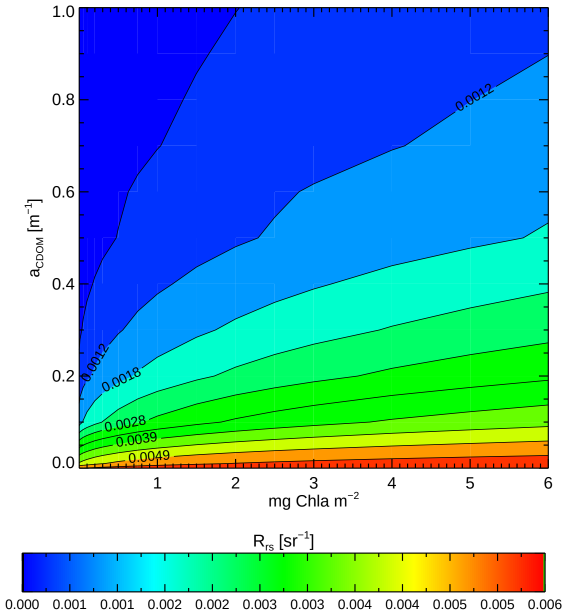

Figure 4.15: Remote sensing reflectance R_{RS} at 490 nm for varying YS absorption and $[Chla]$ concentration.

Table 4.9: Setup for sensitivity study for changing $[Chla]$ and TSM corresponding to Fig. 4.16.

λ	[TChl]	[TSM]	[YS]	AOT(550)	AM	ws	sp	θ	θ_0	ϕ
560 nm	*var.*	*var.*	0.3	0.03	1	1.5	980	0	41	180

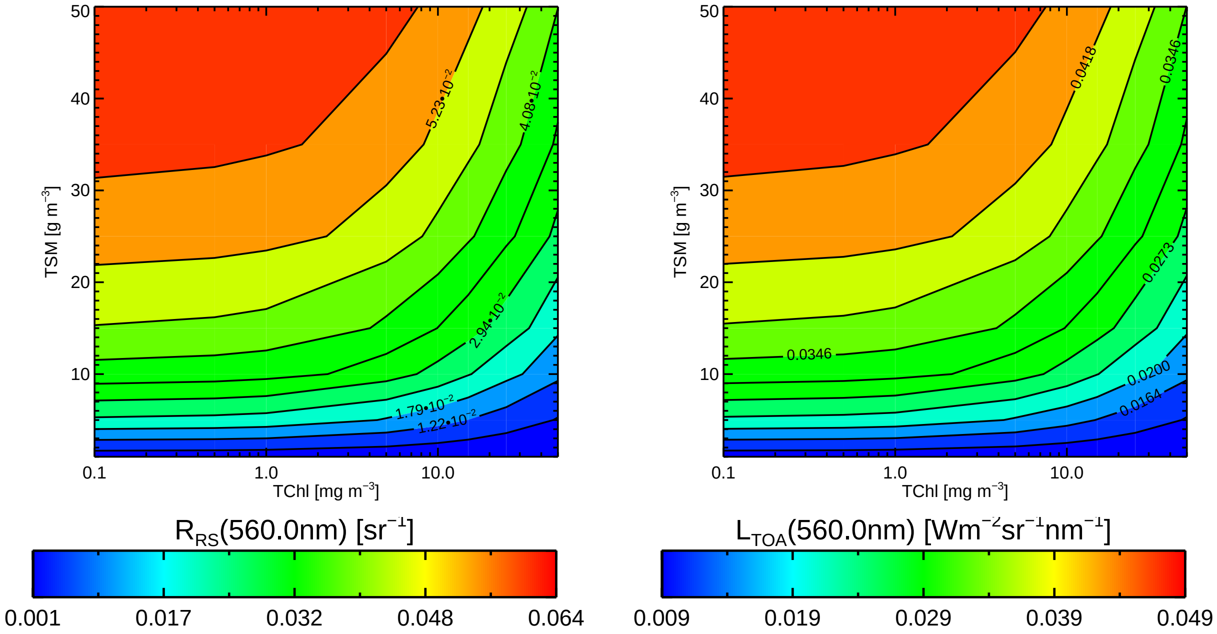

Figure 4.16: Remote sensing reflectance R_{RS} at 490 nm for varying TSM absorption and $[Chla]$ concentration.

4.2.5 Effects of Vertical Stratification

Fig. 4.18 shows and example of measured radiance reflectances R_W (for calculation compare Tab. 2.1) in the Baltic Sea for a mixed phytoplankton bloom occuring in spring (left panel) and a cyanobacterial bloom occuring in July (right panel). The upper plots show L_{TOA} measurements, the lower plots the derived R_W. The R_W signal is simulated and explained by an increasing phytoplankton concentration for the spring bloom condition, which is shown in Fig. 4.17. For the cyanobacterial bloom condition shown in the right panels of Fig. 4.17, the very high R_W values occuring with a specially pronounced effect for MERIS band 5 at 560 nm and a second peak at709 nm could not be explained with the chosen bio-optical model setup except with very high and dominating TSM concentrations.

Cyanobacteria contain gas vacuoles, which allow them to adjust in the water column. The effect of a vertical stratified phytoplankton bloom is tested with MOMO simulations. Fig. 4.19 shows a phytoplankton bloom placed in different depth levels in the water column. Extinction coefficient c and single-scattering albedo ω_0 are varying with depth depending on the phytoplankton concentration. The effect on R_{RS} and L_{TOA} is demonstrated in Fig. 4.20. When phytoplankton is exposed to the sea surface, R_{RS} increases with distinct features around 560 nm and additionally in the nIR around 709 nm. The effect can be explained with an decreasing influence of water absorption for phytoplankton surface accumulation.

The influence of a vertical stratification is shown in Fig. 4.21 in form of a look-up table for L_{TOA}. The influence of varying depth for the $[Chla]$ maximum on radiance ratios is small but it can be observed. The deeper the $[Chla]$ maximum in the water column, the higher the influence of water absorption and the lower is the ratio value.

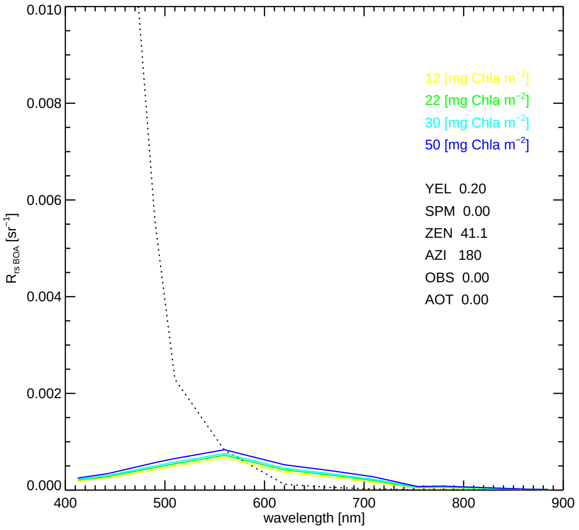

Figure 4.17: R_RS for MERIS spectral bands for varying $[Chla]$.

The influence of varying depth for phytoplankton can not be considered in the bio-optical model but is theoretically studied here and applied for the derivation of the cyanobacteria mask based on the shown thresholds.

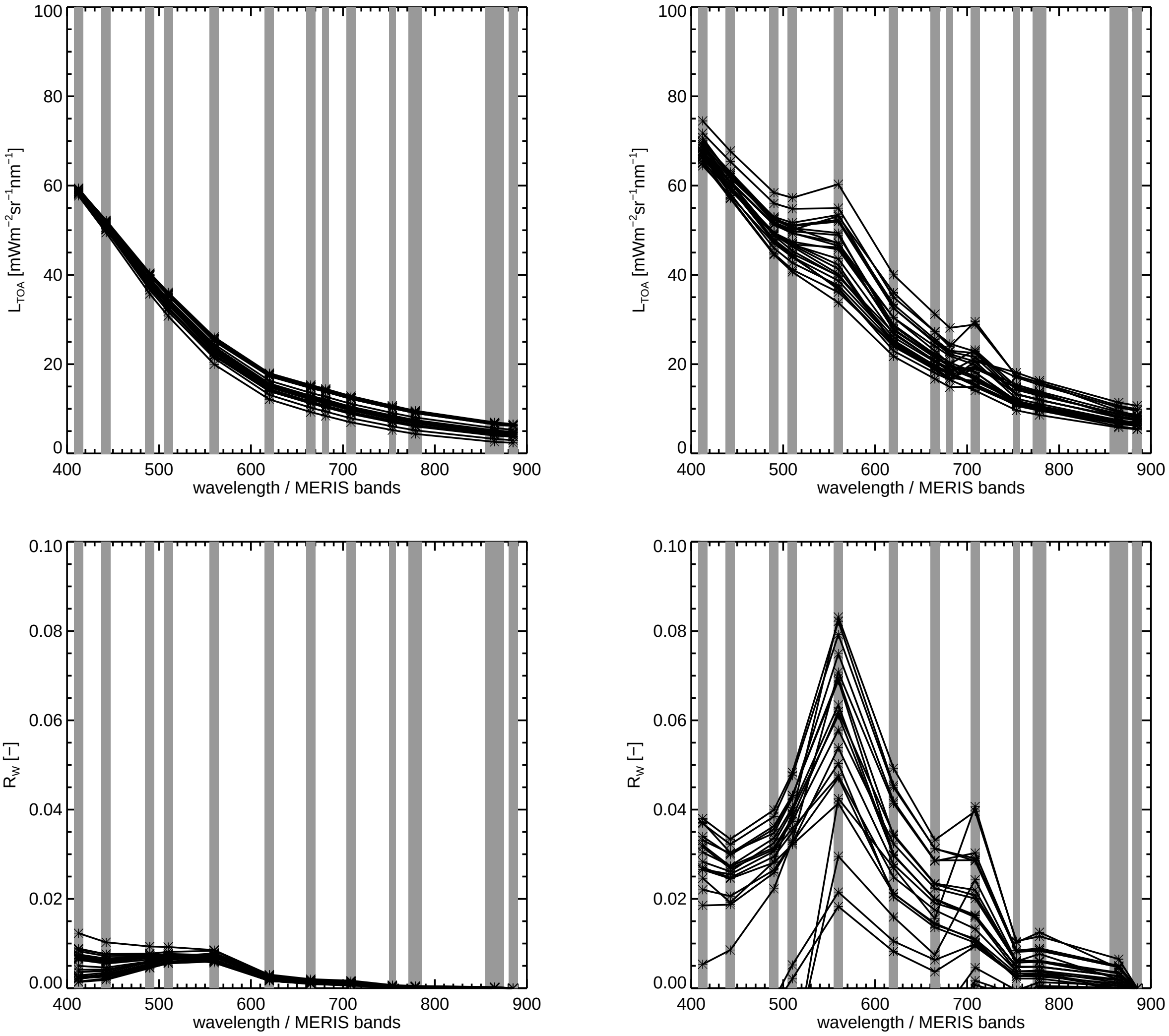

Figure 4.18: Example of spectral measurements by MERIS of L_{TOA} (upper panel) and R_W (lower panel) for a mixed phytoplankton bloom in May (left panel) and for a heavy cyanobacterial bloom in July (right panel).

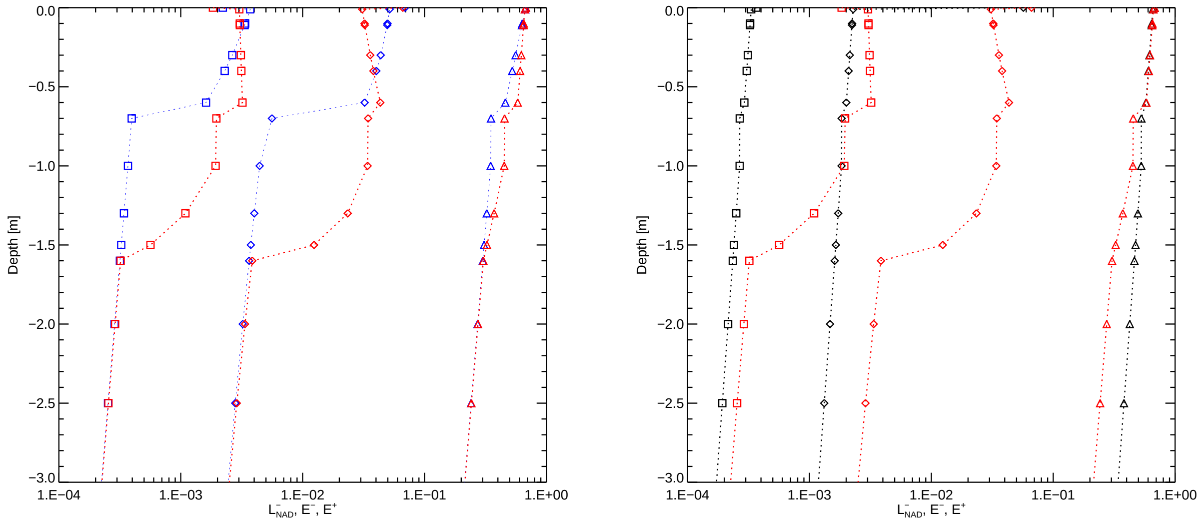

Figure 4.19: Example of a stratified phytoplankton bloom centered at -0.3 m (blue curve) and -1.0 m (red curve) in left panel. The right panel shows homogeneous distributed [*Chla*] (black curve) and the same [*Chla*] distributed between -0 and -1.5 m depth (red curve).

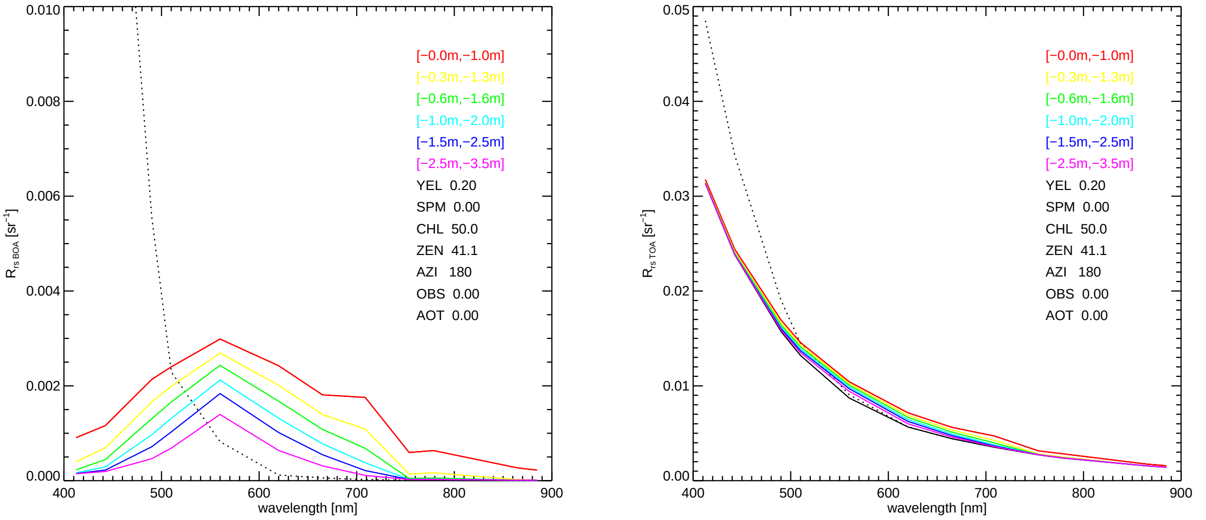

Figure 4.20: Example of a stratified phytoplankton bloom with varying depth of maximum concentration.

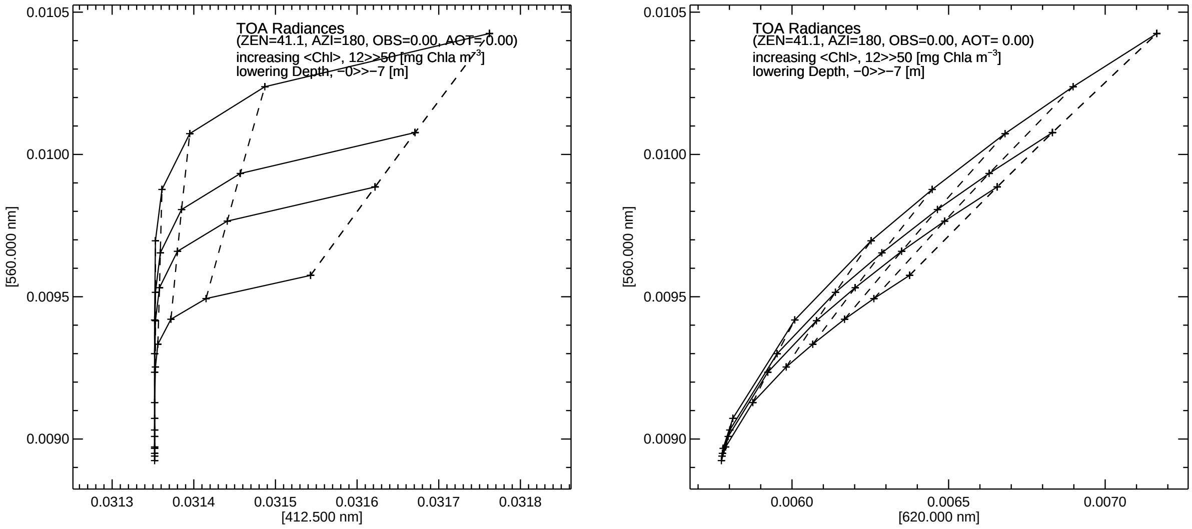

Figure 4.21: Look-up table diagrams for $L_{TOA}(412.5\,\mathrm{nm})$ against $L_{TOA}(560\,\mathrm{nm})$ (left) and $L_{TOA}(620\,\mathrm{nm})$ against $L_{TOA}(560\,\mathrm{nm})$ (right). Solid lines are lines of varying $[Chla]$. Dashed lines are lines varying bloom depth. The depth for maximum $[Chla]$ concentration is increasing from high to low L_{TOA}. $[Chla]$ is increasing from high to low L_{TOA}.

4.2.6 Discussion of the Bio-optical Model for the Baltic Sea

The studied R_{RS} and L_{TOA} are depending on the concentration of the in-water constituents and their spectral parameterization. The containment of typical concentration ranges and their inter-dependencies restricts the number of possible non-linear relationships between the optical properties and radiances, which results in a more stable inversion and retrieval. The Baltic Sea YS absorption differs compared to other seas, the slope of YS absorption and the concentration range has to be considered.
The results of the sensitivity study for the Baltic Sea bio-optical model are:

- a steeper slope of YS absorption is decreasing radiances for MERIS bands shorter than the reference wavelength,
- the typically higher YS absorption is decreasing the radiance field for all wavelengths from 412.5 to 620 nm,
- TSM scattering in the Baltic Sea compared to other coastal regions leads to higher reflectances from 600 to 800 nm,
- the non-linear increase of phytoplankton absorption with increasing $[Chla]$ reduces the maximum total absorption with a highest impact for high phytoplankton concentration,
- phytoplankton dominated by cyanobacterias compared to a mixed phytoplankton community is decreasing radiances for all MERIS spectral bands due to the higher absorption, except for band 6 at 620 nm, and
- phytoplankton abundance is increasing the reflectance field in all wavelength from 412 to 700 nm, foremost at 560 nm for MERIS spectral band 5. The effect increases for phytoplankton abundance close to the sea surface.

4.3 Algorithm Performance and Sensitivity

The Baltic Sea regional algorithm accounts for the specific optical properties occuring in the Baltic. In the following the algorithm is called FUB-Baltic and the derived bio-geophysical products are:

- remote sensing reflectance R_{RS} in eight MERIS spectral bands,
- chlorophyll-a concentration $[Chla]$,
- total suspended matter concentration TSM,
- yellow substance absorption at 443 nm YS, and
- the cyanobacterial flag mask based on threshold values of R_{RS}

The general performance of the ANN inversion is tested against an unseen test data set and the error measures $RMSE$ and $BIAS$ are calculated as described in 3.2.2 with formulas given in the Eq. (3.16) and Eq. (3.17). Section 3.2.2 describes that four ANNs have been trained with varying numbers of neurons in the hidden layer for all products. Compared to the FUB-Case2 algorithm developed by Schroeder et al. (2007a) the $RMSE$ for the selected ANNs of the FUB-Baltic products is in the same order of magnitude and slightly lower (compare to Schröder (2005)).

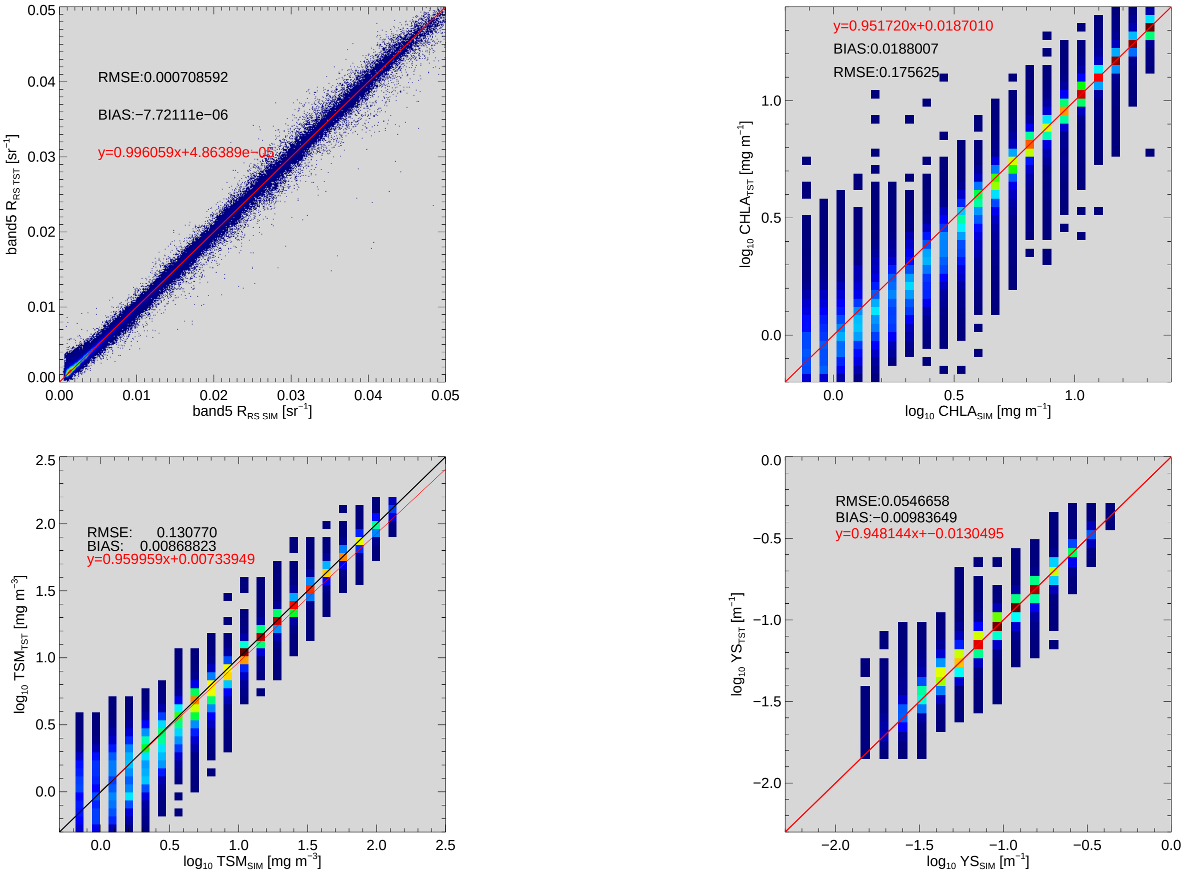

Figure 4.22: Comparison of retrieved FUB-BALTIC bio-geophysical products against the simulated test data.

4.4 Cyanobacterial Bloom and Surface Accumulation Mask

In section 4.2.5 it is discussed, that the exceptional water signal in the Baltic Sea in summer is a combined efffect of increasing chlorophyll-a concentration and surface accumulation of the cyanobacteria floating in the water column. The effect measured by satellite sensors is mainly the effect of surface accumulation. Therefore, the cyanobacterial abundance mask is only valid for cyanobacterial exposed to the sea surface as well as it is only valid for the Baltic Sea as surface accumulation by other phytoplankton can also occure.

The mask is setup the following way: first the derived R_{RS} are normalized to solar downwelling

irradiance and it is checked if they are in an offset range. Then ratios from all R_{RS} are calculated, the denominator is R_{RS} at 560 nm. If all these ratios are smaller than 1, which means $R_{RS}(560\,\mathrm{nm})$ is the highest value, then the signal is from phytoplankton rather than from TSM. In next three steps it is checked if the ratios 620 nm/560 nm, 709 nm/560 nm, and 490 nm/510 nm indicate a steep slope.
Fig. 4.24 shows an example of MERIS L_{TOA} measurements for an overflight during a cyanobacterial bloom occuring from 5th to 20th July 2005. The lower Fig. 4.23 shows the derived cyanobacterial surface accumulation mask. The left panel of Fig. 4.23 is for a MERIS overpass on 2005-05-13 with phytoplankton abundance but no surface accumulation. Fig. 4.24 shows an example of MERIS L_{TOA} measurements for an overflight during a cyanobacterial bloom occuring from 5th to 20th July 2005.

Table 4.10: FUB-BALTIC cyanobacterial mask setting.

Parameter	Min	Max	Operator
$R_{RS}412.5nm$	0.006	0.028	AND
$R_{RS}560.0nm$	0.048	0.019	AND
$R_{RS}620.0nm : R_{RS}560.0nm$	0.5	0.7	AND
$R_{RS}490.0nm : R_{RS}510.0nm$	0.7	0.9	AND
$R_{RS}709.0nm : R_{RS}560.0nm$	0.2	0.6	

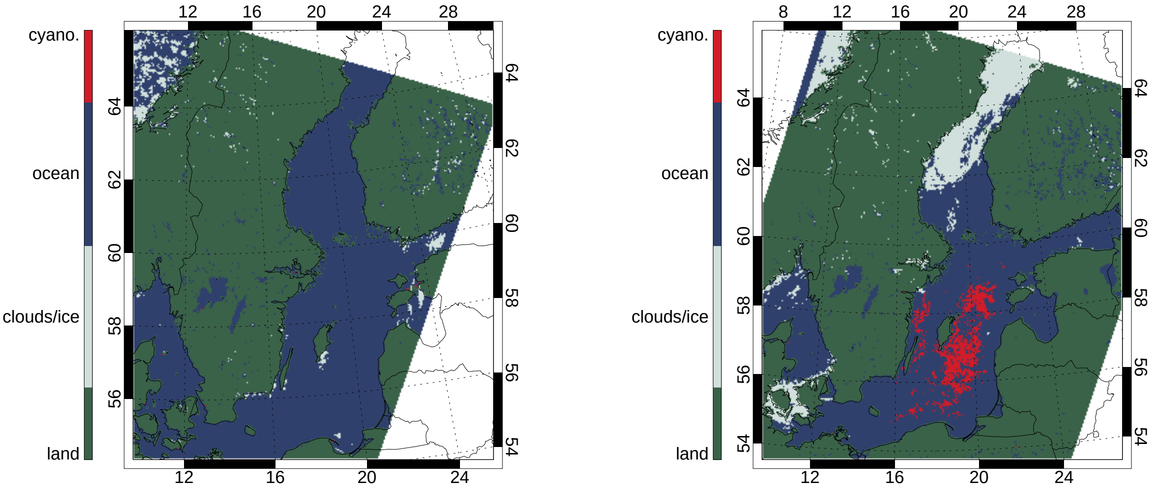

Figure 4.23: Example of the cyanobacteria bloom mask for the Baltic Sea. Left: 2005-05-13: 09:50UTC, orbit 16738 and right: MERIS 2005-07-13, 09:32UTC, orbit: 17611.

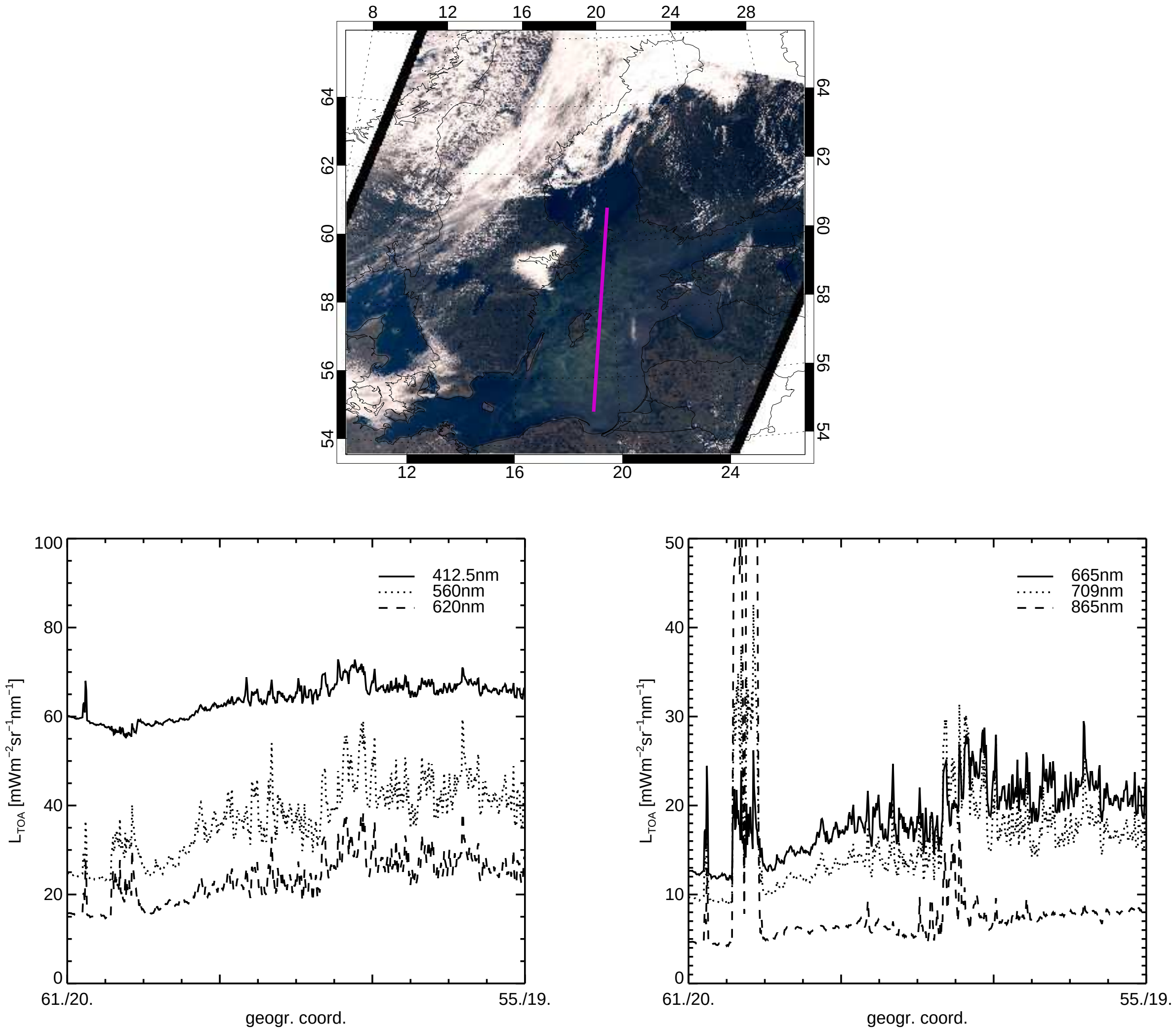

Figure 4.24: Example of MERIS measurements. Upper left panel: FUB-RGB composite with a transect for which MERIS Level-1b L_{TOA} is shown. MERIS 2005-07-13, 09:32UTC, orbit: 17611.

4.5 Comparison of Derived Bio-geophysical Producs

The retrieval products have been compared to *in-situ* data provided by Dr. S. Kratzer, who collected match-up samples in fjord Himmerfjärden at the Swedish coast south of Stockholm. The samples have been collected during MERIS overpassed in August 2002, between 9th August 2002 to 27th August 2002. The data have been collected along a transect from the coast line towards the open Baltic Sea. The data is nicely presented in Kratzer et al. (2008).

For 14 *in-situ* samples cloud free MERIS data points are found. 11 of the 14 match-up samples passed the test, if the MERIS derived products are within the valid minimum/maximum range of the algorithm.

The 11 valid data points are plotted in Fig. 4.25 with the $RMSE$ and $BIAS$ tabulated in Tab. 4.11. $RMSE$ and $BIAS$ are defined in Eq. (3.16) and Eq. (3.17). The $RMSE$ gives the

magnitude of the variation. The $BIAS$ gives the systematic differences.
It is noted that the validation results are preliminary. All MERIS YS products derive YS absorption at 443 nm while the *in-situ* data is YS absorption at 440 nm. The satellite derived products are not corrected for the difference. Also, the ESA-Level-2 product is YSBPA, which is the sum of yellow substance and bleached particle absorption. The coastal waters of fjord Himmerfjärden contain detritus. The ESA-Level-2 YSBPA product is not corrected for bleached particle absorption and also the *in-situ* BPA absorption is not known.
In general, the FUB-Baltic products are expected to have an influence in regions with high TSM load because of a spectral signature of TSM scattering taken into account. Also, YS absorption is expected to be increased compared to the FUB-Case2 derived YS absorption. The reasons are discussed in 4.2.1.

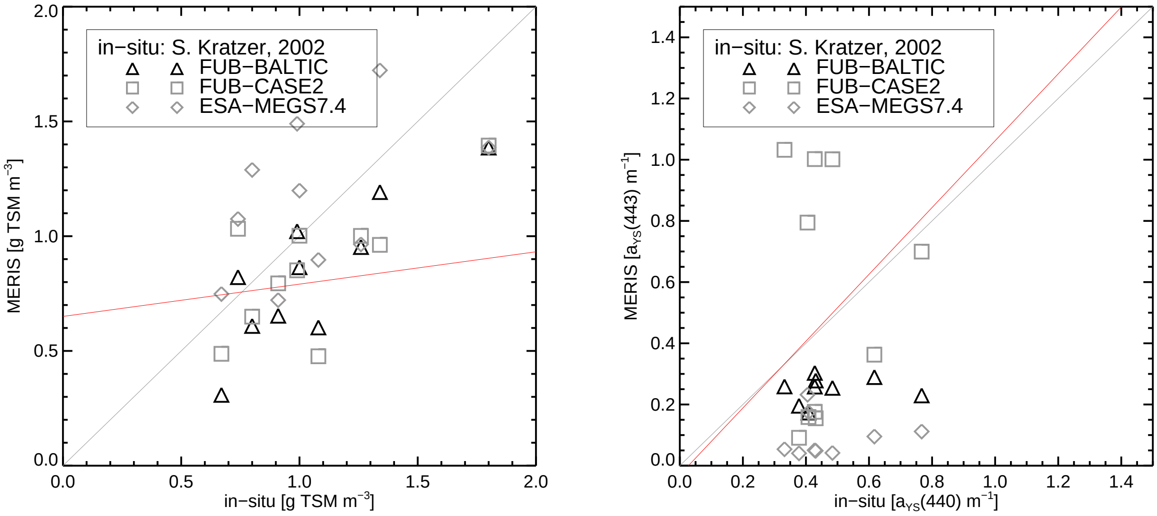

Figure 4.25: Comparison of retrieved products [$Chla$], TSM, and YS to *in-situ* data. *In-situ* data collected and owned by Dr. S. Kratzer, Kratzer et al. (2008). MERIS data: 2002-08-09, 2002-08-15, 2002-08-19, 2002-08-22, 2002-08-27.

Table 4.11: $RMSE$ and $BIAS$ for comparison of derived bio-geophysical products. *In-situ* data collected and owned by Dr. S. Kratzer, Kratzer et al. (2008). MERIS data: 2002-08-09, 2002-08-15, 2002-08-19, 2002-08-22, 2002-08-27.

	ESA Level-2, MEGS7.4	FUB-Case2	FUB-Baltic
$RMSE$-[Chla]	3.84505	2.05789	4.02261
$BIAS$-[Chla]	-2.53384	-0.783878	2.73424
$RMSE$-TSM	0.497224	0.72408	0.670967
$BIAS$-TSM	0.032846	0.37652	0.383805
$RMSE$-YS	0.460559	17.5079	0.5299
$BIAS$-YS	0.265873	-5.3499	-0.01538

4.6 Discussion and Conclusion

On-going work is the validation of the FUB-Baltic products. A detailed validation has to be performed for all FUB-Baltic bio-geophysical products when further *in-situ* data are available. It is planned, that data will be provided by Dr. D. Doxoran, who collected match-up samples in the Northern Baltic Sea in summer 2008, and also data by Dr. H. Siegel, who measured match-up samples in the South and open Baltic Sea during MERIS overpasses in summer 2002. A first comparison for match-up data along a transect from the coast line towards the open sea shows good results. Especially for YS absorption the $BIAS$ is reduced.

The phytoplankton bloom mask of FUB-Baltic flags regions of surface accumulation of cyanobacteria. In the masked regions, the FUB-Baltic products are not valid, since a vertical stratification and the high total absorption of cyanobacterias is not considered in the bio-optical model. For case studies, e.g., for specific *in-situ* measurement campaigns in high concentration areas of the open baltic Sea, the developed cyanobacterial bio-optical model containing high concentrations and cyanobacterial specific absorption can be used, as well as the trained ANN for a retrieval. it is possible to use the cyanobacteria-ANN for a retieval in the regions flagged by the cyanobacteria surface accumulation mask.

Chapter 5

Marine Particulate Inorganic Calcite Concentration Retrieval and the Detection of *Coccolithophore* Blooms

Coccolithophores receive much attention in climate change related research of the global marine ecosystem. As a calcifying phytoplankton species they are utilized to study the oceans response to anthrophognic carbon dioxide (CO_2) rise in the atmosphere. Often, coccolithophorids are treated as a *model species* to understand photosynthesis and oceanic calcification effects for changing atmospheric CO_2.

The first section of this chapter gives a very compact overview on the role of coccolithophores in the oceanic carbon cycle to motivate the importance of monitoring global coccolithophore biomass. In section 5.2 the optical properties are described. Following sections concentrate on the algorithm development to derive the oceanic particulate inorganic calcite concentration and the coccolithophore mask from MERIS Level-1b data.

5.1 Background

Coccolithophorids are an abundant and globally distributed phytoplankton species, which can form dense blooms on regional scales. Coccolithophores play an outstanding ecological and geochemical role in the oceanic carbon and sulfur cycle [Brown and Yoder (1994), Milliman et al. (1999)].

Together with diatoms and dinoflagellates, coccolithophores are the major producers of phytoplankton biomass, therefore their quantification as well as the assessment of their global distribution is important. Coccolithophores synthesize calcium carbonate platelets, which means they produce particulate inorganic carbon (PIC). With about 75% they are the primary source of calcareous sediments and therefore a potential long-term carbon sink although much is still uncertain about coccolithophore sinking rates and their role in the oceanic biological pump (Holligan et al., 1993).

Gregg (2007) expresses the need to understand the distribution of coccolithophores in the global ocean to expand our knowledge of oceans ecology and biogeochemistry. Their spatial and temporal characteristics need to be studied, as well as their interactions with the Earth system. Particulate inorganic carbon distribution maps can help to understand significant anomalies in alkalinity in the surface ocean, which results from the variability in calcification and dissolution (Balch et al., 2005), see section 5.1.1 for how coccolithophores affect regional CO_2 dynamics.

Blooms of coccolithophores have a significant radiative impact because they directly increase water albedo. Coccolithophorids also have an indirect effect on the atmospheric albedo through their cloud forming influence. Amongst phytoplankton, coccolithophores are the main precursor for sulfate aerosol dimethyl sulfide (DMS). DMS is the most important starting source for cloud condensation nuclei, and coccolithophores are the major biogenic source of sulfur for the atmosphere. Yet, little is known about the correlation of coccolithophore abundance and DMS concentration relative to other sources. Within intense coccolithophore blooms in the North Atlantic, Marandino et al. (2008) measured high DMS air/sea fluxes, that were larger than estimates from current models and parameterizations. This study suggests detailed research in high productive coccolithophore blooming regions.

5.1.1 The Oceanic Carbon Cycle

The carbon cycle is the bio-geochemical cycle of carbon exchange between plants and terrestrial biosphere, sediments, and the oceans. The ocean stores 93% of Earths CO_2 and the ocean surface is the largest active source of carbon. The oceans regulate atmospheric CO_2 in two ways:

- the ocean releases CO_2 into the atmosphere and
- the ocean is a potential sink of CO_2 reacting to an increase of partial pressure of CO_2 (pCO_2).

The ocean absorbs CO_2 from the atmosphere to reach equilibrium by direct air/sea exchange. When entering the water, CO_2 dissolves into the ocean. As it is reacting with the water (H_20), dissolved CO_2 is converted to carbonic acid (H_2CO_3). The cooler the seawater is the more carbonic acid is formed as the solubility of CO_2 increases. Therefore, cool, dense, and CO_2 enriched waters are transported to the sea bottom at the Earth's poles.

In the next step, H_2CO_3 ionizes to bicarbonate ions (HCO_3^-), which is the largest fraction of inorganic carbon in the oceans. In a second ionization, HCO_3^- is converted to carbonate ion (CO_3^{2-}). Together with calcium seasalts (Ca^{2+}), CO_3^{2-} convertes to calcium carbonate ($CaCO_3$). Each of the four reactions tends to reach its own local equillibrium depending on temperature, pressure, and the presence of ions.

The full dissolution reaction can be written as:

$$CO_2 + CaCO_3 + H_2O = 2HCO_3^- + Ca^{2+} \tag{5.1}$$

with

$$CaCO_3 = Ca^{2+} + CO_3^{2-}. \tag{5.2}$$

The reaction equation shows, that dissolution increases as a function of changes in $CaCO_3$ with an enrichment of CO_2 in water. The formation of $CaCO_3$ lowers sea water alkalinity. Alkalinity, or in other words ocean's acidity, controls the atmospheric CO_2 but also oceans acidity increases with increasing CO_2, which is known as the on-going longterm acidification of the oceans. Eq. (5.1) and Eq. (5.2) further show the dependence of oceanic CO_2 uptake on the availablity of carbonate ions (CO_3^{2-}). Changes in carbonate standing stocks are significant to the atmospheric CO_2 budget.

Calcification is the process of $CaCO_3$ production by phytoplankton. Coccolithophores are the major calcifying phytoplankton. The $CaCO_3$ produced by coccolithophores is a potential sink for particulate inorganic carbon (PIC). Global oceanic calcite production and calcification rates are estimated to be between 0.6 − 1.4 Gt PIC yr^{-1} [Milliman (1993), Wollast (1994)].

The net effect of increased pCO_2 on the downward flux of calcareous particulate matter is not fully known yet (Balch et al., 2005). This interrelation is crucial to climate change studies and bio-geochemical model forcing. Coccolithophorid blooms play a very important role in air/sea CO_2 exchange and within the global bio-geochemical cycle, but the ecological consequences are uncertain. Especially calcification processes are not completely understood yet. For example, during calcification, CO_2 is released, which increases pCO_2 in surface waters and serves as a potential source of CO_2 to the atmosphere. Resulting, coccolithophores change the oceanic CO_2 uptake and also change the CO_2 release to the atmosphere, but parameterizations are missing. Also, coccolithophorids respond to ocean acidification, which is another important ecosystem process under investigation.

As this section is very comprehensive, the review of Fasham (2003) describing the findings of the 15 years international program Joint Global Ocean Flux Study (JGOFS) is recommended for further reading on the bio-geochemistry of the marine carbon cycle. For a basic introduction on production and distribution of oceanic calcium carbonate, Broecker and Peng (1982), is suggested.

5.1.2 Occurences of *Emiliania huxleyi* Coccolithophore Blooms

Occurrences of oceanic coccolithophore blooms have often been recognized from satellite imagery and *in-situ* observations as white water showing a distinct milky-turquoise colour. Coccolithophorid blooms have been observed globally, with a magnitude in biological productive North Atlantic waters [Balch et al. (1991), Holligan et al. (1993)]. They can form intensive ($\gg 10.000\,\mathrm{cells\,ml^{-1}}$) and extensive ($50.000\,\mathrm{km^2}$) mono-specific blooms from oligotrophic subtropical to temperate and high-latitude semi-eutrophic waters. Calcite concentrations of about 40 to 50 $\mathrm{mg\,PIC\,m^{-3}}$ are typical for North Atlantic regions in summer. Blooms of coccolithophores are typically characterized by 300 to 400 mg PIC m^{-3} (Gordon and Balch, 1999). Highest concentrations have been measured with 1000 mg PIC m^{-3}.

Globally the most abundant calcifying species is *Emiliania huxleyi* (Westbroek and de Jong, 1983), which is taken primarily to characterize coccolithophores. Besides *E. huxleyi* only the species *Gephyrocapsa oceanica* is known to form large blooms detectable from space.

Coccolithophores are microphytoplankton with sizes of 15 to 200 μm. In the process of calcification the cells produce micrometer-size calcite platelets, the so-called coccoliths. Coccoliths, composed almost entirely of $CaCO_3$, scatter but do not absorb light (Ackleson et al., 1994), which causes the white-waters. Highly scattering, coccolithophore-dominated waters increase water column reflectance especially in the blue spectral range. Saturation effects for the MERIS spectral bands are not expected as the maximum reflectance of a bloom is in the range of a signal caused by clouds

A more extensive introduction to coccolithophorid blooms in global oceans is given, e.g., in Brown and Yoder (1994).

5.1.3 Algorithms for Coccolithophore Bloom Detection

Quantification of oceanic $CaCO_3$ using satellite measurements was first investigated by Brown and Yoder (1994) and Ackleson et al. (1994), later by Gordon et al. (2001) and Balch et al. (2005). Based on these works it is possible to derive the extent and intensity of coccolithophorid blooms from CZCS, SeaWiFS, and MODIS satellite data on a pixel-by-pixel basis. The MODIS and SeaWiFS operational algorithms are semi-analytical models which invert measured water-leaving radiances, requiring for a prior atmospheric correction. Absorption and scattering properties are related to concentrations through statistical analysis of direct *in-situ* measurements. An overview of publications on operational algorithms for coccolithophore bloom recognition from space is given in following Tab. 5.1. A number of case studies have also been performed on regional scale, e.g., by Ackleson et al. (1994), Tyrrell et al. (1999), Holligan et al. (1991), and others.

Table 5.1: Algorithms for coccolithophore bloom recognition from different satellite data. References [1]: Balch et al. (2005), [2]: Gordon and Balch (1999), [3]: Gordon et al. (2001), [4] Clark, unpublished, [5]: Smyth et al. (2002), [6] Brown and Yoder (1994). PIC: particulate inorganic carbon, POC: particulate organic carbon.

Satellite Data	Geophysical Parameter	Unit	Quality Flag	Region	Method	Ref.
MODIS (MYD23)	PIC	$CaCO_3$ $[moles\ m^{-3}]$	yes	global	merged 2/3-band alg.	[1],[2], [3]
SeaWiFS	coccolith number	N_{cocco}				
MODIS, SeaWiFS	POC	C $[mg\ m^{-3}]$	no	global	empirical	[4]
SeaWiFS	PIC flag	-	yes	England	IOP-model	[3],[5]
CZCS	PIC flag	-	yes	global	supervised multispectr. classif.	[6]

5.2 Bulk IOPs for Coccolithophore Blooms

5.2.1 Parameterization and Sensitivity

All inherent optical properties of the in-water constituents associated with coccolithophore blooms as well as the parameterization used in this study are summarized in Tab. 5.2 on page 73. The setup is chosen as introduced by Balch and Kilpatrick (1996) with modifications by Tyrrell et al. (1999). Considered are four components for absorption and three components for scattering coefficients and phase functions as introduced in 3.1.2.

The coccolithophorid specific bio-optical model is based on definitions in accordance to biogeochemical model definitions:

- the *particulate inorganic carbon concentration* (PIC) derived is the *calcite concentration*, i.e., PIC and $CaCO_3$,
- PIC is associated to the sum over *attached* and *detached* coccolith concentration (Balch and Kilpatrick, 1996),
- the IOPs and the PIC concentration are defined to be solely associated with the *E. huxleyi* phytoplankton species, and
- *E. huxleyi* is defined to describe the phytoplankton functional type class (PFT) *calcifiers* (compare to 2.2.2).

In natural environment, the attached to detached coccolith ratio is varying with the blooming phase. First, the coccoliths are attached to the coccolithophore cells and with time and bloom age most of the platelets get detached. The bio-optical model does not allow for a varying attached to detached coccolith ratio.

Absorption by coccolithophores is neglected as scattering is much larger than absorption:

$$a_{PIC} = 0. \tag{5.3}$$

Scattering is calculated as a function of PIC concentration in $[mg\, m^{-3}]$:

$$b_{PIC} = b^*_{PIC}\ (PIC) \tag{5.4}$$

rather than as a function of the coccolith number or coccolith concentration as realized, e.g., in the algorithm for SeaWiFS data (Gordon et al., 2001). Spectral calcite-specific scattering coefficients b^*_{PIC} are tabulated in Tyrrell et al. (1999) and are based on *in-situ* measurements carried out mainly in the Gulf of Maine [Balch et al. (1991), Balch and Kilpatrick (1996), Tyrrell and Taylor (1996)]. Underlying definitions are: 0.25 pg PIC per coccolith, 30 coccoliths per *E. huxleyi* cell and 1mg PIC = 8.3212E^{-5} mol PIC. It has to be noted, that the number of variable parameters is higher than the bio-optical model reflects as, e.g, the number of coccoliths per coccolithophore cell is variable in a natural environment. Also the attached to detached ratio changes, which can influence the amount of scattering, i.e., the calcite-specific scattering coefficient b^*_{PIC}.

First and foremost, particulate inorganic carbon (PIC) increases scattering in the blue and green spectral region as shown in Fig. 5.1 for different PIC concentrations. The right panel of Fig. 5.1 illustrates a typical scattering budget for a bloom situation and shows the dominance of the PIC contribution to the scattering signal.

Scattering due to all non-calcite particulates is related to total pigment concentration (Ph) given

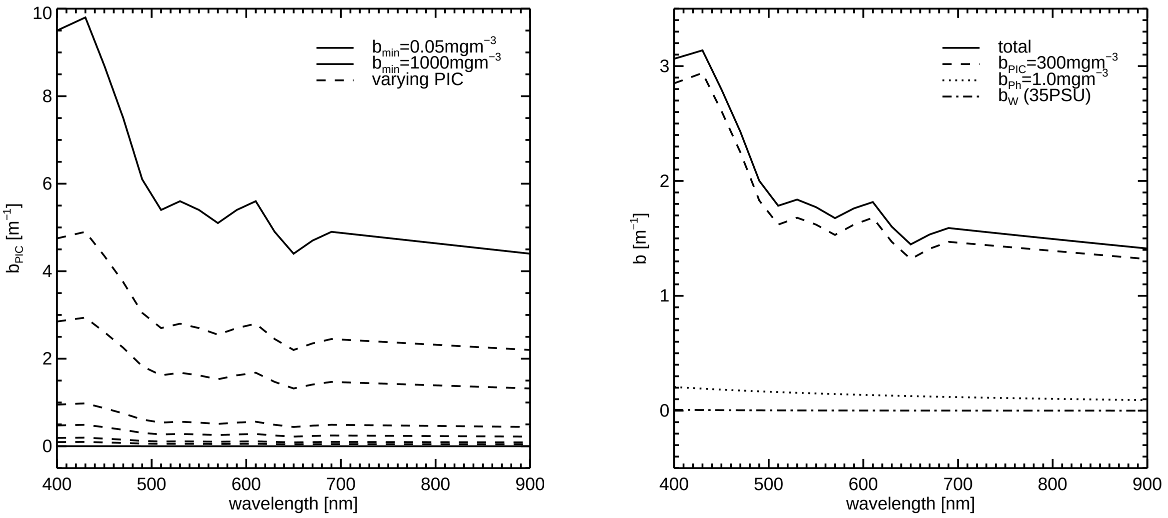

Figure 5.1: Spectral scattering properties of particulate inorganic carbon (PIC) associated with attached and detached coccoliths (left). The scattering budget for a typical coccolithophore bloom concentration (right). PIC parameterization from Tyrrell et al. (1999).

as the chlorophyl-a concentration and is calculated following Gordon and Morel (1983) with an initial coefficient halved to exclude coccolith scattering as defined by Tyrrell et al. (1999).
Phase functions for open ocean conditions dominated by phytoplankton have been parameterized by Zhang et al. (2003). Phase functions for coccolithophores have been measured by Volten et al. (1998), interestingly for *E. huxleyi* species with and without coccoliths. The phase function measurements and extrapolation for the whole angular range is shown in Fig. 5.2.
From absorption and scattering coefficients, single scattering albedo ω_o (Eq. (2.12)) and extinction coefficients c (Eq. (2.10)) are calculated as input parameters for MOMO radiative transfer simulations. The vector of all varying IOPs (for explanation see 3.1.2) for the oceanic bio-optical model including PIC can be written as:

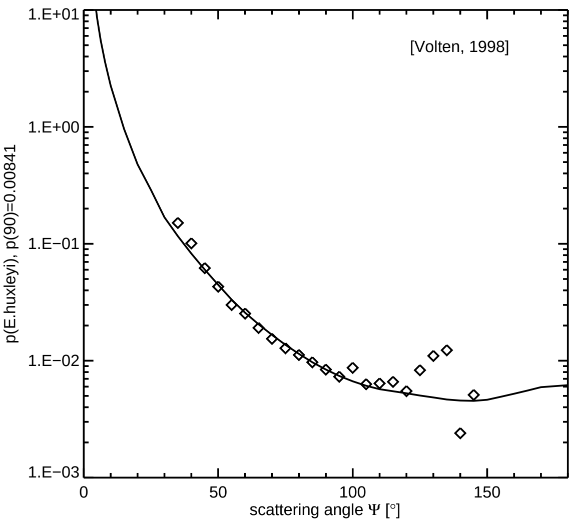

Figure 5.2: Phase function for *E. huxleyi* with coccoliths. Measurements (◇) and best fit by Volten et al. (1998).

$$\begin{aligned} v_{IOP-PIC}(\lambda) &= \{c_{Ph}(Chla,\lambda), \omega_{oPh}(Chla,\lambda), p_{Ph}(\Psi), \\ &\quad a_{YS}(a_{YS}(443),\lambda) \\ &\quad c_{PIC}(PIC,\lambda), \omega_{oPIC}(PIC,\lambda), p_{PIC}(\Psi)\}. \end{aligned} \tag{5.5}$$

Table 5.2: Parameterization of IOPs for in-water constituent during for *coccolithophore* blooms.

Constituent	IOP Parameterization	Reference
Seawater:	$a_W(\lambda)$: directly measured	Pope and Fry (1997). Hale and Querry (1973)
	$b_W(\lambda) = 0.00288(\lambda/500)^{-4.32}$	Morel (1974)
	$p_W(\lambda) = 0.06225(1 + 0.835cos^2\theta)$	Morel (1974)
Ph:	$a_{Ph}(\lambda) = A_{aPh}(\lambda)[Chla]^{B_{aPh}(\lambda)}$	Bricaud et al. (1998)
	$b_{Ph}(\lambda) = A_{bPh}[Chla]^{B_{bPh}}$	Tyrrell et al. (1999), Loisel and Morel (1998)
	$A_{bPh} = 0.15$, $B_{bPh} = 0.635$	
	$p_{Ph}(\Psi) = f([Chla], \Psi)$	Zhang et al. (2003)
PIC:	$a_{PIC}(\lambda) = 0$	Tyrrell et al. (1999)
	$b_{PIC}(\lambda) = b^*_{PIC}(\lambda)\ [PIC]$, $b^*_{PIC}(\lambda)$ tabulated	Tyrrell et al. (1999)
	$p_{PIC}(\Psi)$: directly measured	Volten et al. (1998)
YS:	$a_{YS}(\lambda) = a_{YS}(443)\exp(-(0.014(\lambda - 443)))$	Bricaud et al. (1981)
	$a_{YS}(443) = 0.00348 + 0.5\ a_{Ph}(443)$	Zhang et al. (2003)
concentration range: 0.05<PIC<1000mgm^{-3}, 0.01< $[Chla]$ <10mgm^{-3}		
verical distribution: PIC over first 20m, PIC(depth)=const.		

5.2.2 Concentration Ranges and Dependencies

Absorption of YS is defined to co-vary with phytoplankton. In open oceans, YS is solely a degradation product of phytoplankton rather than from other sources as, e.g., decayed terrestrial vegetation (compare to section 2.2.1). The correlation of YS and $[Chla]$ is described in Zhang et al. (2003) and illustrated in Fig. 5.3.

The distribution ranges of $[Chla]$ and PIC can be seen in Fig. 5.4. Maximum concentrations of chlorophyll-a in the order of 10 mg m^{-3} have been observed. PIC concentration varies between 0.05 and 1000 mg m^{-3}. The correlation between Ph and PIC is unknown, therefore both in-water constituents are taken to vary independently from each other, which also allows high $[Chla]$ while PIC is low.

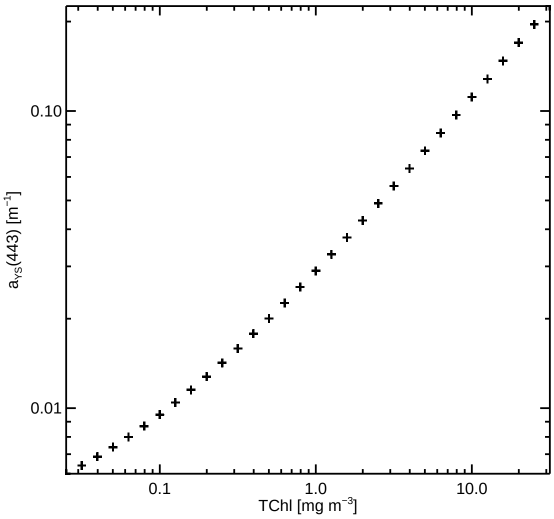

Figure 5.3: Correlation of $[Chla]$ and YS at 443nm utilized within the bio-optical model.

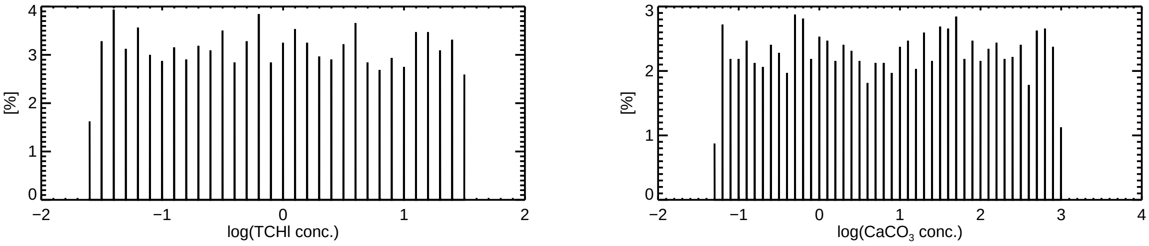

Figure 5.4: Histogram distribution of $[Chla]$ (left) and PIC (right) within the bio-optical model and the synthetic data set.

The change of L_{TOA} and R_{RS} at MERIS spectral band one (412.5 nm) is shown for varying PIC and $[Chla]$ concentrations in Fig. 5.5. Tab. 5.3 summarizes the setup for this sensitivity analysis. The setup is for an atmosphere with a very high aerosol optical thickness. Radiances and reflectance increase with increasing PIC. Highest values occur for high PIC and low $[Chla]$ concentrations. A PIC change from 0 to 400 mg m^{-3} increases the TOA signal at 412.5 nm from about 0.4 to 0.6 $Wm^{-2}sr^{-1}nm^{-1}$, which is an exceptional high signal emerging from sea.

Table 5.3: Setup for the sensitivity study for varying PIC and $[Chla]$ shown in Fig. 5.5.

λ	[TChl]	[PIC]	[YS]	AOT(550)	AM	ws	ps	θ	θ_0	ϕ
412.5nm	*var.*	*var.*	$co-var.$	1.255	8	7.2	1040	0	41	180

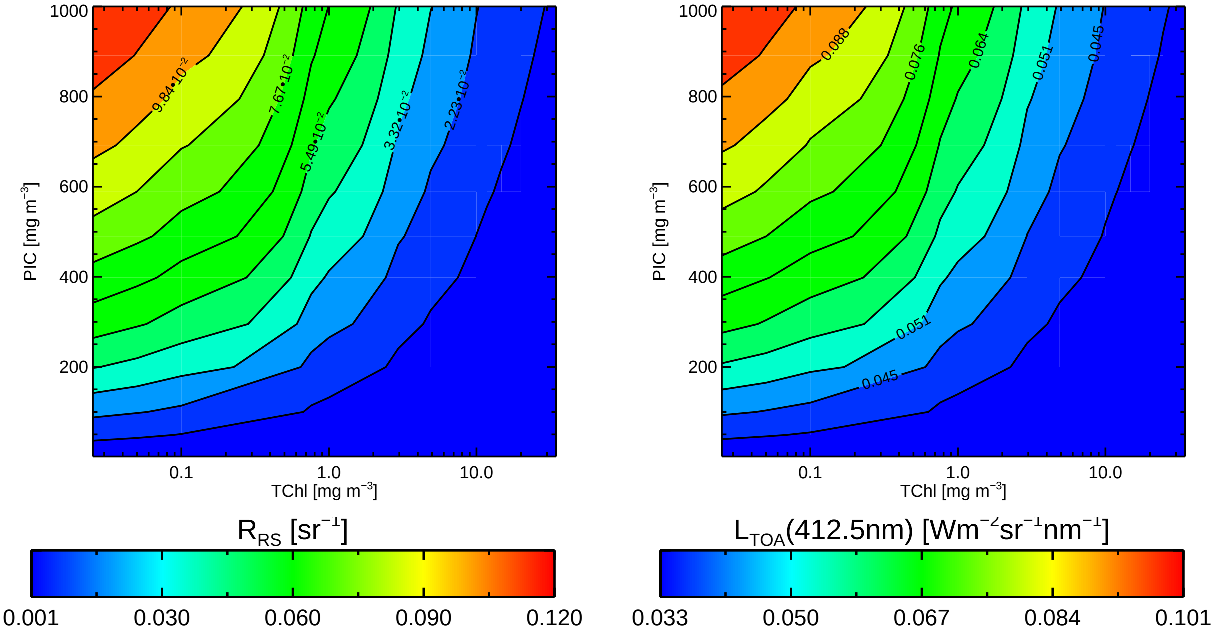

Figure 5.5: R_{RS} (left) and L_{TOA} (right) for MERIS spectral band 1 at 412.5 nm for varying PIC and $[Chla]$ concentrations.

5.2.3 Discussion of the Bio-optical Model for PIC

As noted before, the variability within a coccolithophore bloom is higher than a bio-optical model suitable to calculate macroscopic optical properties as input for radiative transfer calculations can reflect. The model setup is based on realistic assumptions derived from *in-situ* measurements.

For the setup of the bio-optical model for open oceans including marine PIC, a statistics of the inter-correlation between $[Chla]$ and PIC would be desirable. If this co-variation is known, a reasonable retrieval of the pigment concentration [Chla] within a coccolithophore bloom could be possible. Also it would reduce the number of varying parameters of the in-water constituents. A second crucial point is a detailed survey of PIC scattering characteristics. Scattering is increasing lineraly with calcite concentration. Detailed measurements may give information on saturation effects for very high particulate concentrations.

5.3 Algorithm Performance

The performance of the ANN based PIC retrieval algorithm is evaluated by presenting it to an unseen synthetic test dataset as described in section 3.2.2. The derived R_{RS} for eight MERIS spectral bands are compared to implicitely simulated R_{RS}. Fig. 5.6 shows the performance and indicates a succesful inversion regarding to the synthetic test dataset. Second, the retrieved PIC concentrations are compared to a set of unseen PIC concentrations as shown in Fig. 5.7. Limitations can be observed for small PIC concentrations.

Fig. 5.8 shows the functional relationships of the in-water constituent concentrations PIC and $[Chla]$ to R_{RS} of three MERIS spectral bands at 442.5, 510, and 560 nm. These wavelengths are chosen as the ratio of R_{RS} at 442 nm to R_{RS} at 510 and 560 nm, respectively, is unique for PIC. At wavelengths higher than 500 nm a much lower signal appears. Illustrated are the varying remote sensing reflectance in the manner of a look-up-table. The lines with steep slopes are lines of constant $[Chla]$. The lines with a gentle slope are lines of constant PIC concentrations. In Fig. 5.8 the narrow R_{RS} are noticable for high $[Chla]$ and small PIC concentrations. The plots show the ambiguity of the non-linear functional relationships and of the inversion as discussed in 3.2.3. It can be seen, that especially for $[Chla]$ the reflectance information is not unique. Therefore, the pigment concentration is not derived within the blooms from this algorithm.

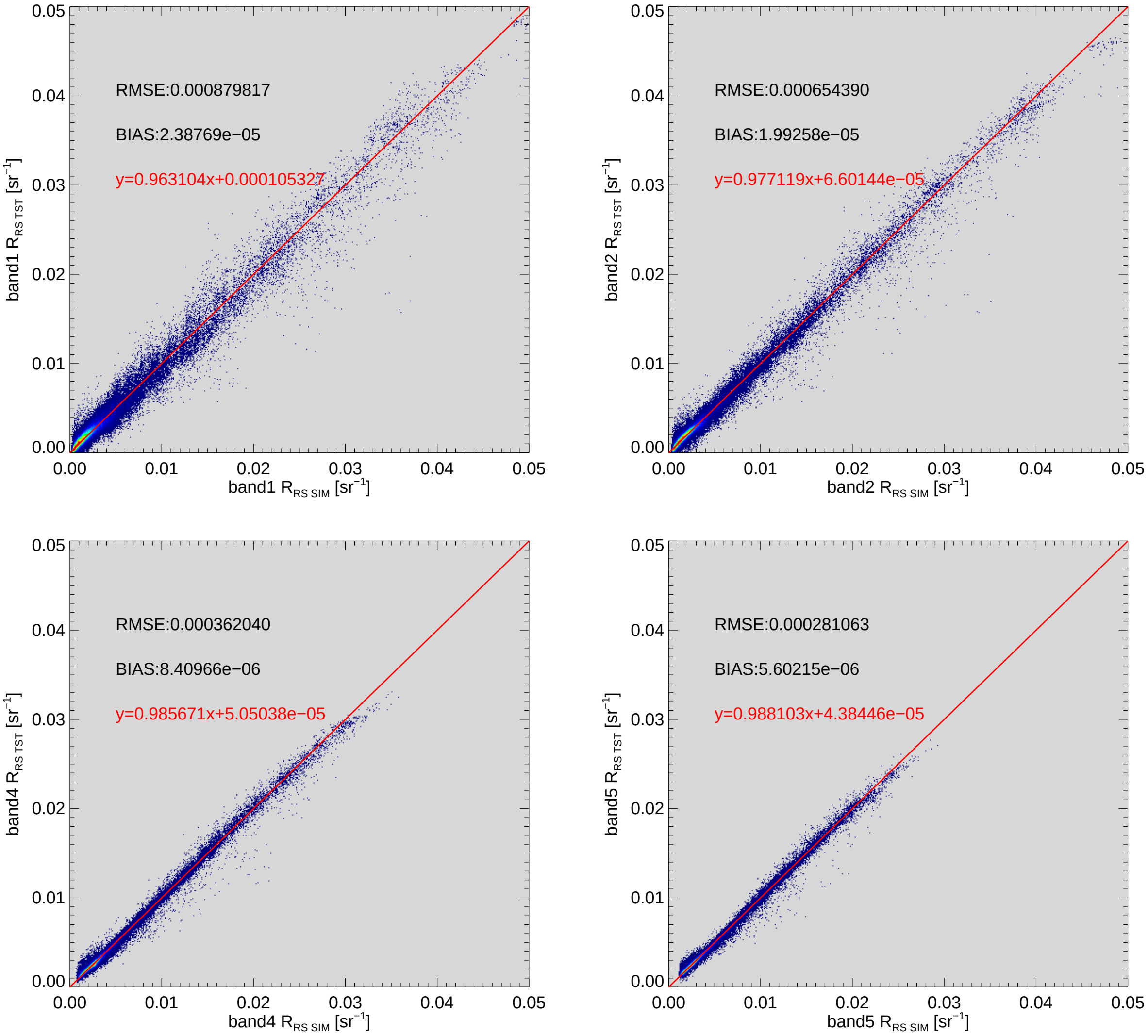

Figure 5.6: Comparison of ANN retrieved R_{RS} against simulated R_{RS} of the test data for MERIS spectral band one, two, four, and five.

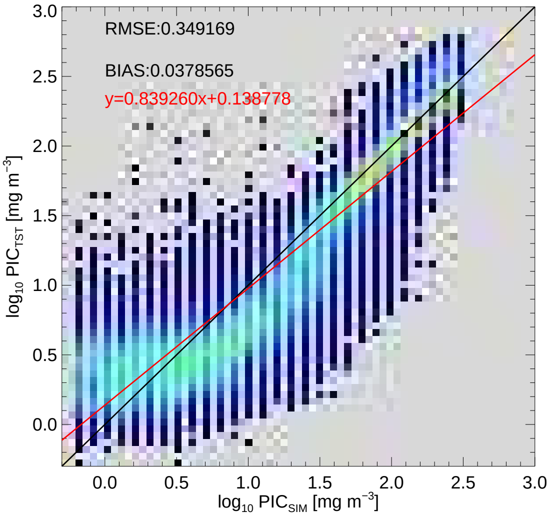

Figure 5.7: Comparison of retrieved and simulated PIC of the test data.

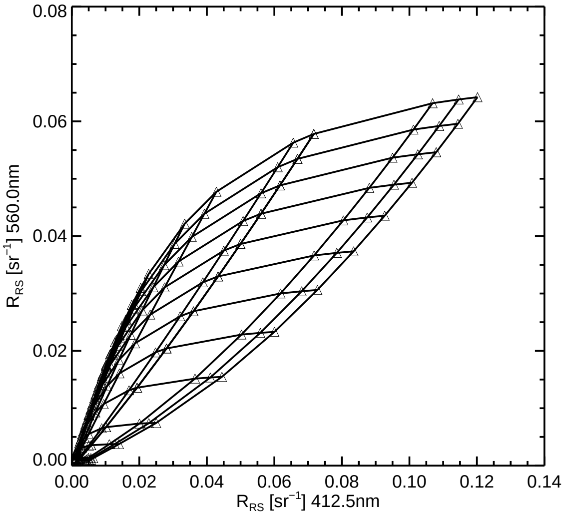

Figure 5.8: Look-up table diagrams for $R_{RS}(412.5\,\mathrm{nm})$ against $R_{RS}(560\,\mathrm{nm})$. $[Chla]$ is constant for lines with steep slopes and is decreasing from high to low R_{RS}. PIC is constant for lines with gentle slopes and is increasing from low to high R_{RS}

5.4 Demonstration of the Algorithm and Comparison

In this section the developed algorithm is applied to MERIS Level-1b measurements. In the following the algorithm is called FUB-PIC. The derived products within one step from MERIS Level-1b TOA measurements are:

- remote-sensing reflectance R_{RS} for eight MERIS spectral bands,
- the calcite concentration PIC, and

- the coccolithophore mask based on threshold values of R_{RS}

R_{RS} and PIC are directly retrieved by applying the two output weighting matrices of the trained ANNs to MERIS Level-1b TOA measurements.

The chosen scene for the demonstration and the comparison is in the North Atlantic. In summer, coccolithophore blooms appear frequently in North Atlantic regions. The derived bio-geophysical products and the coccolithophore mask, are presented here for an illustrative example of a coccolithophore bloom occuring north of Norway in July 2005. The bloom was able to be observed for the whole of July. The example shown is for a nicely cloud free condition on 19th July 2005. The MERIS FUB-PIC product is compared with MODIS-Aqua Level-2 data. MODIS Level-1b and Level-2 products are generated with SEADAS software package version 5.2 from MODIS Level-1A data, which are obtained from *http://oceancolor.gsfc.nasa.gov*. Coccolithophore calcite concentration and coccolithophore quality flags (Level-2 quality flag product, bit set = 11) are determined by a merged 2- and 3-band algorithm proposed by Gordon and Balch (1999) and Balch et al. (2005). The data is stored in the MYD23 product of MODIS-Aqua. The algorithm uses look-up tables based on the scattering properties of the coccolithophores. Input parameters are MODIS-Aqua Level-2 normalized water-leaving radiances at wavelengths 443, 551, and 560 nm.

Time differences between the MODIS-Aqua and MERIS-Envisat overpass for the shown example is 30 minutes. The satellite data used for this comparison are:

- MERIS Level-1b, reduced resolution, 2005-07-19, 09:25UTC and 11:05UTC, orbit numbers 07233 and 07234
- MODIS-Aqua Level-1A data, MYD23 product, 2005-07-19, 09:55UTC, granule 095500

5.4.1 Derived Remote Sensing Reflectance R_{RS}

The upper left panel of Fig. 5.9 shows the RGB composite for the example north of the Norway coast. Clearly visible is the location of the bright coccolithophore bloom in the center of the image. The transect plotted in red indicates the location of the data shown in the other panels of Fig. 5.9. The upper right panel shows the TOA radiance measured for 25 selected points along the transect. It illustrates that no saturation effects occured and demonstrates the variability of the spectral signal over the bloom region. L_{TOA} in the blue spectral range is much higher than for all longer wavelengths. The lower left part of Fig. 5.9 shows the spectral signature measured for radiance reflectance R_W at three wavelengths and the lower right panel illustrates R_W for 25 selected points.

The FUB-PIC alorithm derives R_{RS}, which is converted to R_W by the equation given in Tab. 2.1 for the comparison of FUB-PIC reflectances to ESA-Level-2 relectances. In Fig. 5.10 the comparison is shown for two MERIS spectral bands at 442.5 and 560 nm. The comparison is pixel by pixel. The lower plots in Fig. 5.10 show smaller reflectances for a transect out of the coccolithophore bloom. The upper two panels of Fig. 5.9 are for the transect within the blooming region. Noticable are the differences between both products for the 442.5 nm MERIS spectral band 2. For the 560 nm spectral band the same reflectance values are derived from both algorithms.

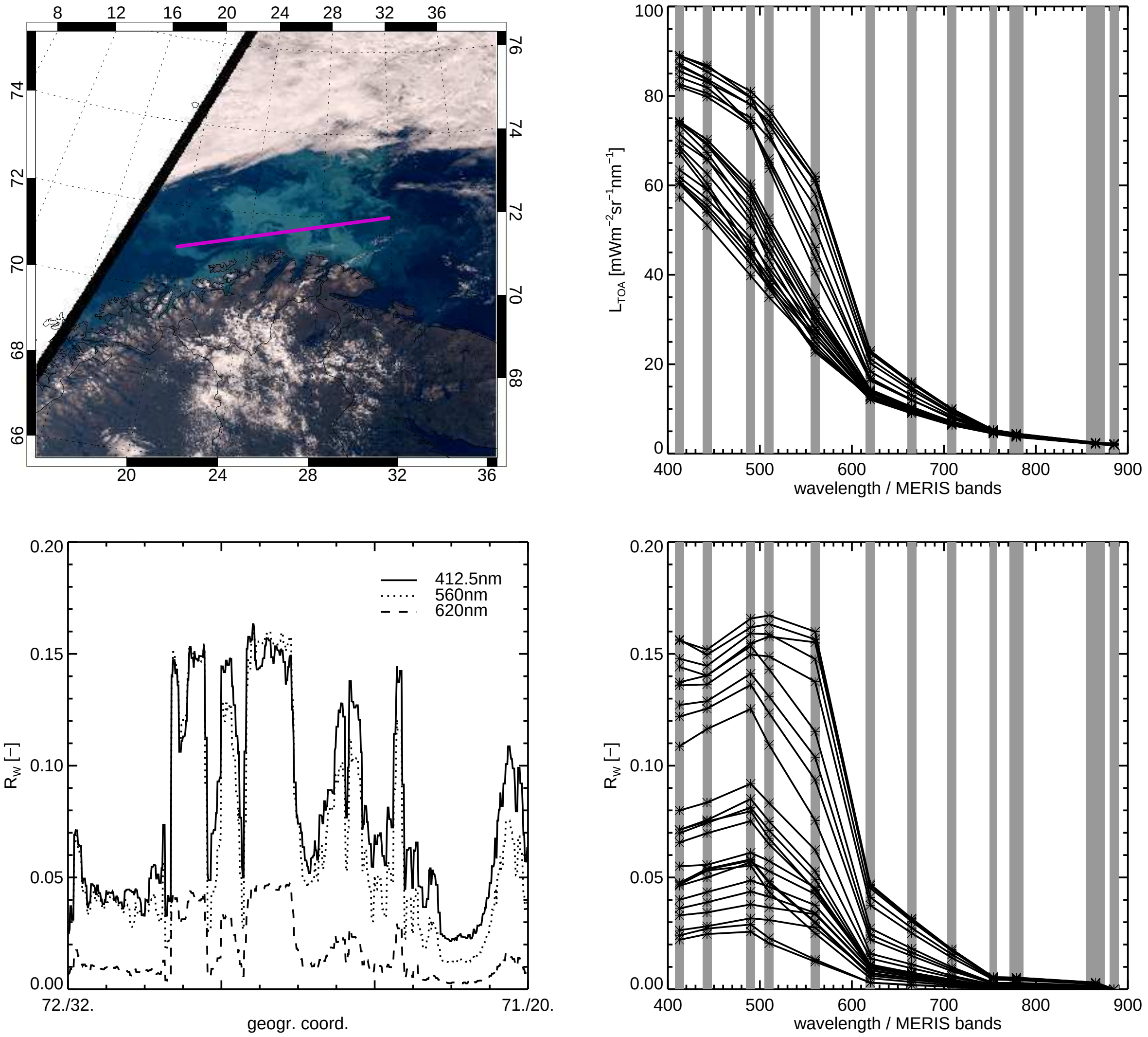

Figure 5.9: Example of L_{TOA} and R_W MERIS measurements. L_{TOA} obtained from MERIS Level-1b data. R_{RS} obtained from FUB-PIC algorithm and converted to R_W to compare to ESA Level-2 product (see Fig. 5.10). Upper left panel FUB-RGB composite of Level-1b data.

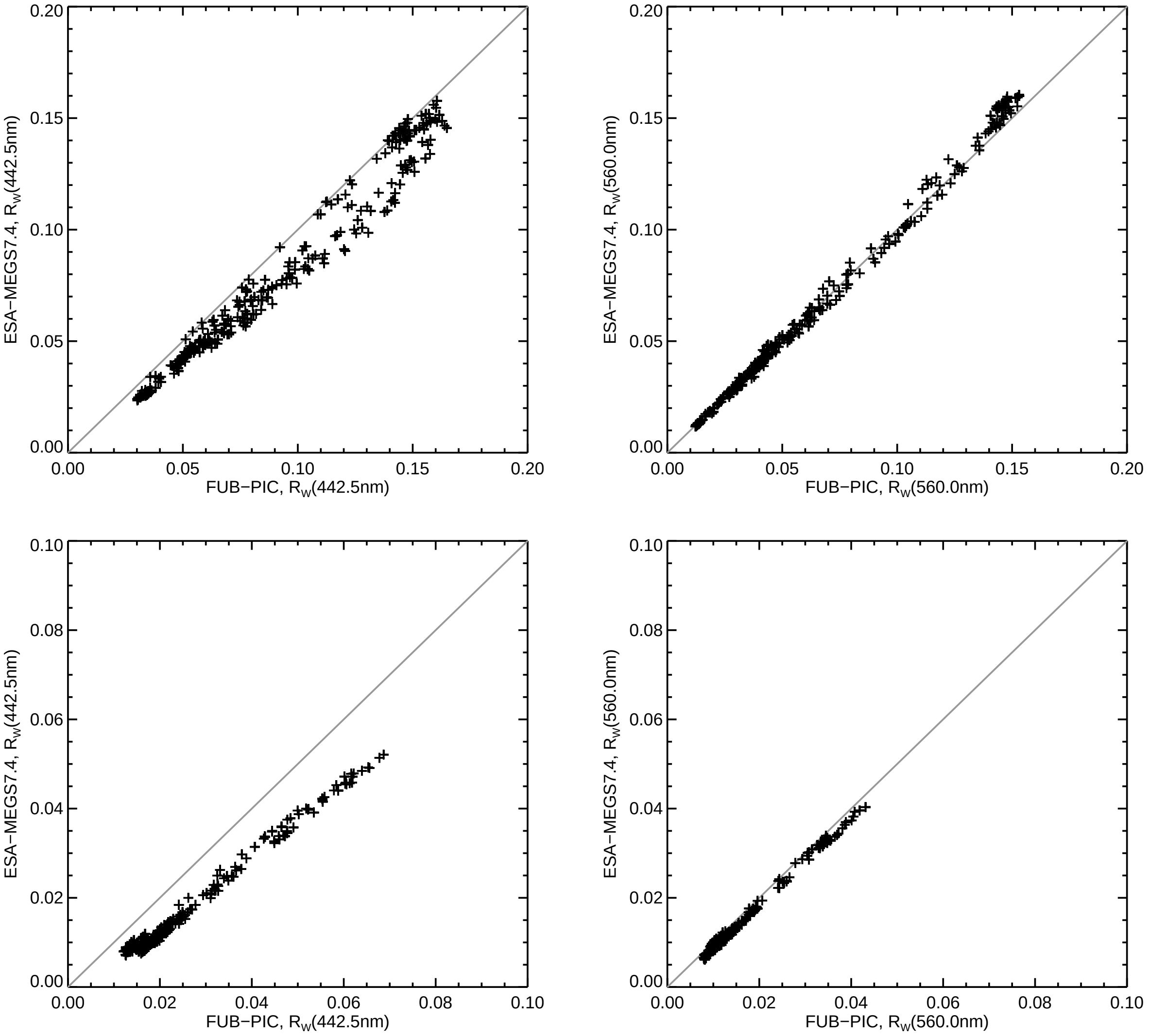

Figure 5.10: Pixel by pixel comparison of radiance reflectance R$_W$ derived with FUB-PIC and ESA-Level-2 MEGS7.4.

5.4.2 Coccolithophore Mask

The informtion used for the coccolithophore bloom mask are R_{RS} derived by the FUB-PIC algorithm at wavelength 442.5nm, 510nm and 560nm, as well as ratios of R_{RS} 442.5 nm/510 nm, 442.5 nm/560 nm and 510 nm/560 nm. Decision boundary values for the coccolithophore flag are derived from the synthetic simulation data as shown in the scatter diagrams in Fig. 5.8. The mask accounts for the specific PIC spectral feature of very high reflectance at 442.5 nm and lower but still increased reflectance at 510 nm and 560 nm. Reflectance values are chosen to correspond with an PIC concentration higher than 100 mg m^{-3}. The values are tabulated in Tab. 5.4.

The FUB-PIC coccolithophore mask has been tested to MERIS scences of sand banks and coral reefs of the Australian Great Barrier Reef to check if the coccolithophore mask is robust against other white ocean signals. Also the mask has been tested over turbid waters like the Baltic Sea during surface accumulation of cyanobacteria phytoplankton. For the processed data these *negative* tests have been succesful.

The mask is set conservative to reduce interactions with the cloud mask. All five criteria defined in Tab. 5.4 have to be full filled. First, the pixels are checked whether they are in a defined reflectance range, then the ratios are calculated.

The comparison of the coccolithophore mask of FUB-PIC and MYD23 (Fig. 5.11) shows an overall good agreement. Also, it can be seen that the conservative setting of the FUB-PIC mask may lead to an under-estimation of the coccolithophore bloom extent compared to the MODIS MYD23 coccolithophore mask. Fig. 5.12 illustrates the influence of the cloud mask within the retrieval scheme. Shown is the same coccolithophore bloom observed by MERIS at 9:25h UTC and 11:05h UTC on 19th of July 2005. Upper plots show the scenes with the cloud mask in white set *cloud* conservative. The lower pictures illustrate the same both scenes with the cloud mask set *cloud free* conservative. In the upper picture the bloom is nearly fully covered by the cloud mask for the second overpass at 11:05h UTC. Extent and intensity is constant for both MERIS overpasses, which is typical for coccolithophore blooms that do not have a diurnal cycle or float in the water column.

Table 5.4: FUB-PIC coccolithophore mask setting.

Parameter	Min	Max	Operator
$R_{RS}442.5nm$	0.022	0.061	AND
$R_{RS}560.0nm$	0.023	0.052	AND
$R_{RS}442.5nm : R_{RS}560.0nm$	0.10	1.20	AND
$R_{RS}442.5nm : R_{RS}510.0nm$	0.90	1.20	AND
$R_{RS}510.0nm : R_{RS}560.0nm$	1.00	1.20	

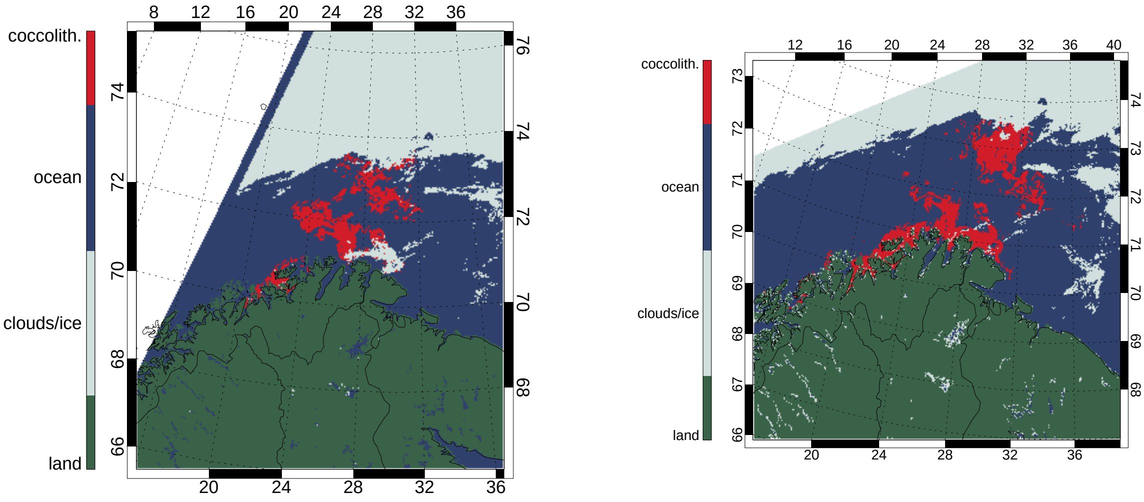

Figure 5.11: Comparison of coccolithophore masks derived by MERIS FUB-PIC (left) and MODIS-Aqua MYD23 (right) for 2005-07-19 at 09:25UTC and 09:55UTC.

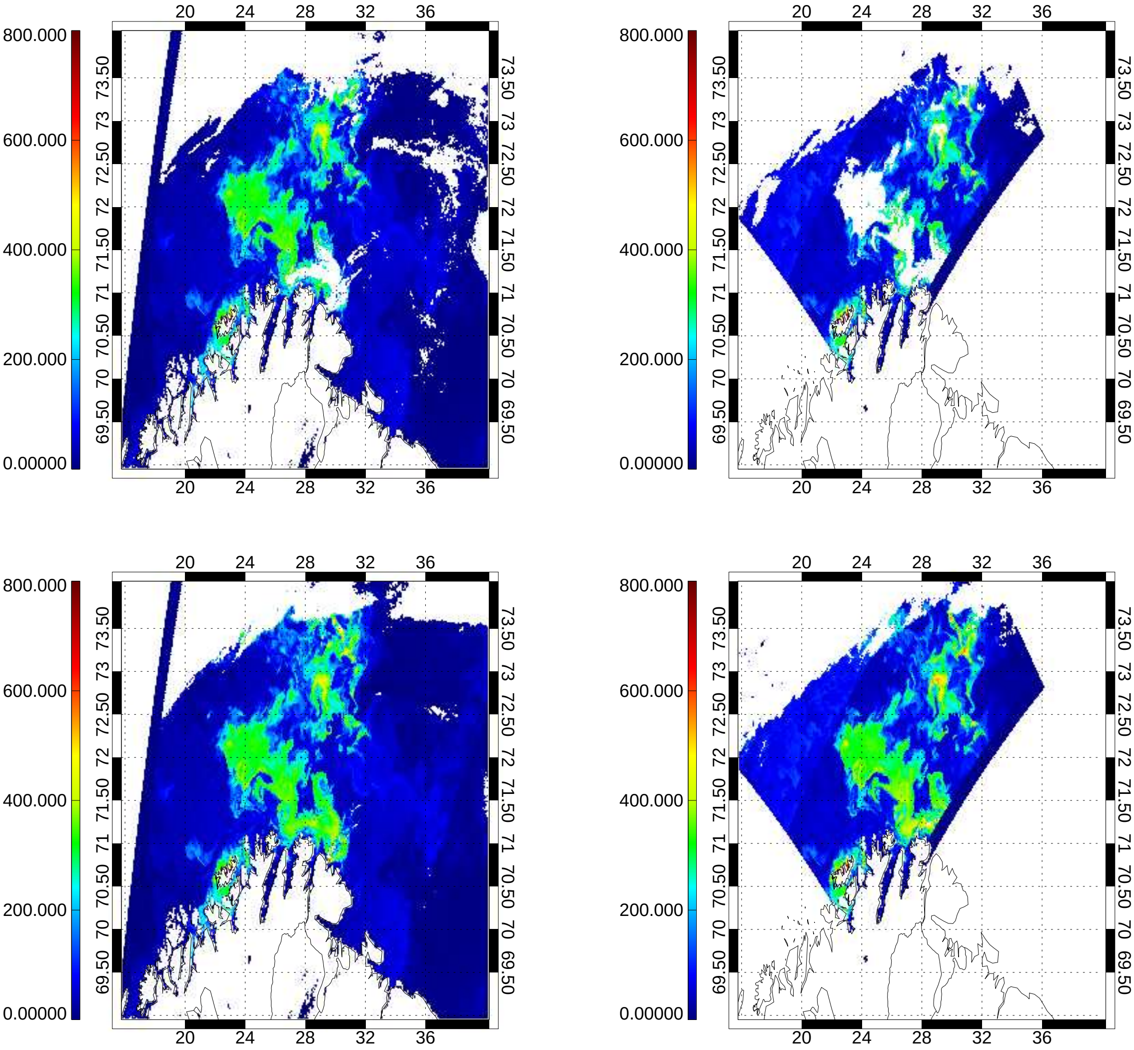

Figure 5.12: Cloud mask and coccolithophore bloom interactions, shown is the PIC concentration derived by MERIS FUB-PIC. Upper panel: cloud masks set *cloudy* conservative. Lower panel: cloud masks set *cloud free* conservative. Day: 2005-07-19, 09:25UTC and 11:05UTC, orbit numbers 07233 and 07234.

5.4.3 Calcite Concentration (PIC)

The MODIS-MYD23 PIC concentration is given in [moles m^{-3}]. Here the data are transfered to units of [mg m^{-3}] using the relationship:

$$1.37\ m^2\ [mol\ PIC]^{-1} \ = \ 1.14 \times 10^{-4}\ m^2\ [mg\ PIC]^{-1}. \tag{5.6}$$

Fig. 5.13 shows the derived PIC concentrations applying the FUB-PIC algorithm to MERIS data and the MYD23 algorithm to MODIS-Aqua data. Fig. 5.14 shows three transects through blooming areas and one transect through an area of low calcite concentration outside the bloom. An overall good agreement for both products can be seen. The PIC signals are correlated for high and small concentrations. However, it is noticable that in average higher PIC concentrations are derived by FUB-PIC for high PIC. This might be caused by a too low atmospheric correction of FUB-PIC. Balch et al. (2005) stated an under-estimation of the MYD23 PIC concentration for high PIC. Since the FUB-PIC and the MODIS-MYD23 algorithms differ in the applied bio-optical model, one possible reason for the variations may also lie in the chosen parameterization. The comparison requires deeper analysis for more test scenes. The validation of the PIC concentration is a major task for later work.

Fig. 5.15 illustrates the derived PIC concentration in form of a FUB-PIC vs. MYD23 scatter plot. It shows that the coccolithophore bloom consists of two main areas, one $\leq 100\,\mathrm{mg\,m^{-3}}$ and a second around 200 to 300 mgm^{-3}. The scatter plot indicates that FUB-PIC results are higher than the MYD23 product for high PIC concentrations.

The statistical error measures $BIAS$, which is the mean deviation and root mean square error $RMSE$ are defined in Eq. (3.17) and Eq. (3.16) and shown in Fig. 5.13. The $BIAS$ is shown for the MERIS FUB-PIC retrieval compared to the MODIS MYD23 product to indicate systematic differences. Additionally, the $RMSE$ gives the magnitude of the variation.

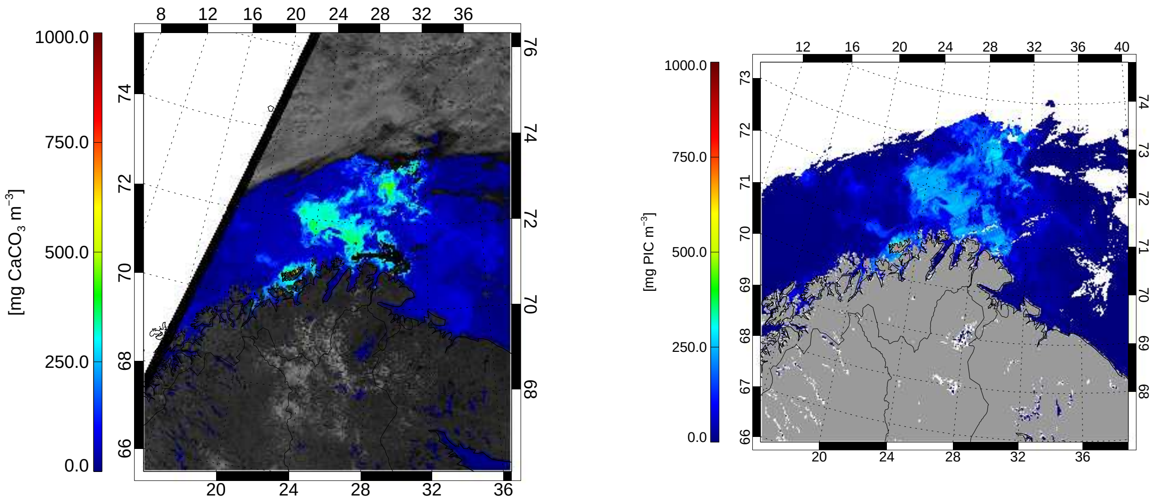

Figure 5.13: PIC comparison FUB-PIC (left) vs. MYD23 (right).

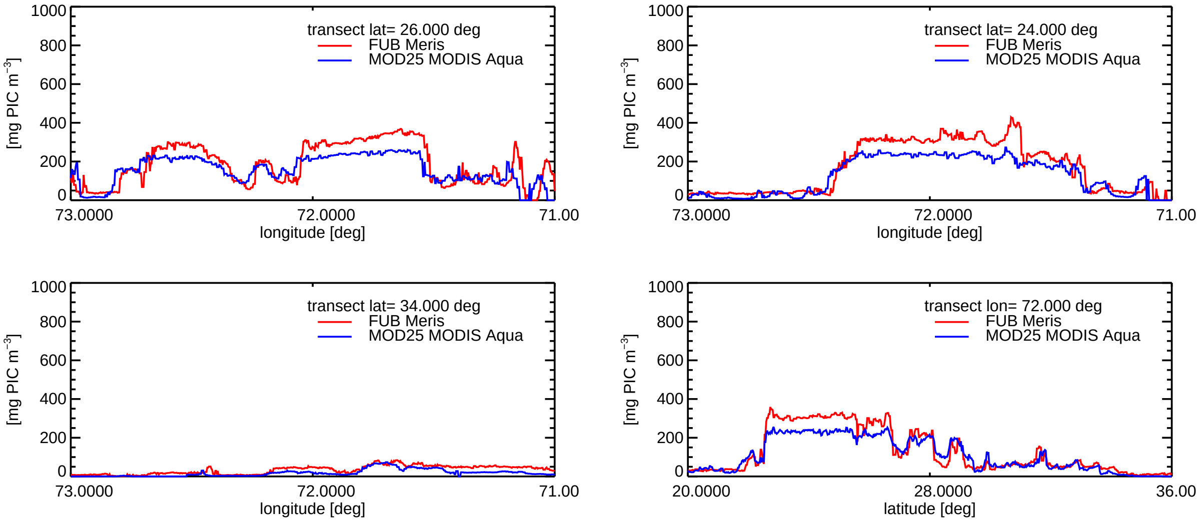

Figure 5.14: Comparison of PIC concentrations derived by MERIS FUB-PIC and MODIS-Aqua MYD23 for 2005-07-19 at 09:25UTC and 09:55UTC.

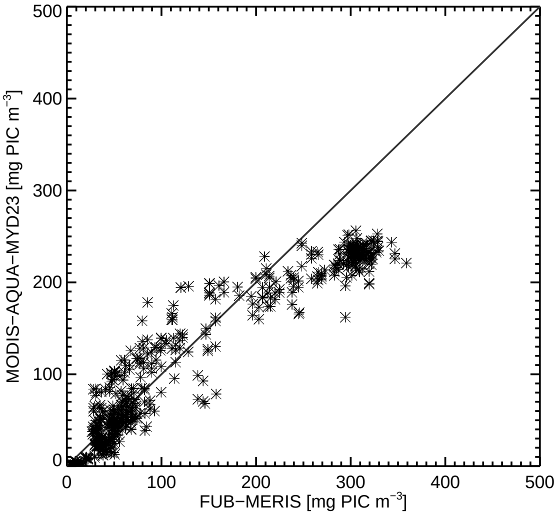

Figure 5.15: Scatter diagram for MERIS FUB-PIC vs. MODIS MYD23 along the transect shown in Fig. 5.9.

5.5 Discussion and Conclusion

Coccolithophores increase water-leaving radiance through their scattering with a maximum in the blue spectral range around 440 to 560 nm. This feature can be recognized top-of-atmosphere by visible radiometers. Numerical simulations performed with the radtiative transfer program MOMO illustrate the sensitivity of the remote-sensing and top-of-atmosphere reflectance for different PIC. The MERIS FUB-PIC algorithm uses measured radiances in 12 spectral bands for the derivation of PIC concentration. Top-of-atmosphere radiances are used as input to allow the consideration of high water-leaving signals for coccolithophore blooming areas.

In a natural environment the ratio of coccolith number to cell number is variable with physiological state of the population, which introduces errors in calcite quantification. The PIC concentration retrieval needs further investigations. Special attention will be given to the assessment of the PIC retrieval outside of the blooming regions.

The coccolithophore bloom mask is developed to be applied globally. In tests the mask was robust against high water signals from coastal waters and white water signals of sand banks and coral reefs. Other in-water compounds producing high back-scattering as, e.g., accumulation of hydrogen sulphide, empty diatom frustules or suspended sediments containing calcareous matter might be misinterpreted as coccolithophores due to similar optical behaviour.

Chapter 6

Summary and Outlook

The **research topic** of this work is a method to study phytoplankton bloom occurences from space using VIS/nIR multispectral satellite radiometry data of medium geometric resolution. For phytoplankton blooms occuring in marine ecosystems an under-sampling has been reported in literature especially regarding a continuous monitoring (Babin et al., 2008). This work made the attempt to investigate in the observational gap from the side of agorithm development of algorithms for satellite sensor applications.

The general importance of investigations in radiation transmission processes lies further in the assessment of the air/sea energy balance and the radiation distribution within the oceans. Radiance distribution determines phytoplankton growth, which is the basic energy source for all live in sea as well it affects the global oxygen and carbon dioxide balance and the oceanic radiation budget.

The satellite data used are calibrated and geo-located top-of-atmosphere radiances of Envisat MERIS Level-1b data. Top-of-atmosphere measurements are prefered to Level-2 atmospherically corrected bottom-of-atmosphere reflectances to allow an atmospheric correction accounting for exceptional water signals particularly caused by phytoplankton blooms. The atmospheric correction is solved implicitly in the retrieval: bottom-of-atmosphere reflectances and in-water constituent concentrations are derived simultaneously.

The retrieval algorithms developed are for phytoplankton blooms of cyanobacteria occuring in the Baltic Sea in summer and phytoplankton blooms of coccolithophores occuring in open oceans. The algorithms are called FUB-Baltic and FUB-PIC, respectively. Compared to the wide variety of phytoplankton blooms, both blooms are exceptional in the marine ecosystem by their dominance, extension, and frequency. Both blooms are occuring regularly and they appear as mono-specific blooms with one or two dominating phytoplankton species.

The **method** applied is based on radiative transfer forward simulations with the Matrix Operator Model MOMO, which is specially capable for calculations in optical dense media. The inversion scheme is based on an Artificial Neural Network technique, which is a method well suited for multi-spectral remote sensing because of its fast application to satellite data.

Results of this work are summarized, first for the analyzation of the bio-optical models, and second for the retrieval algorithms. With the help of radiative transfer forward simulations the sensitivity of top-of-atmosphere and bottom-of-atmosphere radiance fields have been analyzed for the variable parameters of the specific bio-optical setups for the two phytoplankton blooms under investigation. The sensitivity is presented for MERIS spectral bands. The major influence of the parameterization of absorption and scattering properties are comprised in the following.

- The spectral absorption of yellow substances in the oceans is characterized by an exponential curve with a slope varying between regions. The yellow substance absorption is normalized to 443 nm. The steeper the slope the higher is the absorption in the wavelength shorter than 443 nm so that the radiance field is decreasing with increasing slope. For wavelength longer than 443 nm, the radiance field is increasing with increasing slope as absorption is decreasing. The slope value has an increasing influence on the radiance field with increasing absorption. The specific slope values have to be accounted for in the bio-optical water models.

- The influence of decreasing specific absorption coefficients with increasing phytoplankton concentrations is crucial to consider in the water model. This is especially crucial for high phytoplankton concentrations during bloom occurences. Neglecting the variability of the specific absorption can cause a tenfold under-estimation of phytoplankton absorption and therefore an over-estimation of phytoplankton concentration.

- Remote sensing observations in nadir geometry can not resolve vertical information and the derived concentrations are depth-integrated as it is assumed they are homogenously distributed. If in-water constituents occur statified in the water column, their stratification affects the water-leaving signal. The influence is shown to increase with decreasing depth of the concentration maximum. The effect is explained with the decreasing influence of water absorption when concentrations are closer to the sea surface.

- The scattering signal of calareous coccolithophorids is highest in the blue spectral range below 510 nm. For maximum calcite concentrations scattering is increasing of about 4 m^{-1} around 420 nm. Even if the atmospheric influence is high, the exceptional water signal is detectable at top-of-atmosphere.

Restrictions appear due to ambiguous radiant quantities emerging from different optical properties and the additive nature of the bulk optical properties absorption and scattering. Also, the phytoplankton blooms occur under a much more diverse set of natural conditions than the bio-optical models and the macroscopic optical properties they describe can reflect. One example for the higher natural variability is the cyanobacteria floating within the water column.
The results comprise following bio-geophysical products derived from MERIS Level-1b data applying the FUB-Baltic algorithm:

- remote sensing reflectance at eight MERIS spectral bands,

- yellow substance absorption at 443 nm, total suspended matter concentration, and chlorophyll-a concentration for the Baltic Sea,

- the cyanobacterial bloom mask for the Baltic Sea, which is based on high reflectance at 560 nm caused by the surface accumulation by cyanobacterias. The mask uses retrieved remote sensing reflectance threshold values and reflectance ratio thresholds. The bloom mask is set cyanobacteria free conservative.

The bio-geophysical parameters derived by the FUB-PIC algorithm are:

- remote sensing reflectances at eight MERIS spectral bands,
- particulate inorganic carbon concentration in open oceans,
- the coccolithophore bloom mask for open oceans based on thresholds for retrieved remote sensing reflectances and reflectance ratios. The bloom mask accounts for the difference in reflectance at 442.5 nm and 560 nm caused by calcite scattering. The mask is set bloom free conservative and a cloud free conservative cloud mask has to be applied to avoid an under-sampling of coccolithophore blooms.

Major remaining objective is a more detailed validation when suitable *in-situ* data are available. For blooming regions with high concentrations it is difficult to collect these data.

Outlook: Phytoplankton blooms are feedback markers for water quality, ecosystem, and climate change. Studies have to include the assessment of bloom timing and magnitude, the seasonal and inter-annual variations, and the productivity of the blooms (Robinson, 2008). Continuous, long-term Earth observational measurements are an essential data source to allow the recognition of exceptional phytoplankton blooms. Using spaceborne data is the only continuous observational method to detect the extent of the blooms. Therefore, algorithms are needed that sufficiently consider the variability of water inherent optical properties during bloom occurences. For this purpose it would be worth to investigate in a complete information content study including the ambiguity of the total bulk optical properties.

The Sentinel-3 mission of the European Space Agency with the OLCI instrument for land and ocean remote sensing onboard will allow for an on-going observation of the phytoplankton blooms using the developed algorithms.

A high potential of improving remote sensing techniques lies in the synergetic use of multi-sensor data like the combined use of sea surface temperature, e.g., derived from AATSR measurements, or very high resolution data of hyperspectral instruments, e.g., SCIAMACHY. Both instruments are onboard Envisat. Optical studies including sea surface temperature anomalies will support the understanding of ecosystem dynamics. SCIAMACHY and also the GFZ/DLR airborne hyperspectral imager EnMAP can expand multi-sensor research and investigations in ocean signals at hyperspectral resolution.

The use of bio-optical information within oceanic ecosystem models offers the possibility of interdisciplinary investigations in oceanography. Research on algal blooms in marine ecosystem dynamics as well as climate change related and and socio-economic impact studies are strongly demanded by global projects like the UNESCO program on *Global Ecology and Oceanography of Harmful Algal Blooms*.

Acronyms, Symbols and Indizes

Acronyms

Acronym	Denotation
6SV1	Second Simulation of a Satellite Signal in the Solar Spectrum, Vector, version 1
ANN	Artificial Neural Network
AOPs	Apparent Optical Properties
AVHRR	Advanced Very High Resolution Radiometer
BOA	bottom-of-atmosphere
BPA	bleached particles absorption
CCD	Charge Coupled Device
CDOM	colored or chromophoric dissolved organic matter
DOAS	Differential Optical Absorption Spectroscopy
DMS	dimethylsulfid
CZCS	Coastal Zone Color Scanner
ECMWF	European Centre for Medium-Range Weather Forecasts
ENVISAT	ENVIronmental SATellite
EOS	Earth Observation System
ESA	European Space Agency
ESF	European Science Foundation
FIMR	Finish Institute of Marine Research
FR	Full Resolution
FUB	Freie Universität Berlin

Acronym	Denotation
H_2O	water, water vapor
HAB	Harmful Algae Bloom
HELCOM	Helsinki Commission
IAPSO	International Association of Phyical Science of the Ocean
IEEE	Institute of Electrical and Electronics Engineers
IFOV	Instantaneous Field of View
IOCCG	International Ocean Colour Coordinating Group
IOPs	Inherent Optical Properties
IR	Infrared
MCC++	Monte Carlo Method in C++
MERCI	Meris catalogue and inventory
MERIS	MEdium Resolution Imaging Spectrometer
MOBY	Marine Optical Buoy System
MODIS	Moderate Resolution Imaging Spectroradiometer
MOMO	Matrix Operator MOdel
MS	multiple scattering
NASA	National Aeronautics and Space Administration
nIR	near Infrared
NAD	nadir
NAP	non-algal particles, non-living organic and inorganic particles
NOAA	National Oceanic and Atmospheric Administration (U.S.)
O_2	oxygen
O_3	ozone
OSOA	Ordres Successifs Ocean Atmosphere
OSS	organic suspended solids
RE	relative error
Ph	phytoplankton, living organic particles
PIC	particulate inorganic carbon
POC	particulate organic carbon

Acronym	Denotation
RGB	Red Green Blue
RMSE	root mean square error
POC	particulate organic carbon
RR	reduced resolution
RT	radiative transfer
RTE	Radiative Transfer Equation
SCIAMACHY	Scanning Imaging Absorption Spectrometer for Atmospheric Cartography
SeaWiFS	Sea-viewing Wide Field-of-view Sensor
sed	sediments
SNR	signal to noise ratio
SS	single scattering
TIR	thermal Infrared
TOA	top-of-atmosphere
TS	total scattering
TSM	total suspended matter
UV	ultraviolet
VIS	visible
VSF	volume scattering function
W	pure seawater
WFD	European Union Water Framework Directive
YS	yellow substance, gelbstoff, gilvin, CDOM
YSBPA	yellow substance and bleached particles absorption

Symbols and Indizes

Symbol, Index	Unit	Denotation
a	[m^{-1}]	total absorption coefficient
A	[m^2]	area
b	[m^{-1}]	total scattering coefficient
b_b, b_f	[m^{-1}]	back- and forward scattering coefficient
β	[m^{-1}sr^{-1}]	volume scattering function (VSF)
c	[m^{-1}]	beam attenuation, i.e. extinction coefficient
$[Chla]$	[mgm^{-3}]	chlorophyll-a concentration
D	[m]	diameter of the sphere
E	[Wm^{-2}nm^{-1}]	plane irradiance
E_0	[Wm^{-2}nm^{-1}]	solar irradiance
E_d	[Wm^{-2}nm^{-1}]	downwelling irradiance
E_u	[Wm^{-2}nm^{-1}]	upwelling irradiance
E_o	[Wm^{-2}nm^{-1}]	scalar irradiance
Err	$[-]$	error function
γ	[m^{-1}]	bulk IOP coefficient
J	$[-]$	source function
k_r	$[-]$	imaginary part of the refractive index
k_d	$[m^{-1}]$	diffuse attenuation coefficient for downward irradiance
L	Wm^{-2}sr^{-1}nm^{-1}	radiance, intensity
L_W	$[W\,m^{-2}\,sr^{-1}]$	water-leaving radiance
L_{WN}	$[W\,m^{-2}\,sr^{-1}]$	normalized water-leaving radiance
λ	nm	wavelength, denoting spectral dependancy

Symbol, Index	Unit	Denotation
m_r	$[-]$	complex index of refraction
n	$[-]$	number density
n_D	$[-]$	size distribution of the particles
n_r	$[-]$	real part of refractive index
N_2	$[-]$	nitrogen
ω_o	$[-]$	single-scattering albedo
p		scattering phase function
ϕ	[sr]	azimuth angle
Ψ	[sr]	scattering angle
Q	$[-]$	efficiency
Q_a	$[-]$	efficiency factor for absorption
Q_b	$[-]$	efficiency factor for scattering
R	$[-]$	irradiance reflectance, irradiance ratio
R_{RS}	$[sr^{-1}]$	remote-sensing reflectance
R_W	$[-]$	radiance reflectance
R_{WN}	$[-]$	normalized water-leaving reflectance
sig	$[-]$	sigmoidal function
σ	$[\mathrm{m}^2]$	cross section
σ_a	$[\mathrm{m}^2]$	total absorption cross section
σ_b	$[\mathrm{m}^2]$	total scattering cross section
σ^2	$[-]$	variance
$\sigma_a^* = a^*$	$[m^2\mathrm{mg}^{-1}]$, $[m^2\mathrm{mol}^{-1}]$	specific absorption coefficient

Symbol, Index	Unit	Denotation
T	$[-]$	transmission
T	°C	temperature
$[TChl]$	$[\mathrm{mgm}^{-3}]$	total chlorophyll concentration, sum of chlorophyll-a and phycoerythrin concentration
$_{total}$	$[-]$	denoting the sum over all x
τ	$[-]$	optical depth, optical thickness
θ	[sr]	zenith angle or observer zenith angle
θ_0	[sr]	sun zenith angle
V	$[\mathrm{m}^3]$	volume
W	$[-]$	weight matrix
x	$[-]$	denoting varying groups of in-water constituents
z	[m]	geometric depth

Bibliography

S. G. Ackleson, W. M. Balch, and P. M. Holligan. Response of water-leaving radiance to particulate calcite and chlorophyll-a concentrations: a modelfor Gulf of Maine coccolithophore blooms. *J. Geophys. Res.*, 99:7483–7499, 1994.

S. Alvain, C. Moulin, Y. Dandonneau, and F. Bréon. Remote sensing of phytoplankton groups in case 1 waters from global seawifs imagery. *Deep Sea Research Part I: Oceanographic Research Papers*, 52 (11):1989–2004, 2005.

D. Anderson, A. Cembella, and H. G.M. *Physiological Ecology of Harmful Algae Blooms*, volume G 41 of *NATO ASI Series*. Springer verlag berlin, heidelberg edition, 1989.

D. M. Anderson, Y. Kaoru, and A. W. White. Estimated annual economic impacts from harmful algal blooms (habs) in the united states. Technical Report WHOI-2000-11, Woods Hole Oceanographic Institute, Sept. 2000.

D. M. Anderson, P. M. Glibert, and J. M. Burkholder. Harmful algal blooms and eutrophication: Nutrient sources, composition, and consequences. *Estuaries*, 25(4):704726, 2002.

G. Anderson, S. Clough, F. Kneizys, J. Chetwynd, and E. Shettle. Afgl atmospheric constituent profiles (0120 km). Technical Report AFGL-TR-86-0110., Air Forces Geophysics Laboratory, 1986.

S. Andréfouët, M. J. Costello, M. Rast, and S. Sathyendranath. Earth observations for marine and coastal biodiversity and ecosystems special issue. *Remote Sensing of Environment*, 112(8):3297–3299, August 2008.

D. Antoine. *Guide to the creation and use of ocean-colour, Level-3, binned data products.* Number 4. IOCCG Report, 2004.

D. Antoine and A. Morel. Atmospheric correction over the ocean (Case 1 waters). ESA Dokument ATBD 2.7, Doc. No.: PO-TN-MEL-GS-0005, Laboratoire de Physique et Chimie Marines, 2000.

M. Babin. Coastal surveillance through observation of ocean colour (COASTLOOC). Final report, Laboratoire de Physique et Chimie Marines, Villefranche-sur-mer, France, 2000.

M. Babin, A. Morel, and B. Gentili. Remote sensing of sea surface sun-induced chlorophyll fluorescence: consequences of natural variations in the optical characteristics of phytoplankton and the quantum yield of chlorophyll a fluorescence. *International Journal of Remote Sensing*, 17:2417–2448, 1996.

M. Babin, A. Morel, V. Fournier-Sicre, F. Fell, and D. D. Stramski. Light scattering properties of marine particles in coastal and oceanic waters as related to the particle mass concentration. *Limnol. and Oceanogr.*, 48:843–859, 2003.

M. Babin, D. Stramski, G. Ferrari, H. Claustre, A. Bricaud, G. Obolensky, and N. Hoepffner. Variations in the light absorption coefficients of phytoplankton, non-algal particles, and dissolved organic matter in coastal waters around europe. *J. Geophys. Res.*, page 10.1029, 2003. 2001JC000882.

M. Babin, J. Cullen, C. Roesler, P. Donaghay, G. Doucette, M. Kahru, M. Lewis, C. Scholin, M. Sieracki, and H. Sosik. New approaches and technologies for observing harmful algal blooms. *Oceanogr. Mag.*, 18(2):210–227, 2005.

M. Babin, C. Roesler, and J. Cullen. *Real-time Coastal Observing Systems for Marine Ecosystem Dynamics and Harmful Algal Blooms: Theory, Instrumentation and Modeling.* Oceanographic Methodology series. UNESCO Publishing, 2008.

S. M. Babin, J. A. Carton, T. D. Dickey, and J. D. Wiggert. Satellite evidence of hurricane-induced phytoplankton blooms in an oceanic desert. *Journal of Geophysical Research (Oceans)*, 109:CiteID C03043, Mar. 2004. doi: 10.1029/2003JC001938.

W. M. Balch and K. A. Kilpatrick. Calcification rates in the equatorial pacific along 140w. *Deep-Sea Research II*, 43:971–993, 1996.

W. M. Balch, P. M. Holligan, S. G. Ackleson, and K. Voss. Biological and optical properties of mesoscale coccolithophore blooms in the gulf of maine. *Limnol. Oceanogr*, 36:629–643, 1991. URL `http://www.tpdsci.com/Ref/Balch_WM.php`.

W. M. Balch, H. R. Gordon, B. C. Bowler, D. T. Drapeau, and E. S. Booth. Calcium carbonate measurements in the surface global ocean based on moderate-resolution imaging spectroradiometer data. *J. Geophys. Res.*, 110:21, July 2005. doi: 10.1029/2004JC002560.

V. Barale and M. Gade. *Remote Sensing of the European Seas.* Springer Netherlands, 2008. URL `http://www.springer.com/earth+sciences/book/978-1-4020-6771-6`.

J. S. Bartlett, K. J. Voss, S. Sathyendranath, and A. Vodacek. Raman scattering by pure water and seawater. *Appl. Optics, Vol.*, 37(15):3324–3332, 1998. doi: 10.1364/AO.37.003324.

J.-L. Bézy, S. Delwart, and M. Rast. MERIS - A New Generation of Ocean-Colour Sensor onboard Envisat. *ESA Bulletin*, 103:48–56, 2000.

T. S. Bianchi, E. Engelhaupt, P. Westman, T. Andren, C. Rolff, and R. Elmgren. Cyanobacterial blooms in the baltic sea: Natural or human-induced? *Limnology and Oceanography*, 45(3):716–726, May 2000.

U. Boettger, R. Preusker, and N. J. Radiative transfer model storm for full stokes vector calculations for a plane parallel atmosphere-surface-system. *Remote Sensing of Clouds and the Atmosphere SPIE*, 5979, 2005.

C. F. Bohren and D. R. Huffman. *Absorption and Scattering of Light by Small Particles.* Wiley VCH, 1983.

A. Bracher, M. Vountas, T. Dinter, J. P. Burrows, R. Röttgers, and I. Peeken. Quantitative observation of cyanobacteria and diatoms from space using phytodoas on sciamachy data. *Biogeosciences Discuss.*, 5:4559–4590, 2008.

A. Bricaud, A. Morel, and L. Prieur. Absorption by dissolved organic matter in the sea (yellow substance) in the UV and visible domains. *Limnol. Oceanogr.*, 26:43–53, 1981.

A. Bricaud, M. Babin, A. Morel, and H. Claustre. Variability in the chlorophyll-specific absorption coefficients of natural phytoplankton: Analysis and parameterization. *J. Geophys. Res.*, 100:13321–1332, 1995.

A. Bricaud, A. Morel, M. Babin, K. Allali, and H. Claustre. Variations of light absorption by suspended particles with chlorophyll-a concentration inoceanic (case 1) waters: Analysis and implications for bio-optical models. *J. Geophys. Res.*, 103:31033–31044, 1998.

W. S. Broecker and T.-H. Peng. *Tracers in the Sea*, page 660. Lamont-Doherty Geol. Obs., Columbia University, 1982.

C. W. Brown and J. A. Yoder. Coccolithophorid blooms in the global ocean. *J. Geophys. Res.*, 99(C4): 7467–7482, 1994.

B. Bulgarelli, V. B. Kisselev, and L. Roberti . Radiative transfer in the atmosphere-ocean system: The finite-element method. *Applied Optics*, 38(9):1530–1542, 1999. doi: 10.1364/AO.38.001530. URL `http://www.opticsinfobase.org/ao/abstract.cfm?uri=ao-38-9-1530`.

A. H. Callaghan, G. Leeuw, L. Cohen, and C. D. O'Dowd. Relationship of oceanic whitecap coverage to wind speed and wind history. *Geophys. Res. Lett.*, 35:23609+, 2008. doi: 10.1029/2008GL036165.

M. Chami. Importance of the polarization in the retrieval of oceanic constituents from the remote sensing reflectance. *Journal of Geophysical Research*, 112:C05026+, 2007. doi: 10.1029/2006JC003843.

B. Chen and J. J. Stamnes. Scattering by simple and nonsimple shapes by the combined method of ray tracing and diffraction: Application to circular cylinders. *Appl. Opt.*, 37:1999–2010, 1998.

C. Cox and W. Munk. Measurements of the roughness of the sea surface from photographs of the sun's glitter. *J. Opt. Soc. Am.*, 44(11):838 – 850, 1954.

J. J. Cullen, A. M. Ciotti, R. F. Davis, and M. R. Lewis. Optical detection and assessment of algal blooms. *Limnol. Oceanogr*, 42(5):1223–1239, 1997.

M. Darecki and D. Stramski. An evaluation of modis and seawifs bio-optical algorithms in the baltic sea. *Remote Sens. Environ.*, 89(3):326350, February 2004. doi: 10.1016/j.rse.2003.10.012.

M. Darecki, A. Weeks, S. Sagan, P. Kowalczuk, and S. Kaczmarek. Optical characteristics of two contrasting case 2 waters and their influence on remote sensing algorithms. *Continental Shelf Res.*, 23 (3-4):237–250, 2003.

M. Darecki, S. Kaczmarek, and J. Olszewski. Seawifs ocean colour chlorophyll algorithms for the southern baltic sea. *Intl. J. Rem. Sens.*, 26(2):247 – 260, January 2005. doi: 10.1080/01431160410001720298.

M. Defoin-Platel and M. Chami. How ambiguous is the inverse problem of ocean color in coastal waters? *J. Geophys. Res.*, 112(C03004), 2007. doi: 10.1029/2006JC003847.

R. J. Diaz and R. Rosenberg. Spreading dead zones and consequences for marine ecosystems. *Science*, 321(5891):926 – 929, August 2008. doi: 10.1126/science.1156401.

R. Doerffer. Protocols for Validation of MERIS Water Products. Internes ESA Dokument Doc. No.: PO-TN-MEL-GS-0043, GKSS, 2002.

R. Doerffer and J. Fischer. Concentration of chlorophyll, suspended matter and Gelbstoff in case-II waters derived from CZCS satellite data with inverse modelling methods. *J. Geophys. Res.*, 99:7457–7466, 1994.

P. G. Falkowski, R. T. Barber, and V. Smetacek. Biogeochemical controls and feedbacks on ocean primary production. *Science*, 281(5374):200 – 206, 1998. doi: 10.1126/science.281.5374.200.

M. J. R. Fasham. *Ocean Biogeochemistry: The Role of the Ocean Carbon Cycle in Global Change.* Springer, Berlin, 2003.

F. Fell. Validierung eines Modells zur Simulation des Strahlungstransportes in Atmosphäre und Ozean. Strahlung in Atmosphäre und Ozean, Beiträge zur Fernerkundung 7, Institut für Weltraumwissenschaften, Freie Universität Berlin, 1997. ISBN 3-931545-08-3.

F. Fell and J. Fischer. Numerical simulation of the light field in the atmosphere-ocean system using the matrix-operator method. *J. Quant. Spectrosc. Radiat. Transfer*, 3:351–388, 2001.

J. Fischer. Fernerkundung von Schwebstoffen im Ozean. *Hamburger Geophysikalische Einzelschriften*, 65, 1983.

J. Fischer and H. Graßl. Radiative transfer in an atmosphere-ocean system: an azimuthally dependent matrix-operator approach. *Appl. Opt.*, 23:1035–1039, 1984.

J. Fischer and U. Kronfeld. Sun-stimulated chlorophyll fluorescence. 1. Influence of oceanic properties. *Int. J. Remote Sensing*, 11:2125–2147, 1990.

J. Fischer and P. Schüssel. Sun-stimulated chlorophyll fluorescence. 2. Impact of atmospheric properties. *Int. J. Remote Sensing*, 11:2149–2162, 1990.

R. Frouin, S. F. Lacobellis, and P.-Y. Deschamps. Influence of oceanic whitecaps on the global radiation budget. *Geophys. Res. Lett.*, 28(8):15231526, 2001.

H. R. Gordon and W. M. Balch. *MODIS Detached Coccolith Concentration Algorithm Theoretical Basis Document*, version 4 edition, 1999.

H. R. Gordon and A. Morel. *Remote Assessment of Ocean Color for Interpretation of Satellite Visible Imagery. A Review.* Springer-Verlag, New York, 1983.

H. R. Gordon, G. C. Boynton, W. M. Balch, S. B. Groom, D. S. Harbour, and T. J. Smyth. Retrieval of coccolithophore calcite concentration from seawifs imagery. *Geophys. Res. Letters*, 28(8):1587–1590, Apr. 2001. doi: 10.1029/2000GL012025.

W. W. Gregg. A coupled ocean-atmosphere radiative model for global ocean biogeochemical models. Technical Report Series on Global Modeling and Data Assimilation 104606, NASA GSFC, 2002. URL `http://gmao.gsfc.nasa.gov/research/oceanbiology/reprints/gregg_NASATM2002.pdf`.

W. W. Gregg. *Ocean-Colour Data Merging.* Number 6. IOCCG Report, 2007.

G. M. Hale and M. R. Querry. Optical constants of water in the 200nm to 200μm wavelength region. *Appl. Opt.*, 80(3):555–563, 1973.

G. M. Hallegraeff. *Manual on Harmful Marine Microalgae*, chapter Harmful algal blooms: a global overview, pages 25–49. UNESCO Publishing, 2003.

M. Hansson and B. Hkansson. Baltic algae watch system - a remote sensingapplication for monitoring cyanobacterial blooms in the baltic sea. *J. Appl. Rem.Sens.*, 1(011507):1–10, 2007. doi: 10.117/1.2834769.

P. Holligan, S. Ackleson, and K. Voss. Biological and optical properties of mesoscale coccolithophore blooms in the gulf of maine. *Limnol. Oceanogr.*, 36:629–643, 1991.

P. Holligan, E. Fernandez, J. Aiken, W. M. Balch, P. Boyd, P. Burkhill, M. Finch, S. Groom, G. Malin, K. Muller, D. Purdie, C. Robinson, C. Trees, S. Turner, and P. van der Wal. A biogeochemical study of the coccolithophore emiliania huxleyi in the north atlantic. *Global Biogeochem. Cycles*, 7:879–900, 1993.

J. W. Hovenier. *Light Scattering by Nonspherical Particles.* Academic Press, 2000.

H. C. v. d. Hulst. *Light scattering by small particles.* John Wiley and Sons, New York, 1957.

IOCCG. *Remote Sensing of Ocean Colour in Coastal, and Other Optically-Complex, Waters*, volume 3. International Ocean-Colour Coordinating Group, 2000.

M. Kahru. Using satellites to monitor large-scale environmental change: A case study of the cyanobacteria blooms in the baltic sea. monitoring algal blooms: New techniques for detecting large-scale environmental change. *Landes Bioscience*, 1997.

M. Kahru, U. Horstmann, and O. Rud. Satellite detection of increased cyanobacteria blooms in the baltic sea: Natural fluctuation or ecosystem change? *Ambio*, 23(8), 1994.

M. Karjalainen, J. Engström-Öst, S. Korpinen, H. Peltonen, J.-P. Pääkkönen, S. Rönkkönen, S. Suikkanen, and M. Viitasalo. Ecosystem consequences of cyanobacteria in the northern baltic sea. *Ambio*, 36(2-3):195–202, 2007.

J. T. O. Kirk. *Light and Photosynthesis in Aquatic Ecosystems.* Cambridge University Press, 1994. ISBN ISBN0521453534.

S. Y. Kotchenova, E. F. Vermote, R. Matarrese, and J. F. J. Klemm. Validation of a vector version of the 6s radiative transfer code for atmospheric correction of satellite data. part i: Path radiance. *Applied Optics*, 45(26):6762–6774, 2006. doi: doi:10.1364/AO.45.006762. URL `http://www.opticsinfobase.org/abstract.cfm?uri=ao-45-26-6762`.

S. Kratzer and P. Tett. Using bio-optics to investigate the extent of coastal waters - a swedish case study. *Hydrobiologia*, in press, 2009.

S. Kratzer, C. Brockmann, and G. Moore. Using meris full resolution data to monitor coastal waters a case study from himmerfjrden, a fjord-like bay in the northwestern baltic sea. *Remote Sensing of Environment*, 112(5):2284–2300, May 2008.

T. Kutser. Quantitative detection of chlorophyll in cyanobacterial blooms by satellite remote sensing. *Limnol. Oceanogr.*, 49(6):2179 – 2189, 2004.

T. Kutser, L. Metsamaa, N. Strömbeck, and E. Vahtmäe. Monitoring cyanobacterial blooms by satellite remote sensing. *Estuarine Coastal and Shelf Scien.*, 67(1-2):303 – 312, 2006.

C. Le Quéré and S. Pesant. Plankton functional types in a new generation of biogeochemical models. *Eos Trans. AGU*, 90(90):3031, 2009.

C. Le Quéré, S. P. Harrison, I. C. Prentice, E. T. Buitenhuis, O. Aumont, L. Bopp, H. Claustre, L. Cotrim da Cunha, R. Geider, X. Giraud, C. Klaas, K. E. Kohfeld, L. Legendre, M. Manizza, T. Platt, R. B. Rivkin, S. Sathyendranath, J. Uitz, A. J. Watson, and D. Wolf-Gladrow. Ecosystem dynamics based on plankton functional types for global ocean biogeochemistry models. *Global Change Biology*, 11:20162040, 2005. doi: 10.1111/j.1365-2486.2005.01004.

Z. Lee. *Remote Sensing of Inherent Optical Properties: Fundamentals, Tests of Algorithms, and Applications.* Number 5. IOCCG Report, 2006.

H. Loisel and A. Morel. Light scattering and chlorophyll concentration in case 1 waters: A reexamination. *Limnol. and Oceanogr.*, 43:847–858, 1998.

C. A. Marandino, W. J. De Bruyn, S. D. Miller, and E. S. Saltzman. Dms air/sea flux and gas transfer coefficients from the north atlantic summertime coccolithophore bloom. *Geophys. Res. Lett.*, 12 (L23812):L23812, 2008. doi: 10.1029/2008GL036370.

B. R. Marshall and R. C. Smith. Raman scattering and in-water ocean optical properties. *Applied Optics*, 29(1):71–84, 1990.

D. F. Millie and O. Schofield. What are the requirements for the bio-optical characterization of harmful algal blooms? *J. Phycol.*, 31(3), 1995.

J. Milliman, P. Troy, W. Balch, A. Adams, Y.-H. Li, and F. MacKenzie. Biologically-mediated dissolution of calcium carbonate above the chemical lysocline? *Deep-Sea Res. I*, 46:1653–1669, 1999.

J. D. Milliman. Production and accumulation of calcium carbonate in the ocean: budget of a nonsteady state. *Global Biogeochemical Cycles*, 7:927–957, 1993.

C. D. Mobley. A numerical model for the computation of radiance distributions in natural waters with wind-roughened surfaces. *Limnology and Oceanography*, 34(8):1473–1483, 1989. URL `http://www.jstor.org/stable/2837032`.

C. D. Mobley. *Light and Water.* Academic Press, San Diego, CA, 1994.

C. D. Mobley, B. Gentili, H. R. Gordon, Z. Jin, G. W. Kattawar, A. Morel, P. Reinersman, K. Stammes, and R. H. Stawn. Comparison of numerical models for computing underwater light fields. *Appl. Opt.*, 32:7484–7505, 1993.

K. D. Moore, K. J. Voss, and H. R. Gordon. Spectral reflectance of withecaps: Their contribution to water-leaving radiance. *J. Geophys. Res.*, 105:6493–6499, 2000.

A. Morel. *Optical aspects of oceanography*, chapter : Optical properties of pure water and pure sea water, pages 1–24. London: Academic Press, 1974.

A. Nair, S. Sathyendranath, T. Platt, J. Morales, V. Stuart, M. Forget, E. Devred, and H. Bouman. Remote sensing of phytoplankton functional types. *Remote Sens. Environ.*, 112:3366–3375, 2008. doi: 10.1016/j.rse.2008.01.021.

T. Ohde, H. Siegel, and M. Gerth. Validation of meris level-2 products in the baltic sea, the namibian coastal area and the atlantic ocean. *Int. J. remote sensing*, 28:609–624, 2007.

R. Olsonen. Meri- report series of the finnish institute of marine research. fimr monitoring of the baltic sea environment. annual report 2007. Technical Report 62, 2008.

J. E. O'Reilley, S. Maritorena, B. G. Mitchell, D. A. Siegel, K. L. Carder, S. A. Garver, M. K. Kahru, and C. McClain. Ocean color chlorophyll algorithms for SeaWiFS. *J. Geophys. Res.*, 103:24937–24953, 1998.

W. S. Pegau, D. Gray, and J. R. V. Zaneveld. Absorption and attenuation of visible and near-infrared light in water: dependence on temperature and salinity. *Appl. Opt.*, 36:6035–6046, 1997. URL `http://www.opticsinfobase.org/ao/abstract.cfm?URI=ao-36-24-6035`.

T. Platt and S. Sathyendranath. Ecological indicators for the pelagic zone of the ocean from remote sensing. *Remote Sensing of Environment*, 112:3426–3436, 2008.

R. M. Pope and E. S. Fry. Absorption spectrum (380-700 nm) of pure water. II. Integrating cavity measurements. *Appl. Opt.*, 36:8710–8723, 1997.

R. Preusker. Fernerkundung der Wolkenhöhe mit Messungen in der O_2-A Bande. Strahlung in Atmosphäre und Ozean, Beiträge zur Fernerkundung 15, Institut für Weltraumwissenschaften, Freie Universität Berlin, 1999. ISBN 3-931545-08-3 in press.

R. Preusker. *Fernerkundung des Luftdrucks am Oberrand von Wolken mitMessungen in der O2A-Bande.* PhD thesis, Freie Universitt Berlin, 2001.

R. Preusker, A. Huenerbein, and J. Fischer. *Cloud Detection. MERIS Algorithm Theoretical Basis Document.* ESA, 2005.

A. Quirantes and S. Bernard. Light scattering by marine algae: two-layer spherical and nonspherical models. *J. Quantitative Spectroscopy and Radiative Transfer*, 89(1-4):311–321, 2004. doi: 10.1016/j.jqsrt.2004.05.031.

E. Rantajärvi, R. Olsonen, S. Hallfors, J. Leppanen, and M. Raateoja. Effect of sampling frequency on detection of natural variability in phytoplankton: unattended high-frequency measurements on board ferries in the baltic sea. *J. Mar. Sci.*, 55:697–704, 1998.

D. V. S. Rao. *Algal Cultures, Analogues of Blooms And Applications*, volume 2 vols. Rao, D. V. S., Science Publishers,U.S., 2006.

M. Rast, J. Bezy, and S. Bruzzi. The esa medium imaging spectrometer meris- a review of the instrument and its mission. *Int. J. Remote Sensing*, 20(9):1681–1702, June 1999.

A. Reinart and T. Kutser. Comparison of different satellite sensors in detecting cyanobacterial bloom events in the baltic sea. *Remote Sensing of Environment*, 102(1-2):74 – 85, 2006.

I. S. Robinson. Remote sensing of shelf sea ecosystems. state of the art and perspectives. position paper 12. Marine Board - European Science Foundation, February 2008.

R. Rojas. *Theorie der neuronalen Netze*. Springer-Verlag, 1993.

K. Ruddick, G. Lacroix, Y. Park, V. Rousseau, V. De Cauwer, W. Debruyn, and S. Sterckx. *Real-Time Coastal Observing Systems for Ecosystem Dynamics and Harmful Algal Bloom*, chapter Overview of ocean colour: Theoretical background, sensors and applicability for the detection and monitoring of harmful algae blooms (capabilities and limitations). UNESCO Publishing, Paris, France, 2008.

A. Ruiz-Verdú, S. G. Simis, C. de Hoyos, H. J. Gons, and R. Pena-Martínez. An evaluation of algorithms for the remote sensing of cyanobacterial biomass. *Remote Sensing of Environment*, 112:3996–4008, 2008.

A. Sathyendranath. *Remote Sensing of Ocean Colour in Coastal, and Other Optically-Complex, Waters*. Number 3. IOCCG Report, 2000a.

A. Sathyendranath. *Remote Sensing of Ocean Colour in Coastal, and Other Optically-Complex, Waters*, chapter Colour of Case 2 Waters, pages 23–46. IOCCG, 2000b.

S. Sathyendranath, L. Watts, E. Devred, T. Platt, C. Caverhill, and H. Maass. Discrimination of diatoms from other phytoplankton using ocean-colour data. *Marine Ecology Progress Series*, 272:59–68, May 2004.

H. Schiller and R. Doerffer. Neural network for emulation of an inverse model–operational derivation of Case II water properties from MERIS data. *Int. J. Remote Sensing*, 20:1735–1746, 1999.

H. Schiller and R. Doerffer. mproved determination of coastal water constituent concentrations from meris data. *IEEE Transactions on Geoscience and Remote Sensing*, 43:1585–1591, 2005.

T. Schröder. *Fernerkundung von Wasserinhaltsstoffen in Kstengewssern mit MERIS unter Anwendung expliziter und impliziter Atmosphrenkorrekturverfahren*. PhD thesis, Freie Universität Berlin, Fachbereich Geowissenschaften, 2005. URL `http://www.diss.fu-berlin.de/diss/receive/FUDISS_thesis_000000001597`.

T. Schroeder, I. Behnert, M. Schaale, J. Fischer, and R. Doerffer. Atmospheric correction algorithm for meris above case-2 waters. *Intl. J. Rem. Sens.*, 28(7):1469–1486, 2007a.

T. Schroeder, M. Schaale, and J. Fischer. Retrieval of atmospheric and oceanic properties from meris measurements: A new case-2 water processor for beam. *Intl. J. Rem. Sens.*, 28(24):5627–5632, 2007b.

J. N. Schwarz, P. Kowalczuk, S. Kaczmarek, G. F. Cota, B. G. Mitchell, M. Kahru, F. P. Chavez, A. Cunningham, D. McKee, P. Gege, M. Kishino, D. A. Phinney, and R. Raine. Two models for absorption by coloured dissolved organic matter (cdom). *Oceanologia*, 44(2):209–241, 2002.

J. M. Sieburth, V. Smetacek, and J. Lenz. Pelagic ecosystem structure: Heterotrophic compartments of the plankton and their relationship to plankton size fractions. *Limnol. Oceanogr.*, 23:12561263, 1978.

H. Siegel, T. Ohde, and M. Gerth. Preliminary meris-validation results for the baltic sea. In *Proceedings of Envisat - Validation Workshop*, 2003.

H. Siegel, M. Gerth, and G. Tschersich. Sea surface temperature development of the baltic sea in the period 1990-2004. *Oceanologia*, 48:119–131, 2006.

S. G. H. Simis, S. W. M. Peters, and H. J. Gons. Remote sensing of the cyanobacterial pigment phycocyanin in turbid inland water. *Limnology and Oceanography*, 50:237–245, 2005a.

S. G. H. Simis, M. Tijdens, H. L. Hoogveld, and H. J. Gons. Optical changes associated with cyanobacterial bloom termination by viral lysis. *Journal of Plankton Research*, 27:937–949, 2005b.

T. J. Smayda. What is a bloom? a commentary. *Limnology and Oceanography*, 42(5 (2)):1132–1136, July 1997a.

T. J. Smayda. Harmful algal blooms: Their ecophysiology and general relevance to phytoplankton blooms in the sea. *Limnology and Oceaanography*, 42(5/2):1137–1153, 1997b.

T. J. Smyth, G. F. Moore, S. B. Groom, P. E. Land, and T. Tyrrell. Optical modeling and measurements of a coccolithophore bloom. *Appl. Optics*, 41(36):7679–7688, Dec 2002.

S. Solomon, D. Qin, M. Manning, Z. Chen, M. Marquis, K. Averyt, M. Tignor, and H. Miller. *Climate Change 2007: The Physical Science Basis. Contribution of Working Group I to the Fourth Assessment Report of the Intergovernmental Panel on Climate Change.* Cambridge University Press, Cambridge, United Kingdom and New York, NY, USA, 2007.

P. A. Staehr, S. Markagers, and K. Sand-Jensen. Pigment specific in vivo light absorption of phytoplankton from estuarine, coastal and oceanic waters. *Marine ecology. Progress series*, 275:115–128, 2004.

R. P. Stumpf and M. C. Tomlinson. Use of remote sensing in monitoring and forecasting of harmful algal blooms. In R. J. Frouin, M. Babin, and S. Sathyendranath, editors, *Remote Sensing of the Coastal Oceanic Environment.*, volume 5885 of *Proceedings of the SPIE*, pages 148–151, Aug. 2005. doi: 10.1117/12.614376.

R. P. Stumpf, M. E. Culver, P. A. Tester, M. Tomlinson, G. J. Kirkpatrick, B. A. Pederson, E. Truby, V. Ransibrahmanakul, and M. Soracco. Monitoring of karenia brevis blooms in the gulf of mexico using satellite ocean color imagery and other data. *Harmful Algae*, 2(2):147–160, June 2003. doi: 10.1016/S1568-9883(02)00083-5.

A. Subramaniam, R. R. Hood, C. W. Brown, E. J. Carpenter, and D. G. Capone. Detecting trichodesmium blooms in seawifs imagery. *Deep-Sea Res. Part II*, 49(1-3):107–121, 2002.

F. J. R. Taylor. Red tides, brown tides and other harmful algal blooms: The view into the 1990's. In *Proceedings of 4th International Conference on Toxic marine phytoplankton*, pages 527–533, 1990.

The BACC Author Team. *Assessment of Climate Change for the Baltic Sea Basin.* Regional Climate Studies. Springer Netherlands, 2008.

T. Tyrrell and A. H. Taylor. A modelling study of emiliania huxleyi in the ne atlantic. *J. Mar. Systems*, 9(1/2):83–112, Oct. 1996. doi: 10.1016/0924-7963(96)00019-X.

T. Tyrrell, P. M. Holligan, and C. D. Mobley. Optical impacts of oceanic coccolithophore blooms. *J. Geophys.Res.*, 104(C2):3223–3242, Feb 1999. doi: 10.1029/1998JC900052.

J. Uitz, Y. Huot, F. Bruyant, M. Babin, and H. Claustre. Relating phytoplankton photophysiological properties to community structure on large scale. *Limnol. and Oceanogr.*, 53(2):614–630, 2008.

M. Vargas, C. W. Brown, and M. R. P. Sapiano. Phenology of marine phytoplankton from satellite ocean color measurements. *Geophys. Res. Lett.*, 36(L01608), 2009. doi: 10.1029/2008GL036006.

J. Vepsäläinen, T. Pyhälahti, E. Rantajärvi, K. Kallio, S. Pertola, T. Stipa, M. Kiirikki, and J. Pulliainen. The combined use of optical remote sensing data and unattended flow-through fluorometer measurements in the baltic sea. *Int. J. Rem. Sens.*, 26(2):261–282, 2005.

A. Voipio. *The Baltic Sea.* Elsevier oceanography series ; 30. Elsevier/North-Holland, 1981.

H. Volten, J. de Haan, J. Hovenier, R. Scheurs, W. Vassen, and A. Dekker. Laboratory measurements of angular distributions of light scattered by phytoplankton and silt. *Limnol. and Oceanogr.*, 43:11801197, 1998.

P. Westbroek and E. de Jong. *Biomineralization and Biological Metal Accumulation. Biological and Geological Perspectives.* Reidel, Dordrecht, 1983.

R. Wollast. The relative importance of biomineralization and dissolution of caco3 in the global carbon cycle. Bulletin de l'Institut Ocanographique de Monaco Spec 13, 1994. 13-35.

J. Zaneveld, M. Twardowski, M. Lewis, and A. Barnard. *Introduction to Radiative Transfer*, pages 347–368. Dordrecht, 2005.

T. Zhang, F. Fell, Z.-S. Liu, R. Preusker, J. Fischer, and M.-X. He. Evaluating the performance of artificial neural network techniques for pigment retrieval from ocean color in case i waters. *J. Geophys. Res.*, 108(C9):3286, 2003. doi: 10.1029/2002JC001638.

X. Zhang, L. Hu, and M.-X. He. Scattering by pure seawater: Effect of salinity. *Optics Express*, 17(7): 5698–5710, 2009. doi: 10.1364/OE.17.005698.

Acknowledgements

I would like to thank all the people involved in the realization of this work.

I wish to express my gratitude to Prof. Dr. J. Fischer for his interest in and his support of this work, for his patience and flexibility as well as for reviewing this thesis.

I owe particular thanks to Prof. Dr. M. Thomas for his attandence and advice and his interest in reviewing this work.

I thank my colleagues for their work making this study possible: Prof. Dr. J. Fischer, Dr. F. Fell, and all cooperators for their work on the radiative transfer code MOMO, Dr. T. Zhang for his work on phase function parameterization, Dr. T. Schröder for his work on the atmospheric model, Dr. R. Preusker for providing the ANN code and the MERIS cloud mask, as well as Dr. T. Schröder and R. Leinweber for the start-up help with MERIS operational and NRT processing.

I wish to acknowledge Drs. S. Kratzer and N. Stroembeck for providing unpublished and published ground-truth and *in-situ* data.

For granting financial support, I acknowledge German Rosa-Luxemburg Foundation, funding this work with a PhD fellowship.

Travelling support to summer schools, workshops, conferences and a lab practical stay was funded by: German Research Foundation DFG, German Aerospace Center DLR, Australian Commonwealth Scientific and Research Organization CSIRO - Land & Water division, Freie Universität Berlin - Institut für Weltraumwissenschaften FUB-WeW, Universität Bremen - IUP, and Rosa-Luxemburg Foundation.

Many thanks to all colleagues and ex-colleagues of WeW for the on-topic and off-topic disscussions in a very pleasant research atmosphere. Special thanks to the ’FUB-WeW Service and HelpDesk Team’, *explicitly* to R. Leinweber.

Big thanks to the first readers spread around the globe: Drs. A. Hünerbein and J. Mendrok. Thanks for all the open, helpfull, guiding, supporting, and pressuring words: Drs. U. Böttger, A. Hünerbein, and J. Mendrok.

I greatly thank you all for your support. Merci beaucoup!